Phonon renormalization in La-cobaltate and Fe-based superconductors investigated by inelastic neutron and x-ray scattering

Zur Erlangung des akademischen Grades eines

DOKTORS DER NATURWISSENSCHAFTEN

von der Fakultät für Physik des
Karlsruher Institut für Technologie (KIT)

genehmigte

DISSERTATION

von

M. Sc. Maximilian Kauth
aus Würzburg

Tag der mündlichen Prüfung: 09.11.2018

Referent: Priv.-Doz. Dr. F. Weber
Korreferent: Prof. Dr. H. v. Löhneysen

Contents

Chapter 1

Introduction

Neutron scattering is one of the most important, versatile and powerful tools in solid state physics. It is not only used to examine crystal and magnetic structures but also to study their excitations in solids. In the last few years inelastic x-ray scattering became another important technique to complement lattice dynamical investigations with inelastic neutron scattering. In the present work both methods have been used to investigate the phonon renormalization in lanthanum cobaltate $LaCoO_3$ and iron-based superconductors of the AFe_2As_2 (A = Ba, Sr) family. Moreover two further neutron scattering techniques, neutron diffraction and neutron resonance spin echo spectroscopy, were used to study additional aspects of the investigated systems.

The second chapter briefly introduces the basic concepts of neutron scattering and the techniques used in this thesis. Furthermore it gives a short overview on lattice dynamical calculations which provided important support for planning, analyzing and discussing the scattering experiments on $LaCoO_3$.

The third chapter is devoted to the lattice dynamical investigations in lanthanum cobaltate. $LaCoO_3$ exhibits two crossovers at $T_{\mathrm{SS}} \approx 100\,\mathrm{K}$ and $T_{\mathrm{MI}} \approx 500\,\mathrm{K}$ observed in various physical properties such as thermal expansion and electric susceptibility. Both crossovers are assumed to be connected to the spin state evolution of the cobalt ions from a low spin to a high spin configuration. Due to the different spatial extent of the corresponding electronic wave functions the crystal lattice is directly affected by the population of high spin states and the expansion of the CoO_6 octahedra around such excited cobalt atoms. It was proposed that the two different spin states form a dynamic short-range order which manifests itself in a breathing-type distortion of the crystal lattice. The second crossover is believed to be caused by a melting of this order. All experimental work on inelastic neutron scattering including the temperature dependence of the phonon energies was accompanied by lattice dynamical calculations. Besides acoustic and optic phonon modes the mean square displacement of the atoms was studied with neutron and x-ray diffraction.

Chapter 4 addresses the phonon renormalization in iron-based superconductors of the AFe_2As_2 ($A = Ba$, Sr) family, with partial substitution of Fe by Co, or Ba and Sr by K and Na. One of the major issues is the relation between lattice dynamics and nematicity, where the latter manifests itself in a structural/nematic phase transition closely connected to magnetism yet setting in at a transition temperature higher than that of long-range magnetic order. The nematic phase does not show a static magnetic order but the magnetic fluctuations have a preferred direction. The results from the inelastic neutron and x-ray scattering experiments in $Ba(Fe_{0.94}Co_{0.06})_2As_2$ in the framework of this thesis served as the starting point for a theoretical model. The model was developed with R. Fernandes (University of Minnesota) and J. Schmalian (Karlsruhe Institute of Technology, KIT) describing the anomalous behavior of the phonon dispersion by introducing the nematic correlation length ξ. Furthermore the neutron resonance spin echo measurements on the same system were used to investigate the temperature dependence of the phonon lifetime. This study yields the first evidence for a damping mechanism in iron-based superconductors which is similar to that in conventional superconductors, e.g. electron-phonon coupling. The last part of this chapter shows first inelastic x-ray measurements on several hole-doped 122 systems.

Chapter 2

Experimental methods

The bestowal of the Nobel Prize in Physics in 1994 to C. G. Shull and B. N. Brockhouse 'for their pioneering contributions to the development of elastic and inelastic neutron scattering' [1] showed how important this techniques had become in science but the beginning of the success story started a lot earlier. Shortly after J. Chadwick discovered the neutron in 1932, its ability to be Bragg diffracted by solids was shown [2]. With an upcoming new generation of high-flux reactors starting in the 1970s the limitations of the early days by the low neutron flux could be overcome, and even inelastic scattering studies became possible. The theory and specific techniques of neutron scattering are widely discussed in several books [3, 4, 5]. Therefore only the basics of neutron scattering will be discussed in Chapter 2.1 and the instruments and methods used for this study will be described in Chapters 2.3 to 2.6.

2.1 Basics of neutron scattering

Neutron scattering is one of the most important and versatile methods in many different fields such as biology, material sciences or solid state physics. The physical properties of the neutron (Table 2.1) make it possible to study not only structural but also dynamic and magnetic properties of matter and especially condensed matter [3]:

- De-Broglie wavelength of $\lambda \approx 2\,\text{Å}$ for thermal neutrons (Table 2.2): The interatomic distances are about the same size and this leads to interference effects that enable structural analysis.

- Charge neutrality: the interaction between the neutrons and the scattering material is quite weak which leads to a large penetration depth. Therefore neutrons can be used to study the bulk properties of the sample.

- Several excitations in condensed matter are energetically in the same region as thermal neutrons ($E \approx 25\,\mathrm{meV}$): using inelastic scattering phonons and magnons can be observed.

- Magnetic moment: neutrons interact with magnetic atoms and therefore can be used to observe magnetic structures and excitations.

Table 2.1: Basic Properties of the neutron [3].

Mass	$m = 1.675 \cdot 10^{-27}\,\mathrm{kg}$
Spin	1/2
Charge	0
Magnetic moment	$\mu_\mathrm{n} = -1.913\,\mu_\mathrm{N}$

The most common source of neutrons for science are fission reactors. Neutrons coming directly from the core of a reactor have to be moderated, otherwise their energy would be too high to study condensed matter properties. For cold neutrons liquid H_2 or CH_4, for thermal neutrons heavy water and for hot neutrons a hot massive block (for example graphite heated to $T \approx 2400\,\mathrm{K}$) could be used to select a range of the neutron wavelength suiting the desired purpose (Table 2.2).

Table 2.2: Approximate values for the range of energy, temperature and wavelength for three types of sources in a reactor [3].

Source	Energy E (meV)	Temperature T (K)	Wavelength λ (10^{-10} m)
Cold	0.1 - 10	1 - 120	30 - 3
Thermal	5 - 100	60 - 1000	4 - 1
Hot	100 - 500	1000 - 6000	1 - 0.4

In the following the scattering mechanisms that are most important for this work and the coherent effective cross-sections are briefly described.

Elastic scattering at atomic nuclei

The differential cross section for elastic scattering at a crystal lattice with a multi atomic basis from the initial state $|\mathbf{k_i}\rangle$ to the final state $|\mathbf{k_f}\rangle$ is given by

$$\left(\frac{\mathrm{d}\sigma}{\mathrm{d}\Omega}\right) \propto \sum_{\mathbf{G}} \delta(\mathbf{Q} - \mathbf{G})\,|F(\mathbf{G})|^2 \tag{2.1}$$

with the static structure factor

$$F(\mathbf{G}) = \sum_j b_j e^{i\mathbf{G}\cdot\mathbf{r}_j} e^{-W_j}. \tag{2.2}$$

$\mathbf{Q} = \mathbf{k}_f - \mathbf{k}_i$ is the scattering vector and $\mathbf{G}$ a reciprocal lattice vector. The Laue condition for crystal diffraction is represented by the delta function in Equation 2.1, which is equivalent to the Bragg condition for constructive interference between lattice planes $\langle hkl \rangle$

$$\lambda = 2d_{\mathrm{hkl}} \sin(\Theta). \tag{2.3}$$

In Equation 2.2 the structure factor $F(\mathbf{G})$ describes interferences between different atoms j with the coordinates $\mathbf{r}_j$ inside the unit cell, with the scattering length b_j. The Debye-Waller-factor $\exp(-W_j)$ describes the reduction of the intensity of the diffraction reflexes due to thermal displacements $\mathbf{u}$ from the equilibrium position of the atoms. For small displacements one can write

$$W = \frac{1}{2}\langle(\mathbf{Q}\cdot\mathbf{u})^2\rangle. \tag{2.4}$$

Inelastic scattering at atomic nuclei - Phonons

In general the differential scattering cross section for inelastic scattering can be written as

$$\frac{\mathrm{d}^2\sigma}{\mathrm{d}\Omega_f \mathrm{d}E_f} = N\frac{k_f}{k_i} S(\mathbf{Q},\omega) \tag{2.5}$$

with the scattering function $S(\mathbf{Q},\omega)$. The fluctuation dissipation theorem connects it with the imaginary part of the dynamical susceptibility $\chi(\mathbf{Q},\omega)$:

$$S(\mathbf{Q},\omega) = \frac{\chi''(\mathbf{Q},\omega)}{1-\mathrm{e}^{-\hbar\omega/k_B T}} \tag{2.6}$$

For the creation respectively annihilation of a phonon of a certain phonon mode s with the polarization vector $\vec{\xi}_j$ of the atom j with mass m_j it is given by

$$\chi''(\mathbf{Q},\omega) \propto \sum_{\mathbf{G},\mathbf{q}} \delta(\mathbf{Q}-\mathbf{q}-\mathbf{G}) \sum_s \frac{1}{\omega_{\mathbf{q},s}} \left|\mathcal{F}(\mathbf{Q})\right|^2 \cdot \left[\delta(\omega-\omega_{\mathbf{q},s}) - \delta(\omega+\omega_{\mathbf{q},s})\right] \tag{2.7}$$

with the dynamic structure factor

$$\mathcal{F}(\mathbf{Q}) = \sum_j \frac{b_j}{\sqrt{m_j}} \left(\mathbf{Q}\cdot\vec{\xi}_j\right) \mathrm{e}^{i\mathbf{Q}\cdot\mathbf{r}_j}\,\mathrm{e}^{-W_j}\,. \tag{2.8}$$

The expression $\delta(\mathbf{Q}-\mathbf{q}-\mathbf{G})$ in Equation 2.7 pays respect to the conservation of momentum

$$\mathbf{Q} = \mathbf{k}_f - \mathbf{k}_i = \mathbf{G} + \mathbf{q}. \tag{2.9}$$

The conservation of energy for the creation or annihilation of a phonon is given by $[\delta(\omega - \omega_{\mathbf{q},s}) - \delta(\omega + \omega_{\mathbf{q},s})]$. Only the components of the polarization vector parallel to the scattering vector $\mathbf{Q}$ contribute to the scattered intensity because of the scalar product $\mathbf{Q} \cdot \vec{\xi}_j$ in Equation 2.8. With the Equations 2.5, 2.6, 2.7 and 2.8 the integrated phonon intensity becomes

$$I_E \propto [n(\omega) + 1] \cdot \frac{\left|\mathbf{Q} \cdot \vec{\xi}_j\right|^2}{\hbar\omega} \cdot \mathrm{e}^{-2W(\mathbf{Q})} \tag{2.10}$$

for phonon creation and a fixed final energy in the measurements. The phonon intensity that can be observed in the experiment varies as the square of the scalar product of the polarization vector $\vec{\xi}$ and the scattering vector $\mathbf{Q}$. That is why phonon measurements are typically carried out at the highest scattering vectors $\mathbf{Q}$ that can be achieved within the experimental limits. The result is a minimization of magnetic scattering contributions due to the decreasing magnetic form factor with increasing $\mathbf{Q}$ [3].

The Bose Einstein distribution leads to the prefactor $n(\omega)$. Due to the thermal occupation of phonons with an energy $E = \hbar\omega$ with increasing temperature the integrated phonon intensity also increases with

$$[n(\omega) + 1] = \frac{1}{\mathrm{e}^{\frac{\hbar\omega}{k_B T}} - 1} + 1. \tag{2.11}$$

The intensity ratio of phonon creation ($\hbar\omega > 0$) and annihilation ($\hbar\omega < 0$)is described by the detailed-balance condition [5]

$$S(-\mathbf{Q}, -\omega) = \mathrm{e}^{-\hbar\omega_{\mathbf{q},S}/k_B T} \cdot S(\mathbf{Q}, \omega). \tag{2.12}$$

That means that for example at $T = 0$ only phonon creation contributes to the measured phonons since no excitations are thermally populated.

Polarized neutrons

In the sections above the scattering cross section for unpolarized neutrons was discussed where neutrons are scattered from an initial state $|\mathbf{k}_i\rangle$ to a final state $|\mathbf{k}_f\rangle$ regardless of the exact spin state of the neutrons (spin-up $|\uparrow\rangle$ or spin-down $|\downarrow\rangle$). In many cases it is useful to take advantage of the polarization analysis and to get additional information on the observed system or to distinguish between magnetic and nuclear scattering processes. Detailed information on the scattering of polarized neutrons and the scattering cross sections for various scattering processes can be found in the literature [3, 5]. This chapter should just give a brief introduction on the topic.

The following equation describes the beam polarization in the applied field direction normally defined as parallel to the $z-$direction:

$$P_0 = \frac{N_\uparrow - N_\downarrow}{N_\uparrow + N_\downarrow} \tag{2.13}$$

$N_{\uparrow}$ is the number of neutrons in the spin-up state ($|\uparrow\rangle$) and $N_{\downarrow}$ the number of neutrons in den spin-down state ($|\downarrow\rangle$). If the spin state of the neutrons is taken into account, the previously considered scattering cross section for unpolarized neutrons $(\mathrm{d}\sigma/\mathrm{d}\Omega\mathrm{dE})_{|\mathbf{k}_\mathrm{i}\rangle} \rightarrow |\mathbf{K}_\mathrm{f}\rangle$ is split into four different scattering cross sections

$$\left.\begin{array}{l} |\uparrow\rangle \rightarrow |\uparrow\rangle \\ |\downarrow\rangle \rightarrow |\downarrow\rangle \end{array}\right\} \text{non-spin-flip scattering}$$
$$\left.\begin{array}{l} |\uparrow\rangle \rightarrow |\downarrow\rangle \\ |\downarrow\rangle \rightarrow |\uparrow\rangle \end{array}\right\} \text{spin-flip scattering} \tag{2.14}$$

The main objective of polarized neutron experiments is to determine the polarization dependence of scattering. Another technique is neutron spin echo spectroscopy where the main idea is to use the individual spin precession of the neutrons to monitor possible small energy transfers. It will be discussed in Chapter 2.5.

$$\frac{1}{2}\left(\frac{\mathrm{d}\sigma}{\mathrm{d}\Omega\mathrm{d}E}\right)_{\mathrm{mag}} = \left(\frac{\mathrm{d}\sigma}{\mathrm{d}\Omega\mathrm{d}E}\right)_{\mathrm{HF}}^{|\uparrow\rangle\rightarrow|\downarrow\rangle} - \left(\frac{\mathrm{d}\sigma}{\mathrm{d}\Omega\mathrm{d}E}\right)_{\mathrm{VF}}^{|\uparrow\rangle\rightarrow|\downarrow\rangle} \tag{2.15}$$

2.2 Triple axis spectroscopy

One of the most useful and versatile instruments in neutron scattering is the so called triple axis spectrometer (TAS). It is used to probe excitations and fluctuations in liquid and solid matter in both energy and momentum space. The technique was developed by B. N. Brockhouse and was awarded the Nobel Prize in physics together with C. Shull in 1994 [1, 6]. Due to its unique properties the TAS can be used for both, elastic and inelastic scattering.

Layout of a triple axes spectrometer

In figure 2.1 the schematic structure of the thermal TAS 1T at the Orphée reactor at the Laboratoire Léon Brillouin (LLB) is shown. The three independently rotating and eponymous axes are the monochromator axis, the sample axis and the analyzer axis. Essentially it is possible to reach every point in momentum space at any energy with an appropriate setting of the corresponding angles. The polychromatic neutron beam from the neutron source, typically a nuclear reactor, is diffracted at a given set of lattice planes of the monochromator crystal (1). The Bragg diffraction leads to the selection of a specific neutron wavelength λ_i. Starting from Bragg's law

$$G_{hkl} = 2k \sin \Theta_B \tag{2.16}$$

the selected neutron wavelength is

$$\lambda = 2d_{hkl} \sin \Theta_B \tag{2.17}$$

where $G_{hkl} = \frac{2\pi}{d_{hkl}}$ with d_{hkl} the lattice spacing of the planes indicated by the Miller indices $h,\ k,\ l$. Θ_B is the scattering agle and $k = \frac{2\pi}{\lambda}$ the wave vector of the selected neutron. A higher neutron beam intensity is usually achieved by using several small single crystals with a relatively broad mosaic spread as the monochromator. These are arranged in a way that all the neutron intensity can be focused onto the sample position by an adjustable curvature. Today TASs have monochromators and analyzer with horizontally and vertically adjustable curvatures. The sample (4) is normally mounted on a two-circle goniometer for inelastic neutron scattering. If a cryostat is needed for the experiments the sample is placed in an helium filled aluminum can to ensure a small temperature gradient by providing a good thermal contact to the cold finger. The analyzer crystal (5) is used to analyze the final energy E_f of the scattered neutron beam. A typically measuring method is to keep the final energy fixed and vary the scattering angle of the monochromator crystal in an appropriate way to get the chosen energy transfer $\Delta E = E_i - E_f$.

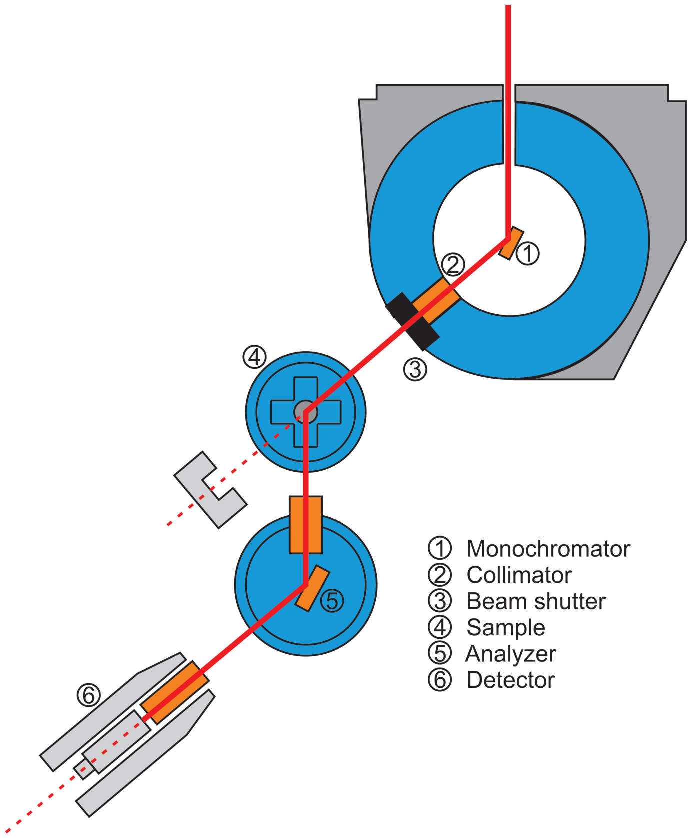

Figure 2.1: Schematic drawing of the thermal triple axes spectrometer 1T at the Orphée reactor at LLB at CEA Saclay in France.

Resolution of a triple axes spectrometer

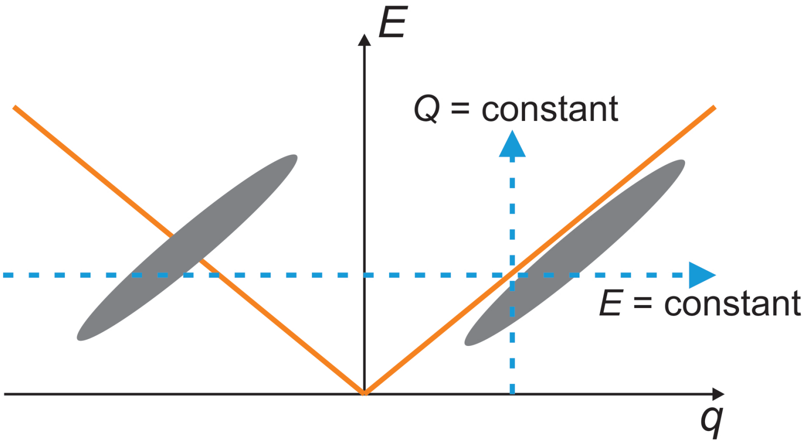

Figure 2.2: Schematic projection of the four dimensional experimental resolution ellipsoid onto the plane defined by E and $\mathbf{q}$. The orange line shows a linear dispersion relation such as that of an acoustic phonon. At positive $\mathbf{q}$, the two longer axes of the resolution ellipsoid (gray) are parallel to the dispersion and hence in an energy or momentum scan (blue dashed lines) a narrow peak will be measured (focused condition). At negative $\mathbf{q}$ the longer axes are orthogonal to the dispersion and the measured peak is broadened (defocused condition).

To obtain a higher intensity of the neutron flux, imperfect crystals with a comparatively high mosaicity and beam divergence are used as monochromator and analyzer. The measured signal is a convolution of an instrumental resolution function $R(\mathbf{Q} - \mathbf{Q}_0, \omega - \omega_0)$ and the scattering function $S(\mathbf{Q}, \omega)$ where the instrumental resolution may become the dominant part due to the choice of imperfect crystals. The resolution function is peaked at $(\mathbf{Q}_0, \omega_0)$ and decreases for deviations $(\Delta\mathbf{Q}, \Delta\omega)$. The shape of the observed spectra is strongly depending on how the resolution function is scanned through the structures defined by the scattering function.

In general, the resolution function can be described by a four dimensional ellipsoid (three dimensions in momentum space and one in energy). If the vertical resolution, i.e. the resolution perpendicular to the scattering plane, is neglected the resolution function can be considered as an three dimensional object, which has a shape that can be described as a flattened cigar. The orientation of the resolution function resolution relative to the dispersion surface will determine the measured peak width in a constant $\mathbf{Q}$ scan through a sharp dispersion surface. If the two longer axes of the ellipsoid are parallel to the surface a narrow peak will be measured (focused condition). In the defocused condition, the two long axes are orthogonal to the dispersion surface and the measured peak may be so broad that it is nearly undetectable. Figure 2.2 shows an acoustic dispersion along one direction in $\mathbf{q}$. The gray are schematically describes a two dimensional projection of the four dimensional experimental resolution ellipsoid onto the plane defined by E and $\mathbf{q}$. The result of the measurement is now depending on how this projection is scanning through the dispersion. The focused condition is shown on the right side and the defocused condition on the left side in this picture.

Special problems

Due to the non-ideal behavior of the various elements of a TAS and the specific sample environment, in both elastic and inelastic scattering, scattering artifacts can be observed. These artifacts often appear as sharp peaks which could be misinterpreted as intrinsic structures. This leads to the necessity of reliably identifying such spurious peaks (so-called spurions) in the measured spectra to extract the physically relevant information. One of the several well understood causes of artifacts is Bragg scattering of higher-order neutrons at the monochromator and analyzer. For a specific scattering angle Θ additionally to neutrons with energy E respectively wave length λ also neutrons with energies n^2E respectively wave lengths λ_n are Bragg diffracted. Analogous to Equation 2.3 one can write

$$\lambda_n = \frac{\lambda_{\max}}{n} \quad \text{mit} \quad \lambda_{\max} = 2d_{\text{hkl}} \sin\Theta \quad (n \in \mathbb{N}). \tag{2.18}$$

To suppress higher-order neutrons a pyrolytic graphite (PG) filter is used that allows the passage of thermal neutrons. In figure 2.3 the transmission of a 5-cm-thick PG filter (c axis parallel to the wave vector of the neutrons) for a desired energy $E(\lambda)$, $4E(\lambda/2)$ and $9E(\lambda/3)$ is shown. In most cases the final energy k_f is kept fixed and the PG filter is placed in between the sample and the analyzer. A very advantageous ratio between transmission in the first order and absorption for higher orders can be achieved for the final energies 14.7 meV and 30.5 meV.

Another cause of artifacts are resolution function effects. When measuring near a reciprocal lattice point $\mathbf{G}$, it is possible that the tail of the resolution ellipsoid ranges through $\mathbf{G}$ and therefore picks up some unwanted intensity and is misinterpreted as an intrinsic signal.

Furthermore there are artifacts caused by the sample environment, such as Bragg scattering by aluminum, which is used for most sample holders, sample cans and cryostat radiation shields. Although the sample can is typically filled with He as an exchange gas, a certain fraction of air can not be avoided. The condensation of these gases can lead to temperature dependent effects of the background.

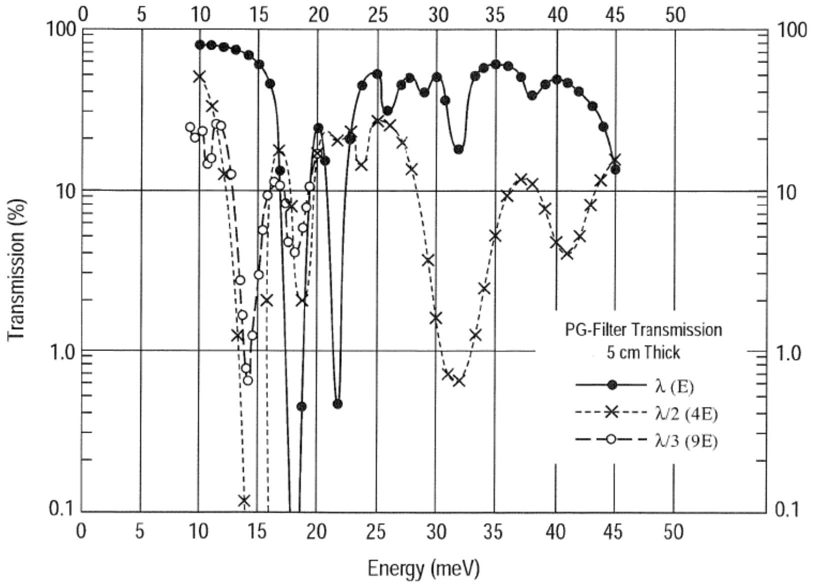

Figure 2.3: Transmission of a 5-cm-thick PG filter as a function of energy for a desired energy $E(\lambda)$ [5].

2.3 Single crystal diffractometer

To study the structural parameters and to determine the overall structure of a crystal, diffraction experiments are often the appropriate technique. The translation symmetry of most crystalline materials allows to obtain the position of all atoms from the position of a all atoms in the unit cell [7, 8]. Thus, the typical aim of diffraction measurements is to determine the atomic positions in the unit cell and the six lattice parameters (the lengths of the lattice vectors a, b and c and the angles between those vectors α, β and γ). Moreover the atomic displacement from the resting positions can be observed.
For example x-rays or neutrons can be used as probes in those experiments, depending on the underlying questions. The various types of radiation are differently scattered at the sample. The neutron is scattered by the atomic nucleus in contrast to x-rays which are scattered by the electronic shell. Depending on the available samples there are two different experimental setups: powder diffraction and single-crystal diffraction. For the work presented in this thesis only the latter was used and therefore only this technique will be discussed further. A single crystal diffractometer is quite similar to a triple axis spectrometer (see Chapter 2.2) with the beam passing the monochromator, the sample and the detector (Fig. 2.4). However the analyzer is not needed since the inelastic intensity can be neglected and the overall intensity can be increased.
The measurements shown in Chapter 3.2.2 were carried out on a x-ray diffractometer

at our institute and on HEiDi, a single crystal diffractometer at the hot neutron source of the Forschungsreaktor München II (FRMII) at the Heinz Maier-Leibnitz Zentrum (MLZ) in Garching, Germany. HEiDi (Fig. 2.4) is a four-circle diffractometer with a large acentric Euler cradle to mount heavy sample environments like cryostats or furnaces [9]. The incident wave lengths can be varied by using three different monochromator crystals at three different monochromator angles which leads to nine possible incident wavelengths between 1.4 Å and 0.3 Å. Furthermore three selectable collimators ($\alpha = 60', 30', 15'$) in front of the monochromator unit can be used for defining the horizontal beam divergence. The sample is mounted in the center of the Eulerian cradle. The scattered neutrons are then detected by a ^{3}He single counter.

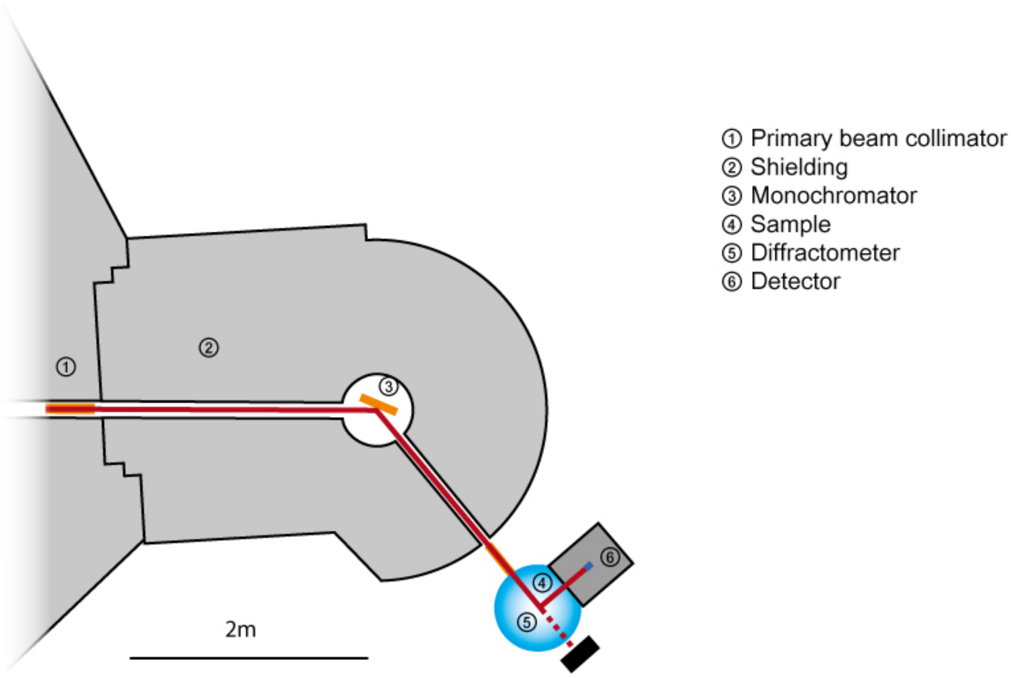

Figure 2.4: Schematic drawing of the single crystal diffractometer HEiDi at the MLZ in Garching [10].

2.4 Inelastic x-ray scattering

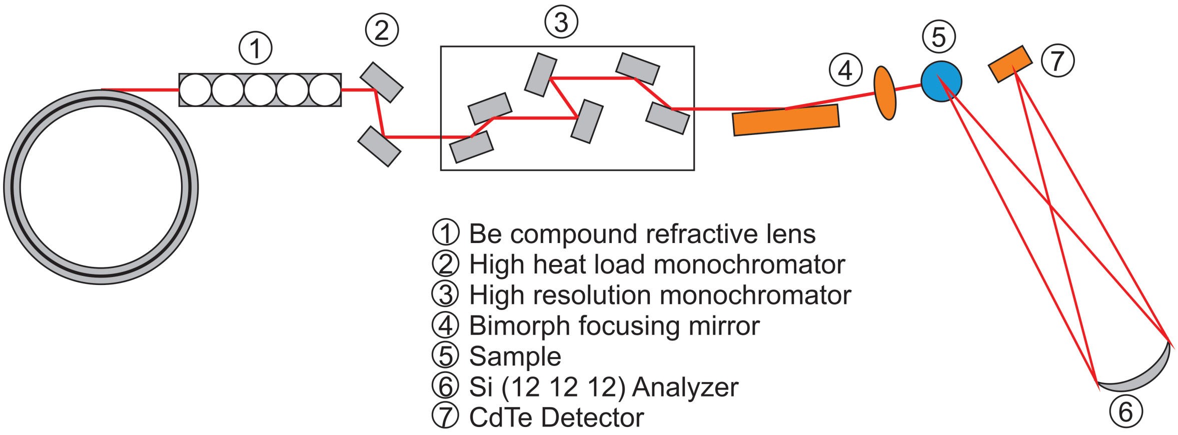

Figure 2.5: Schematic drawing of HERIX at Sector 30 at the APS (cf. [11]).

Another very important method for observations of lattice dynamics in solids is inelastic x-ray scattering (IXS). In the 1980's the idea was born that the synchrotron radiation of particle accelerators can be used for that purpose with a really high energy resolution because of the high intensity and brilliance compared to laboratory x-ray sources [12, 13, 14]. Inelastic x-ray scattering like inelastic neutron scattering is also based on triple axis spectrometry. One of the main differences is the typical incident energy of the x-ray radiation $E_i \approx 20\,\mathrm{keV}$ necessary to cover the wave-vector range of the first Brillouin zone which is roughly six orders of magnitude larger than typical phonon energies. This leads to the necessity of a very good relative energy resolution of about $\Delta E/E \approx 10^{-7}$. The scattering cross sections described above for elastic and inelastic scattering also apply for x-ray scattering if the scattering length in the Equations 2.2 and 2.8 is replaced by the atomic form factor $f^0(\mathbf{Q}) = \int \rho(\mathbf{r}) \exp(i\mathbf{Q}\cdot\mathbf{r}) d\mathbf{r}$. A more detailed description of inelastic x-ray scattering and the derivation of the scattering cross sections can be found in literature [15, 16, 17].

The experiments described in this thesis were all carried out at on the high energy-resolution x-ray (HERIX) spectrometer at sector 30 at the Advanced Photon Source (APS) at Argonne National Laboratory near Chicago, Illinois, in the United States. HERIX is a high energy resolution (1.5 meV) four circle spectrometer for inelastic x-ray measurements used for phonon measurements in solids and liquids [11]. In a first step the synchrotron radiation is gathered and monochromatized by the high heat load monochromator [Fig. 2.5 (2)]. The resolution afterwards does not suit the requirements of phonon measurements with 1.6 eV yet, so the beam has to pass through another three pairs of monochromators (3) until it reaches the final resolution of $\approx 1\,\mathrm{meV}$. After focusing the x-ray beam to a size of around $15 \times 35\,\mu\mathrm{m}^2$ and deflecting it with bimorph mirrors (4), the x-rays are scattered from the sample (5) into nine analyzer crystals (6) arranged in a horizontal line covering different scattering angles simultaneously. The x-rays with the chosen final energy are focused into nine individual point detectors (7). Inelastic x-ray scattering has certain essential advantages compared to inelastic neutron scattering

- energy resolution independent of energy transfer
- good **q** resolution
- very small samples can be investigated due to the good focusing of the beam ($10\,\mu$m)

and of course also some disadvantages

- small penetration depth
- good energy resolution technically complicated
- weak magnetic interaction
- only a few available instruments.

Depending on the underlying question of the investigations and on the available samples a method has the be chosen between inelastic x-ray and neutron scattering. Both methods are complementary, not competitive.

2.5 Resonance spin echo spectroscopy

Combining triple-axis spectroscopy (see Chapter 2.2) with neutron spin echo techniques (NSE) makes it possible to measure the linewidths of dispersive excitations like phonons or magnons with an energy resolution of down to a few μeV. To gather some of the data for this thesis the three axes spin echo spectrometer (TRISP) (Fig. 2.6) at the research neutron source Heinz Maier-Leibnitz (FRM II) in Garching was used [18, 19].

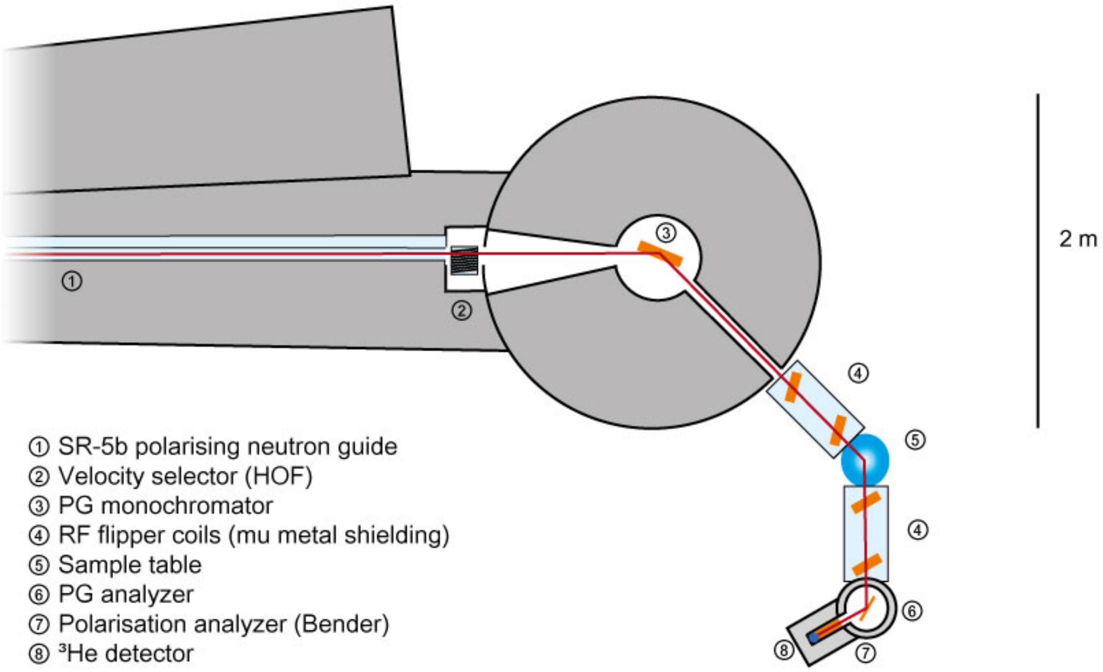

Figure 2.6: Schematic drawing of the three axes spin echo spectrometer (TRISP) at the research neutron source Heinz Maier-Leibnitz (FRM II). The neutron guide (1) polarizes the incoming neutron beam from the reactor. After passing the velocity selector (2) the incident energy is chosen with the help of a double focusing graphite monochromator (3). Right before and after the sample (5) two pairs of RF flipper coils are positioned (4) the first pair creates a Larmor precession ϕ_1 (see text) and the second one a larmor precession ϕ_2. The analyzer (6) is also made of graphite and for the detection of the neutrons a ^{3}He detector (8) is used. The polarization analysis can be done with the help of a polarized neutron guide (7) which is only transparent to one neutron polarization. [20]

Conventional NSE techniques are using the Larmor precession of a polarized neutron beam to determine slight changes in the velocity of incident and scattered neutrons (see also [21]). Neutrons with $\mathbf{k}_1$ along the y-direction and a polarization along the x-direction precess in a magnetic field with the strength B_1 and the length L_1 (in z-direction) by an angle of

$$\phi_1 = \frac{2\omega_z^{(1)} L_1}{v_1}. \tag{2.19}$$

The Larmor frequency ω_L is given here as

$$\omega_L^{(1)} = 2\omega_z^{(1)} = \frac{2\mu B_1}{\hbar}. \tag{2.20}$$

The scattered neutrons precess in a second magnetic field with the strength B_2 and the length L_2 with an orientation in the opposite direction than B_1 by the angle

$$\phi_2 = \frac{2\omega_z^{(2)} L_2}{v_2}. \tag{2.21}$$

If $B_1 = B_2 = B$ and $L_1 = L_2 = L$ the precession angle of the neutrons after passing both magnetic fields for energy transfers of $\hbar\omega = m/2(v_2^2 - v_1^2)$ is given by [21, 22]:

$$\begin{aligned} \phi_{\text{NSE}} = \phi_1 + \phi_2 &= 2\omega_z \left[\frac{1}{v_1} - \frac{1}{v_2}\right] \\ &\approx \left(\frac{2\hbar\omega_z L}{m v_1^3}\right)\omega = \omega\tau_{\text{NSE}}, \end{aligned} \tag{2.22}$$

where τ_{NSE} is the spin echo time. The approximation is only valid for small changes in the velocity $v_2 = v_1 + \delta v$ with $\delta v << v_1$ (quasi elastic scattering). For neutron resonant spin echo (NRSE) techniques, high frequency spin flippers are used instead of the homogeneous magnetic fields of large coils with the lengths $L_{1,2}$ [23]. The flippers generate two fields, B_z along the z-direction is time-independent and B_r is rotating in the x-y-plane with the frequency ω_S, which meets the resonance conditions:

$$\omega_s = 2\omega_z = \gamma B_z = \omega_L \tag{2.23}$$

where γ is the gyromagnetic ratio of the neutron. The amplitude of B_r satisfies the condition

$$\gamma B_r = \frac{\pi v}{d} \tag{2.24}$$

with the neutron velocity v and the coil length d [23, 24]. A pair of these coils can be used to achieve the same precession angle ϕ as in a homogenous magnetic field. The energy transfer ω of dispersive excitations is dependent on the wave vector $\mathbf{q}$ of the excitation, therefore $\omega = \omega(\mathbf{q})$. With the $\mathbf{q}$ resolution being finite ω broadens and a spin echo phase ϕ_{NSE} can even be measured for excitations with a linewidth of zero. To measure the intrinsic linewidth of phonons, the spin echo phase has to be adjusted to the slope of the dispersion area, i.e. the group velocity $\mathbf{v}_g = \nabla_{\mathbf{q}}\omega$. This phonon focusing leads to a constant phase ϕ_{NSE} for all scattering contributions along a straight line with the slope $\mathbf{v}_g$ (Fig. 2.7). Such a phonon focusing can be achieved by tilting the field boundaries relative to the beam direction [24]. Then all neutrons scattered by a phonon with a linewidth near zero and a linear dispersion have the same spin echo phase

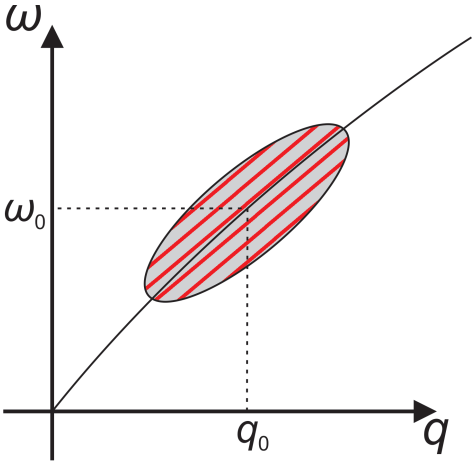

Figure 2.7: Focusing conditions for measuring phonons with neutron resoanant spin echo techniques (see [18, 21]). The resolution function of the triple axis spectrometer (resolution ellipsoid) defines a region in the momentum and energy space. The high energy resolution is achieved with the spin echo spectrometer. Therefore the lines $\phi_{\text{NSE}} =$ constant (red lines) have to be aligned parallel to the dispersion area by tilting the field boundaries (phonon focusing).

ϕ_{NSE}. For finite linewidths a broadening of ϕ_{NSE} occurs and leads to a depolarization of the neutron beam which is proportional to the Fourier transformation of the spectral line shape. A detailed derivation of the focusing condition, i.e. the development of Equation 2.22 in terms of $\mathbf{v}_{1,2} = \bar{\mathbf{v}}_{1,2} + \delta\mathbf{v}_{1,2}$, can be found in literature [18, 21]. The spin echo time τ_{NSE} is determined by the chosen frequencies $\omega_{s(1,2)}L_{1,2}$ and is identical for both parts of the spectrometer before and after the sample. The polarization of the scattered neutron beam after passing the second pair of coils is given by

$$P(\tau_{\text{NSE}}) \propto \int S(\omega)\cos(\omega\tau_{\text{NSE}})\mathrm{d}\omega \tag{2.25}$$

and is the Fourier transformed of the scattering function $S(\omega)$. When describing $S(\omega)$ by a Lorentzian function with full width half maximum Γ

$$S(\omega) = \frac{1}{\pi}\frac{\Gamma}{\Gamma^2 + \omega^2} \tag{2.26}$$

the polarization decreases exponentially:

$$P(\tau_{\text{NSE}}) \propto \mathrm{e}^{-\Gamma\tau_{\text{NSE}}}\,. \tag{2.27}$$

As a conclusion the intrinsic phonon linewidth Γ can be determined by measuring the polarization as a function of τ_{NSE}. Resolution effects that lead to a further depolarization of the neutron beam are discussed in [25, 26]. The method of the data acquisition of such a measurement is illustrated step by step in figure 2.8 for the example of $\mathrm{Ba(Fe_{1-x}Co_x)_2As_2}$. A triple axis scan is used to determine the phonon energy for a given wave vector [Fig. 2.8(a)]. All angles of the triple axis spectrometer are kept fixed on the positions determined in this first scan during the NRSE measurements. The polarization of a specific τ_{NSE} is measured by the variation of the length of the second precession area in the second part of the spectrometer by translation of the second RF coil by small distances ΔL (b). This results in an oscillation of the measured intensity:

$$I(\Delta L) = I_0 \left(1 + P \cos\left[2\pi \frac{\Delta L + \Delta L_0}{\Delta L_p}\right]\right) \tag{2.28}$$

where ΔL_p is the length of the period of the oscillation, ΔL_0 a constant offset and I_0 the mean intensity. These measurements of ΔL range over a period length ΔL_p (typically a few mm) which is specified by the parameters of the used instrument. The polarization can be determined by fitting Equation 2.28 to the experimental data. This has to be done for at least four different τ_{NSE} values to get a reliable set of data. The ratio ω_{s1}/ω_{s2} is kept fixed. The intrinsic phonon linewidth can then be determined by fitting Equation 2.27 to the gathered polarization values $P(\tau_{\mathrm{NSE}})$. Under ideal conditions the described technique allows to measure phonon linewidths of just a few μeV, which has been demonstrated on pure element superconductors Pb and Nb [25, 27].

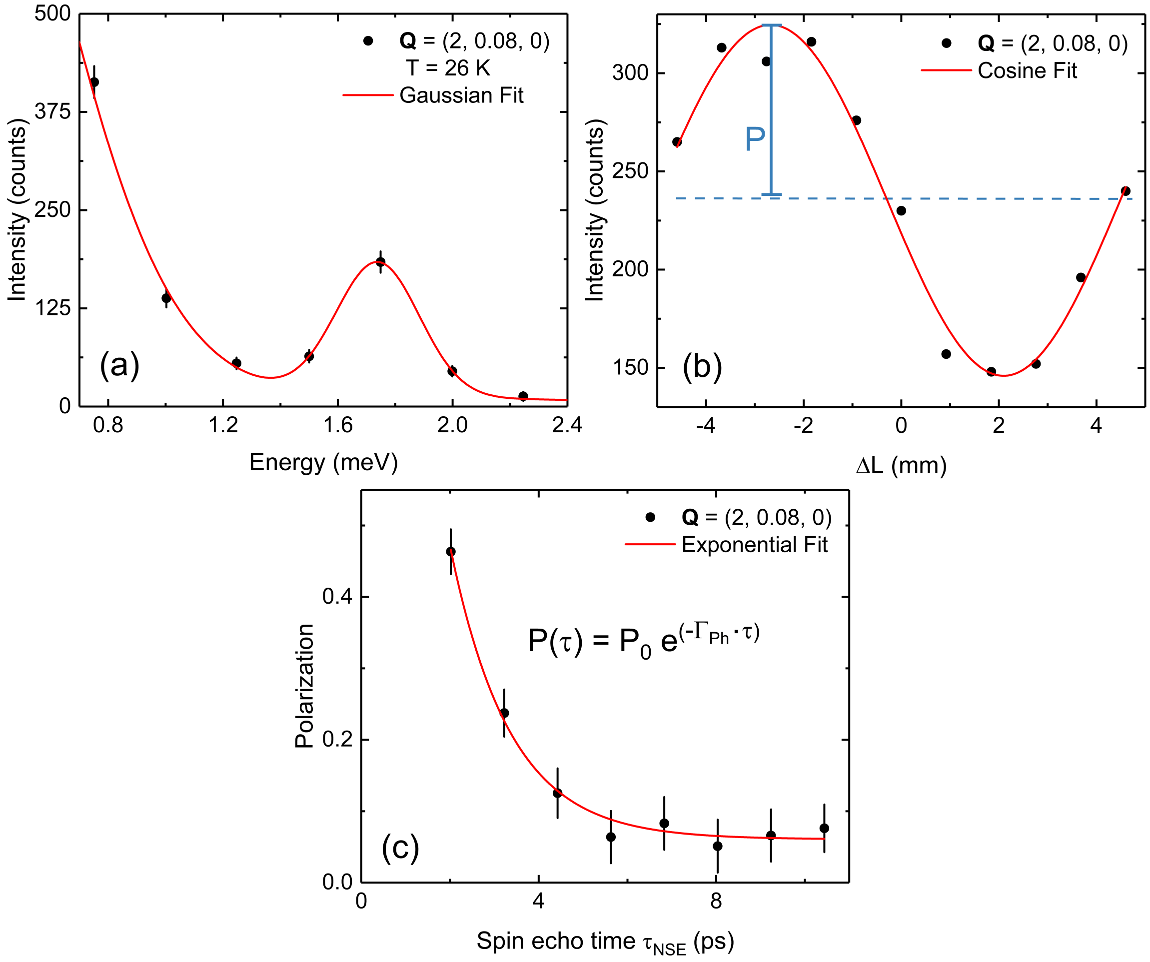

Figure 2.8: Typically routine of data acquisition for phonon measurements using the NRSE technique for the example of a phonon in $Ba(Fe_{1-x}Co_x)_2As_2$. (a) From a regular triple axes measurement the phonon wave vector and the energy for the NRSE measurements can be deduced. The angles of the spectrometer are set to the appropriate positions for the phonon in $\mathbf{q}$ and E and will not be changed during the following measurements. (b) The precession field in the second arm of the spectrometer gives rise to oscillations in the intensity at the detector. With Equation 2.28 the polarization for a specific τ_{NSE} can be determined. (c) With the polarization for various spin echo times τ_{NSE} and Equation 2.27 the intrinsic phonon linewidth can be found.

2.6 Lattice dynamical calculations

This chapter will give a short introduction to density functional theory (DFT) which has been used to study the lattice dynamics of $LaCoO_3$. A more detailed description of this method can be found in literature [28, 29, 30]. DFT is based on the Hohenberg-Kohn theorem, which states that the properties of the ground state of a system consisting of N interacting electrons can be described unambiguously by the electron density distribution $n(\mathbf{r})$ [31]. It can be shown that there is an universal functional $F[n(\mathbf{r})]$ of the electron density distribution that the functional

$$E[n] = F[n] + \int n(\mathbf{r})V(\mathbf{r})d\mathbf{r} \tag{2.29}$$

is minimized by the correct electron density distribution to the associated external potential $V(\mathbf{r})$. This is under the constraint that the integral over $n(\mathbf{r})$ is equivalent with the total number of electrons N. Furthermore the resulting minimum corresponds to the energy of the ground state of the system. With this method the system described by wave functions with $3N$ independent variables can be reduced to a problem with only three independent variables in the electron density distribution. The fact that the functional F is unknown can be solved by the Kohn-Sham equations which project the system on a corresponding system of non interacting electrons [32]. Another assumption made by Kohn and Sham is that each small volume of the system contributes the same amount to the exchange energy as the same volume of an homogeneous electron gas with the same density. This is the so called Local Density Approximation (LDA). If the electron spin is taken into account the electron density $n(\mathbf{r})$ can be written as $n(\mathbf{r}) = n_{\uparrow}(\mathbf{r}) + n_{\downarrow}(\mathbf{r})$ by using the spin densities. Using this Local Spin Density Approximation (LSDA) magnetic ground states can also be described [30]. Although the LDA is quite successful describing weakly correlated electron systems it has some significant weaknesses. Most importantly the binding forces are overestimated by about 20 %. The Generalized Gradient Approximation (GGA) avoids this problem by taking the gradient of the electron density distribution $\nabla n(\mathbf{r})$ into account [33, 34].
With the adiabatic approximation the dynamic properties of the lattice can be determined by a linear response of the electronic system to a perturbation due to a displacement of the atoms relative to their position of equilibrium. This expansion of the DFT to the so called Density Functional Perturbation Theory (DFPT) allows the decoupling of responses to perturbations with different wavelengths [35, 36]. This helps to calculate the phonon energies of a desired wave vector $\mathbf{q}$ without the need of using super cells. For metallic systems, where occupied and unoccupied states can be separated clearly for a vanishing electronic temperature, the DFPT can be used directly. To describe the Fermi surface in an appropriate way a huge amount of values in $\mathbf{k}$ space is needed. To get numerical convergence every Kohn-Sham energy level is

broadened by a smearing function

$$\delta_{\mathrm{sigma}}(\epsilon) = \frac{1}{\sigma}\tilde{\delta}\left(\frac{\epsilon}{\sigma}\right) \tag{2.30}$$

where $\tilde{\delta}$ is an arbitrary function normalized to one so that it will become a δ function in the limit of vanishing smearing parameter σ. The resulting density of states is then given by a convolution of the initial density of states with the smearing function.

Chapter 3

$\mathbf{LaCoO_3}$

The longstanding scientific interest in $LaCoO_3$ and its related compounds [37] is based on intriguing physical behavior relevant for fundamental research as well as for potential applications, e.g. in spintronic [38] or thermoelectric devices [39]. Furthermore when the high temperature superconductivity in layered cuprates was discovered in 1986 [40] huge interest arose in other 3d metal oxides with a perovskite structure like $LaCoO_3$ cobaltates [41] with its strong electron correlations. Hall marks of cuprates such as stripes [42] and the hour-glass dispersion [43, 44, 45] of magnetic excitations have been observed as well. After decades of study a definite consensus on the question of the cobalt spin state evolution has not emerged. This issue will be discussed in detail in Chapter 3.1.2.

A proposed static order of the different spin states, i.e. low-spin ($S = 0$), intermediate spin ($S = 1$) and high spin ($S = 2$), could not be found experimentally. More recent models suggest that spin states form a 3D checkerboard-type dynamic short range order near room temperature, a so called breathing mode (due to different sizes of the different spin states). The idea to test this proposal is to explore the lattice dynamical response around the ordering wave vector, which is in the pseud-cubic notation of the perovskite just $\mathbf{q} = (0.5, 0.5, 0.5)$.

This idea is based on previous investigation of Michael Maschek in his doctorate thesis on charge order in colossal magnetoresistive (CMR) manganite $La_{1-x}Sr_xMnO_3$ [46, 47]. In CMR manganites an ordering of Jahn-Teller active Mn^{3+} and Jahn-Teller inactive Mn^{4+} ions yields a characteristic set of oxygen displacements and, for a narrow range of doping values, leads to a checkerboard-type superstructure. It was found that low-energy acoustic phonon modes are sensitive to fluctuations of this type of charge and orbital order even if no superlattice peak can be observed in purely elastic scattering. On the basis of the results on manganites, we investigated phonons at and close to the proposed ordering wave vector of Co spin states, i.e, $\mathbf{q} = (0.5, 0.5, 0.5)$ and looked for anomalous behavior primarily as function of temperature across the two crossovers in the range $5\,\mathrm{K} \leq T \leq 700\,\mathrm{K}$. Furthermore, we investigated Co-O bond stretching phonons. The atomic displacement pattern of this phonon mimics the proposed one introduced by an 3D checkerboard-type order of Co HS and LS states.

3.1 Scientific background and motivation of the project

3.1.1 Basics

In this section the focus will be on the structural properties and basic physical features of $LaCoO_3$.

The valence formula is $La^{3+}Co^{3+}O_3^{2-}$ with the same valence for the rare-earth and the transition element. It was shown that $LaCoO_3$ exhibits a rhombohedrally distorted perovskite-structured lattice [48, 49] (Fig. 3.1). Perovskite compounds share the general formula ABX_3 with two cations A and B with a large difference in size (A atoms are larger than B atoms) and an anion X bonding to both cations [50]. The ideal structure is cubic. Depending on the relative size of the ions a slight distortion emerges. $LaCoO_3$ exhibits a rhombohedral distortion visible in a tilt of the CoO_6 octahedra at all temperatures investigated in this work [Fig. 3.1(b)]. More details on the structure can be found in Chapter 3.2.2 where the results of the diffraction experiments are shown.

The cobalt ions are surrounded by six oxygen atoms which together form CoO_6 octahedra that are rhombohedrally distorted along the cubic (111) direction. The angle of the Co-O-Co bond is $\approx 163\,^\circ$ and the Co-O bond length 1.93 Å [51]. The unit cell can be assigned to the spatial group $R\bar{3}c$, D_{3d}^6 [41].

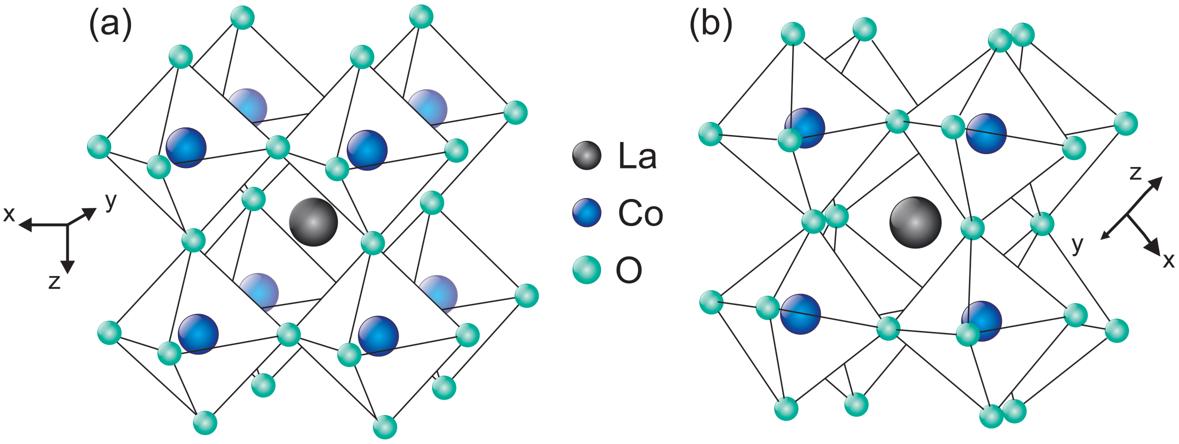

Figure 3.1: Schematic drawing of the crystal structure of $LaCoO_3$. (a) Ideal cubic perovskite structure. (b) Actual rhombohedrally distorted structure.

The lattice of $LaCoO_3$ shows an interesting temperature dependent thermal expansion (Fig. 3.2) [52, 53]. Slightly below 100 K there is a sharp peak in both the thermal expansion of the crystal lattice and the Co-O bond distance. Another maximum for both quantities can be observed above 500 K – 600 K.
The temperatures of the maxima correlate with anomalies in the magnetic susceptibility and conductivity [54]. The susceptibility $\chi(T)$ shows two broad maxima at $T_1 \approx 100$ K and $T_2 \approx 500$ K (Fig. 3.3).

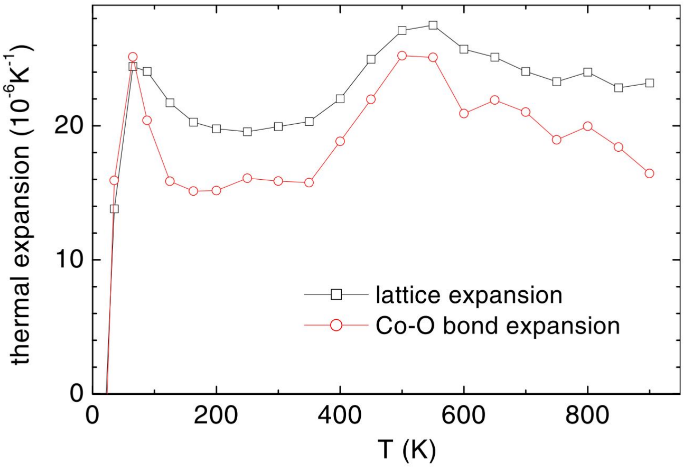

Figure 3.2: Comparison of the lattice (black squares) and Co-O bond distance (red circles) [52].

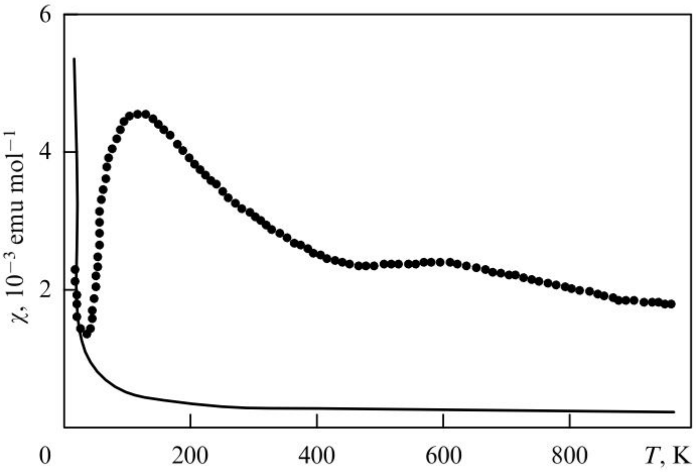

Figure 3.3: Temperature dependence of the the magnetic susceptibility of $LaCoO_3$ [55]. The solid line shows the contribution of magnetic impurities [41].

The second crossover is associated with a metal-insulator crossover ($T_2 \hat{=} T_{\mathrm{MI}} \approx 500\,\mathrm{K}$) whereas the origin of the first peak has remained elusive for decades [56, 57]. It is now widely accepted to be a result of the thermally activated spin-state crossovers of the Co ions ($T_1 \hat{=} T_{\mathrm{SS}} \approx 100\,\mathrm{K}$). In literature the crossovers are also often referred to as transitions. Within this work the term crossover will be used due the broad temperature range of the anomalies in most physical properties. The evolution of the spin states was also object of decade long debates and in the following Chapter 3.1.2 the original and current points of view on this topic will be reviewed.

3.1.2 Original and current point of view on evolution of spin states in LaCoO$_3$

The electron configuration of the Co^{3+} ions is [Ar]$3d^6$. The six $3d$ electrons have to occupy the available three t_{2g} and two e_g orbitals. For low temperatures LaCoO$_3$ is nonmagnetic ($\chi \approx 0$, see Fig. 3.3) indicating that all six $3d$ electrons of the Co^{3+} ions are in the t_{2g}^6 orbitals (see Fig. 3.4). This spin configuration has a total spin $S = 0$ and is therefore called low spin state (LS, $t_{2g}^6 e_g^0$). In this region the material is a diamagnetic insulator. With increasing temperature other spin states are populated, there are two other possible spin states: the intermediate spin state (IS, $t_{2g}^5 e_g^1$, $S = 1$) and the high spin state (HS, $t_{2g}^4 e_g^2$, $S = 2$) (Fig. 3.4).

The crossovers at around 100 K and 500 K in LaCoO$_3$ are typically associated with gradual crossovers from the LS to excited spin states. However the nature of the excited state which is responsible for the spin state crossover has been under debate for quite some time. Goodenough originally proposed that this is the HS state [57], but other groups like Korotin *et al.* [58] suggested that this state is rather the IS state based on their local density approximation calculations.

Two possible scenarios were considered to solve the issue of the spin state population for LaCoO$_3$ with increasing temperature. The first one proposes that the IS state does not exist at all and that the two crossovers are transitions from a pure LS state to a mixed LS/HS state and to a pure HS state for high temperatures, respectively. Another possibility that is very popular is the crossover from pure LS states to IS states at $T_{\mathrm{SS}} \approx 100\,\mathrm{K}$ and then for $T > 500$ from IS states to a pure HS state. The discussion about the spin state issue is still ongoing but there is a lot of evidence that the excited state is the HS state and that the evolution of the spin state is from LS to a LS/HS mix for the crossover at T_{SS}. The population of the HS states increases further on heating up to a LS/HS ratio of about 50:50 [38]. The different spin states form a dynamic ordering that is broken at the second crossover at T_{MI}. This scenario is supported both by experiment [38, 59, 60] and theory [61, 62, 63]. The different states not only differ in the configuration of their spins but also in the size of the Co^{3+} ions. The radii of the cobalt atoms increase from $r_{\mathrm{LS}} = 0.545\,\mathrm{\AA}$ for the LS state to $r_{\mathrm{IS}} = 0.56\,\mathrm{\AA}$ for the

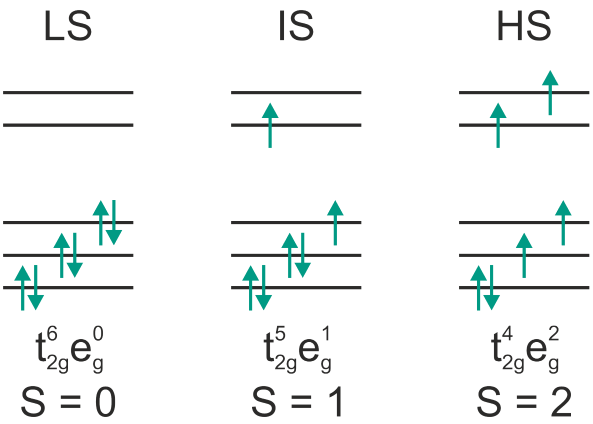

Figure 3.4: Schematic drawing of the possible spin states of the Co^{3+} ions in $LaCoO_3$. There are three different possible spin states: the low spin state (LS, $t_{2g}^6e_g^0$), the intermediate spin state (IS, $t_{2g}^5e_g^1$, $S = 1$) and the high spin state (HS, $t_{2g}^4e_g^2$, $S = 2$).

IS state and $r_{\mathrm{HS}} = 0.61\,\text{Å}$ for the HS state, which is a change of more than 10 % from LS to HS. The size of the CoO_6 octahedra is likewise effected and increases with the population of higher spin states of the cobalt ion, since the oxygen atoms are moved away from the HS states towards the LS states. One of the first models by Goodenough [57] assumed a static long-range 3D alternating ordering between LS and HS states. However it could not be observed experimentally.

Theoretically the crystal field, which controls the energy differences between the multiplets and therefore the population of the three different spin states, should be reduced by the spin crossover and the accompanied expansion of the Co-O bond, but it was found to increase with temperature [64]. This feature could be explained by an effective repulsion between the HS sites which results in an attraction between HS and LS sites [62, 65, 66]. This attractive super-exchange interaction between HS and LS states could be the driving force for the formation of a theoretically proposed dynamically ordered superstructure of LS and HS atoms that is often referred to as spin-state disproportionation [Fig. 3.5(a)] [63]. Furthermore the response of the lattice might act as a positive feedback for the generation of more local moments, e.g. HS states. On the other hand the addition of further local moments gets harder the more local moments are already in the system due to the repulsive interaction between HS sites [64]. This leads to the assumption that there is a short range dynamic LS-HS order in the intermediate temperature region and that there is an energetically most favorable ratio of LS to HS sites roughly around 50:50. It is assumed that the HS and LS sites form a so called checkerboard pattern [Fig. 3.5(b)] in this region which is widely supported by theory [67, 63, 68]. The second crossover at $T_{\mathrm{MI}} \approx 500\,\mathrm{K}$ can be seen as a melting of the LS-HS

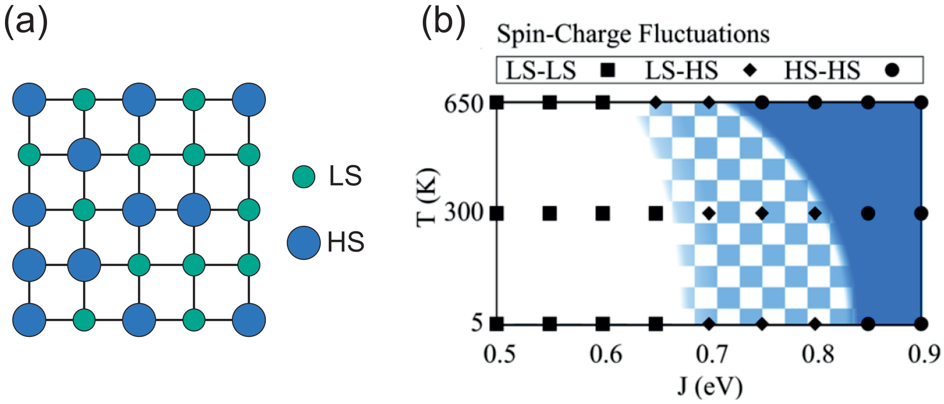

Figure 3.5: (a) Schematic view of dynamical spin-state disproportionation in LaCoO$_3$ according to the model described in the text above (see [69]) (b) Phase diagram as a function of the lattice temperature and the Hunds rule coupling J for $U = 3\,\text{eV}$. The colored parts illustrate different regions, white indicating LS and blue HS. The checkerboard pattern is indicating the LS-HS phase where strong spin-charge fluctuations are present. [67]

order which would also explain the reported anomalous lattice expansion (see Fig. 3.2) due to the breaking of attractive LS-HS bonds. Experimentally a static LS-HS order was never confirmed, but a dynamic order was proposed from the beginning [70, 71]. In this picture the spin states change dynamically between LS and HS and, hence, the size of the Co ions and the CoO$_6$ octahedra fluctuates as well. Due to the favorable alternating positions of LS and HS in a checkerboard-like manner the resulting fluctuations look like a breathing mode where the oxygen atoms all move towards the central Co LS ion or move away/out from the central Co HS ion. In a snapshot, we find that a large Co$_{\text{HS}}$-O$_6$ octahedra is surrounded (in 3D) by 6 small Co$_{\text{LS}}$-O$_6$ octahedra (see Fig. 3.6 for a 2D scheme).

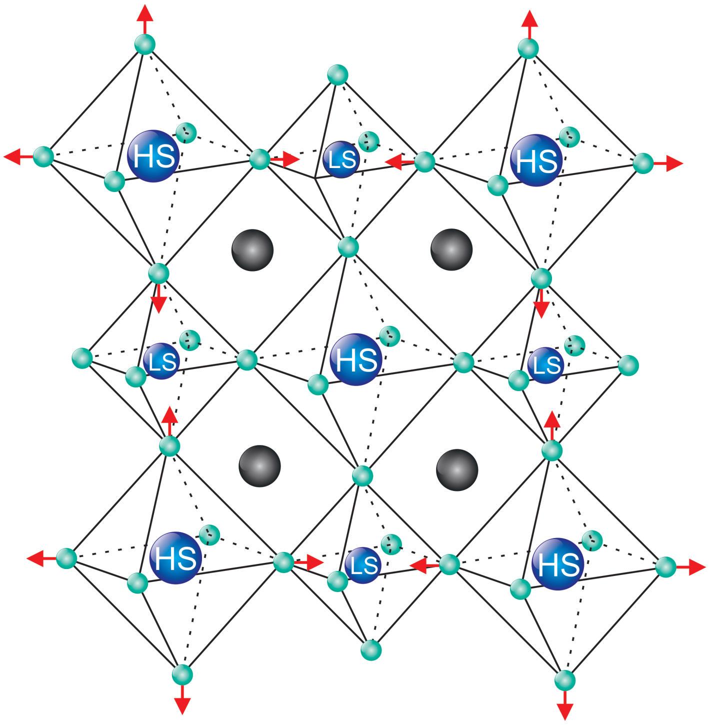

Figure 3.6: Schematic drawing of the breathing distortion of the crystal lattice of $LaCoO_3$ for a plane of CoO_6 octahedra.

3.1.3 Previous experimental results on lattice dynamics and spin-state ordering in $LaCoO_3$

The previous section shows that the question of the spin-state ordering has been a focal point on research in $LaCoO_3$ for a long time. Here, we want to present some previous results defining the background and starting point of our study:

- S.M. A. Señarís-Rodríguez, J. B. Goodenough
  $LaCoO_3$ Revisited
  Journal of Solid State Chemistry **116**, 224 (1995)
  Evolution of spin states defines five different T domains similar to our results [72]

- M. W. Haverkort, Z. Hu, J. C. Cezar, T. Burnus, H. Hartmann *et al.*
  Spin State Transition in $LaCoO_3$ Studied Using Soft X-ray Absorption Spectroscopy and Magnetic Circular Dichroism
  Physical Review Letters **97**, 176405 (2006)
  Population of HS states is closely linked to crossovers [38]

- A. Doi, J. Fujioka, T. Fukuda, S. Tsutsui, D. Okuyama, Y. Taguchi *et al.*
  Multi-spin-state dynamics during insulator-metal crossover in $LaCoO_3$
  Physical Review B **90**, 081109 (2014)
  Second study on population of HS states [69]

- P. G. Radaelli, S. W. Cheong,
  Structural phenomena associated with the spin-state transition in $LaCoO_3$
  Physical Review B **66**, 094408 (2002)
  Powder diffraction data as comparison to compare with our single crystal diffraction data [51]

- T. S. Naing, T. Kobayashi, Y. Kobayashi, M. Suzuki *et al.*
  Ultrasonic Measurement of $LaCoO_3$ *- Evidence for the Orbital-Order Fluctuation*
  Journal of the Physical Society of Japan **75**, 084601 (2006).
  Elastic constants (closely linked to lattice dynamics) sensitive to crossovers [73]

- Kichizo Asai, Osamu Yokokura, Nobuhiko Nishimori, Henry Chou *et al.*
  Neutron-scattering study of the spin-state transition and magnetic correlations in $La_{1-x}Sr_xCoO_3$ *(*$x = 0$ *and 0.08)*
  Physical Review B **50**, 3025 (1994)
  Polarized neutron study can help to interpret our results [56]

- Y. Kobayashi, Thant Sin Naing, M. Suzuki, M. Akimitsu, K. Asai *et al.*
  Inelastic neutron scattering study of phonons and magnetic excitations in $LaCoO_3$
  Physical Review B **72**, 174405 (2005)
  One of the rare INS studies on $LaCoO_3$ [74]

Señarís-Rodríguez *et. al* [72] studied the magnetic and transport measurements of single phase $LaCoO_3$ and distinguish five different temperature domains:

- $0\,K < T < 35\,K$: Below $T \approx 35\,K$ (see also [75]) $LaCoO_3$ is insulating and all of the cobalt ions in the bulk are LS. Only a few surface atoms are in the HS configuration and give a weak contribution to ferromagnetism.

- $35\,K < T < 110\,K$: Cobalt ions gradually populate HS states on increasing temperature. The ratio of HS to LS ions stays below 0.5 due to the restriction of LS near neighbors of HS sites caused by smaller covalent bonding between different spin states compared to the bonding between equivalent Co sites.

- $110\,K < T < 350\,K$: A population of HS/LS states around 50:50 is stabilized in a proposed dynamically short-range ordered semiconducting phase. The order limits the creation of further HS in this temperature regime.

- 350 K $<$ T $<$ 650 K: Besides the dynamically ordered semiconducting phase a metallic coexisting phase is formed by the population of IS from the remaining LS states.
- $T \geq 650\,K$: For the high temperature range a homogeneous (poor) metallic phase contains HS cobalt states in an ordered array alternating with cobalt ions in the IS state.

This model of five different temperature domains explains a number of the physical properties in $LaCoO_3$. For the classification of these domains it is not essential whether the IS state is populated like Señarís *et. al* suggest or the melting of the short-range ordered phase is responsible for the second crossover. In Chapter 3.3 it is discussed how the five suggested domains fit into our model of a LS to LS/HS spin state evolution and to the experimental data.

Several groups focused on the population of excited states. Haverkort *et al.* [38] used x-ray absorption spectroscopy (XAS) to determine the HS state population as a function of the temperature [Fig. 3.7(a)]. Doi *et al.* [69] measured temperature dependence of the HS state or IS state population with inelastic x-ray scattering (IXS) [Fig. 3.7(b)]. Both studies show the same behavior. The excited cobalt states are populated above $T \approx 35$ K. On heating towards 150 K the population increases with an nearly linear slope that slows down in the range from 150 K $\leq T \leq$ 450 K. Above the second crossover there is no IXS data and the XAS data has quite large error bars but it suggests that the population of excited states exhibits a further increase on heating.

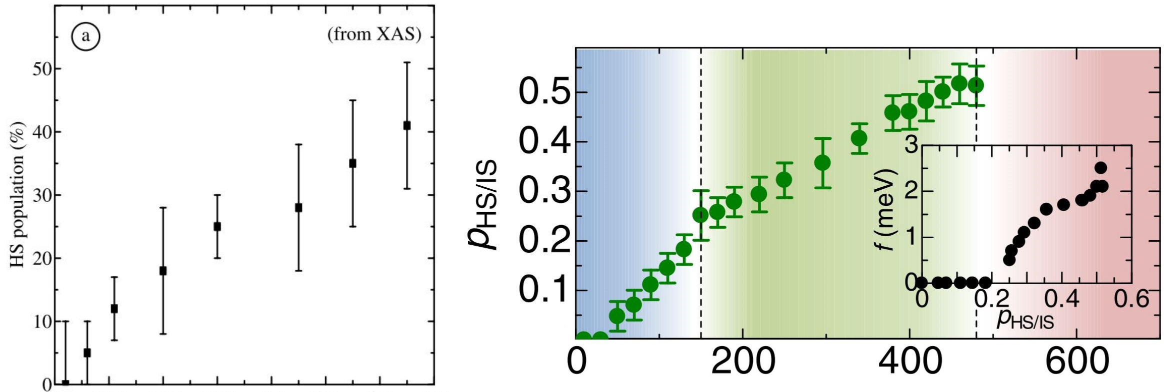

(a) X-ray absorption spectroscopy (XAS) [38]

(b) Inelastic x-ray scattering (IXS) [69]

Figure 3.7: HS population from (a) x-ray absorption spectroscopy XAS data and (b) inelastic x-ray scattering (IXS). The inset shows the fluctuation energy f as a function of the excited state population $p_{\mathrm{HS/LS}}$.

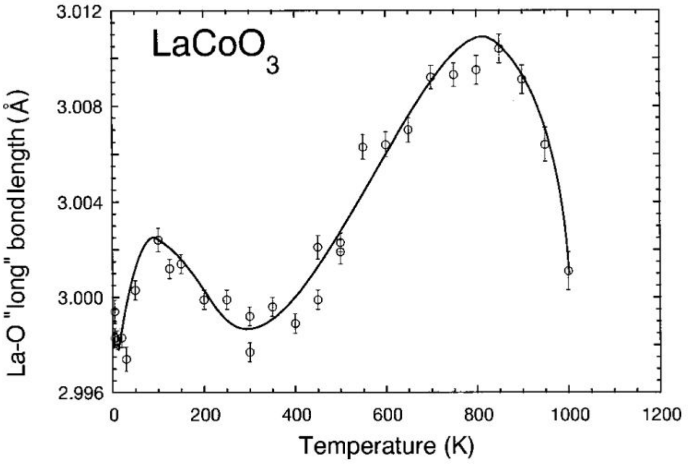

Figure 3.8: Temperature dependence of the long threefold degenerate La-O bond length in LaCoO$_3$, as determined from neutron powder diffraction data. The solid line is a guide to the eye. [51]

Another parameter that shows interesting behavior in the temperature range of the two crossovers is the long threefold degenerate La-O bond length (Fig. 3.8) [51]. For other perovskites it typically has a very weak and monotonic temperature dependence due to the very sensitive competition between the expansion of the whole lattice (expanding all bonds) and the untilting of the oxygen octahedra (shortening one bond). In LaCoO$_3$ this competition leads to a very high sensitivity of the longest of the La-O bonds with regard to nonthermal lattice distortions (besides normal lattice expansion). Since both crossovers can be associated with an enormous increase of this bond length Radaelli *et al.* conclude that it is expanding in an anomalous way in the vicinity of the two crossovers. The bond length increases significantly towards the first crossover $T_{\mathrm{SS}} \approx 100\,\mathrm{K}$ where it has a local maximum before increasing on heating towards room temperature. On further heating an increase can be observed until $T \approx 800\,\mathrm{K}$ before the bond length drops down again.

Naing *et al.* determined [73] the effective elastic constant with the help of ultrasonic measurements. Figure 3.9(a) shows the effective elastic constant for the longitudinal and 3.9(b) the transverse ultrasound propagating along [111]. For the longitudinal direction the elastic constant drops down significantly in between $25\,\mathrm{K} \leq T \leq 60\,\mathrm{K}$ before partly recovering until 200 K before decreasing again for higher temperatures. The single domain and multi domain samples both show a similar temperature dependence. For the transverse direction the elastic constant decreases monotonically on heating although the multi domain effective elastic constant is much smaller. For the single domain the first crossover can be clearly observed in the region $40\,\mathrm{K} \leq 100\,\mathrm{K}$ between two regions with a linear temperature dependence below and above.

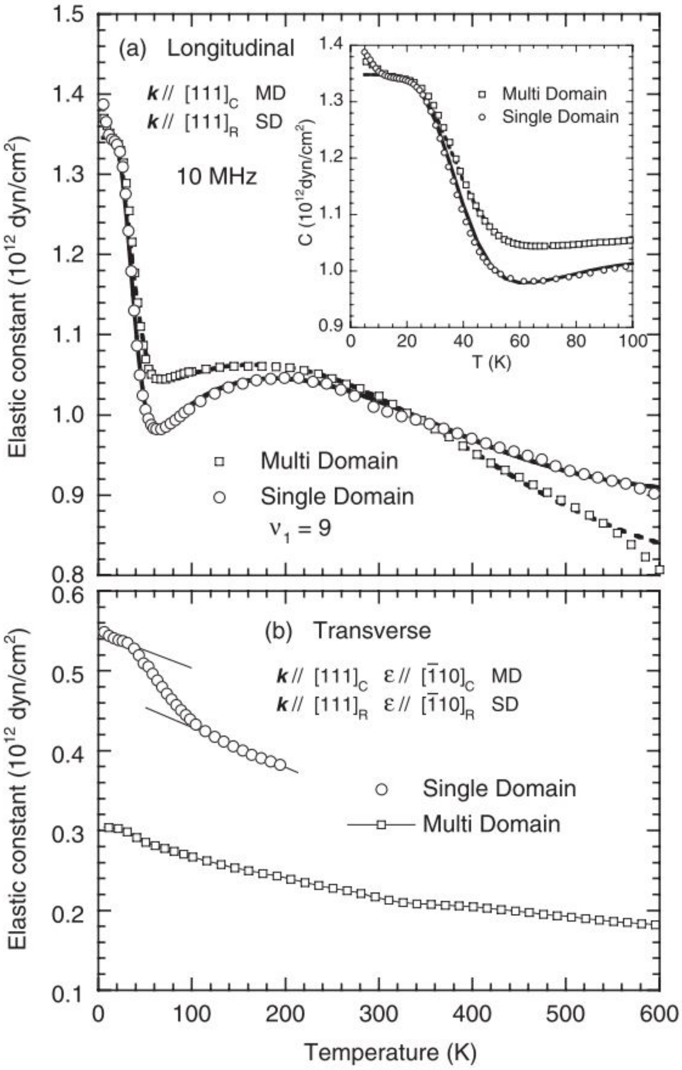

Figure 3.9: Temperature dependence of the effective elastic constant for (a) longitudinal and (b) transverse sounds propagating along the rhombohedral $[111]_R$ direction in single domain and the cubic $[111]_C$ direction in multi domains [73].

As we will discuss in great detail in the chapter on iron-based superconductors (see Chapter 4), the elastic constants are closely connected to the slope of the dispersion of acoustic phonons. This leads to the assumption that the strong anomalies in the elastic constants can also be seen in the lattice dynamics probed, e.g. by, inelastic neutron scattering measurements.

Polarized neutrons were used to determine the temperature dependence of the magnetic scattering in $LaCoO_3$ by Asai *et al.* [56]. The data shown in Figure 3.10 were taken

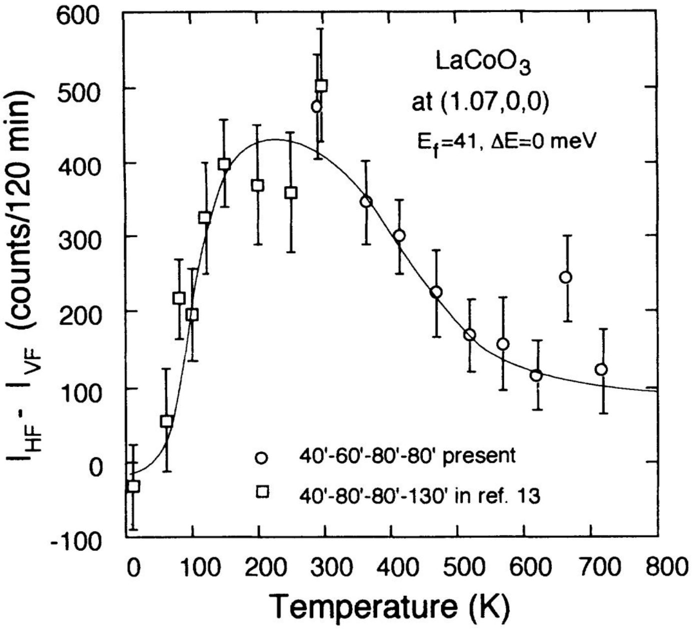

Figure 3.10: Temperature dependence of the paramagnetic scattering cross section at (1.07, 0, 0) with $E_f = 41$ and $\Delta E = 0\,\text{meV}$ for $LaCoO_3$. The solid line is a guide to the eye. [56]

at $\mathbf{Q} = (1.07,\ 0,\ 0)$ with zero energy transfer $\Delta E = 0$. The vertical axis shows the intensity difference between the spin-flipped neutrons scattered in the horizontal-field (HF, parallel to horizontal scattering vector) and the vertical-field (VF, perpendicular to horizontal scattering vector) modes [5]. It increases on heating toward $T \approx 150\,\text{K}$ with a broad maximum and is decreasing for further heating above room temperature. The scattering at this wave vector takes place in the vicinity of a Bragg peak. Hence its character tends to be more paramagnetic-ferromagnetic. It will be instructive to compare our results on phonon renormalization in $LaCoO_3$ with its magnetic properties. Inelastic neutron scattering measurements on a $LaCoO_3$ were performed by Kobayashi *et al.* [74] to study the phonon anomaly associated with the spin-state transition. The data were taken at two different temperatures $T = 8\,\text{K}$ and $200\,\text{K}$ at $\mathbf{Q} = (3 - \delta,\ 1 + \delta,\ 1 + \delta)$ with $E_f = 30.5\,\text{meV}$. The wave vectors here and in the following are given in the pseudo-cubic notation if not stated otherwise (for further discussion see section 3.2.1). For $\delta = 0.5$ the authors find two broad peaks at around $E = 13\,\text{meV}$ and $22\,\text{meV}$ and assign the first one as a rotational mode of the oxygen atoms and the higher energy one with a vibrational mode of lanthanum atoms. The temperature dependence of those phonons is described with a softening on heating. For $\delta = 0.3$ and 0.4 the phonon softening is visible but not as pronounced as at $\delta = 0.5$, a R point

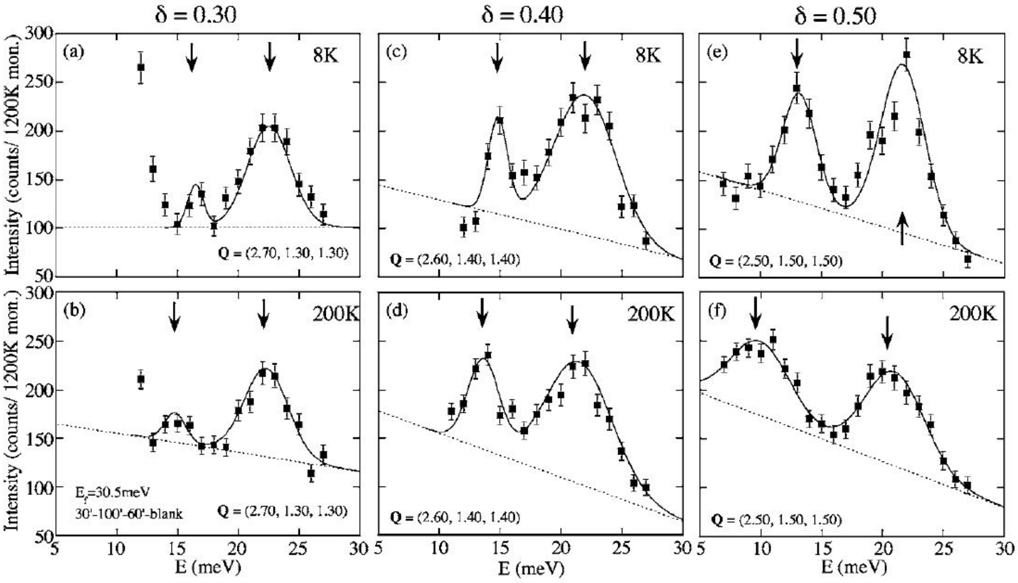

Figure 3.11: Inelastic neutron scattering intensities per 1200 k monitor for $LaCoO_3$ at $\mathbf{Q} = (3 - \delta,\ 1 + \delta,\ 1 + \delta)$ at $T = 8\,\mathrm{K}$ and $200\,\mathrm{K}$ with $E_f = 30.5\,\mathrm{meV}$. The phonon scattering intensity was corrected by the temperature factor. The solid lines are fits to the data using a Gaussian line shape. The arrows indicate the peak positions of the optical phonons. The dotted lines are the background level. [74]

of the pseudo-cubic Brillouin zone, which is a Γ point in the reciprocal lattice for the rhombohedral unit cell due to the Brillouin zone folding.

3.1.4 Key question of our investigations on $LaCoO_3$

The experimental work on $LaCoO_3$ for this thesis focused on inelastic neutron scattering. The basic idea is to indirectly measure a theoretically proposed dynamic short-range order with a proposed ordering vector of $\mathbf{q} = (0.5,\ 0.5,\ 0.5)$ via corresponding signatures in the lattice dynamical properties, i.e., phonons and thermal displacement parameters.

The occupation of spin states of the Co^{3+} ions in $LaCoO_3$ evolves upon heating from LS to HS. The ionic radius depends on the spin state. The crystal lattice participates in the state mixture by the expansion of the CoO_6 octahedra around the larger HS sites. A static LS-HS ordering was proposed in the 1960's [70] but it could not be confirmed experimentally. More recent [63, 64] studies proposed a dynamic short-range LS-HS ordering which leads to a so-called breathing mode of the lattice due to the different ion sizes. The INS measurements focused on the proposed ordering vector

q = (0.5, 0.5, 0.5). Furthermore this INS study is the first to observe effects in the linewidth, e.g. the lifetime of the fluctuations, since previous ones did not have a suitable resolution.

3.2 Results

During this PhD thesis we investigated $LaCoO_3$ with inelastic and elastic neutron scattering as well as x-ray diffraction in order to aqcquire a better understanding of the lattice dynamical properties. A particular focus has been on anomalies possibly related to ordering of Co ions with HS and LS configuration. To this end we performed:

- inelastic neutron scattering at the TAS 1T and PUMA (see Chapter 2.2) in order to determine the phonon dispersion lines, phonon life times and their evolution with temperature.

- diffraction experiments at the neutron diffractometer HEiDi (see Chapter 2.3) and on our lab x-ray diffractometer aiming at the determination of the atomic mean square displacements, which can also be indicators for an incipient or dynamic structural distortion.

The cylindrical $LaCoO_3$ sample used for our investigations was grown by J. F. Mitchell at Argonne National Laboratory using the floating zone technique weighing around 7 g [Fig. 3.12(a)]. Synchrotron x-ray powder diffraction confirmed the pure $LaCoO_3$ phase of the sample. This is supported by our own single crystal XRD discussed later in this work. During our investigation, there appeared a question on the high-temperature behavior of our sample and for that reason we measured also the magnetization in an oven, i.e. for $T > 300\,\mathrm{K}$, to compare it to previous $LaCoO_3$ data. The susceptibility [Fig. 3.12(b)] decreases on heating from 300 K to 1000 K. Around $T = 600\,\mathrm{K}$ it exhibits a local maximum. The behavior of our sample is in good agreement to the previously reported data [55] (Fig. 3.3).

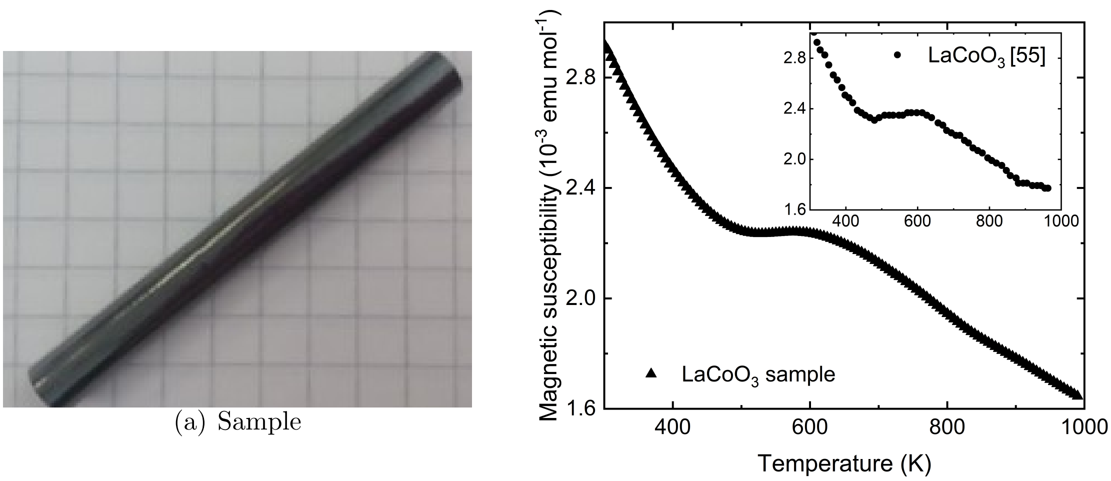

(a) Sample

(b) Susceptibility

Figure 3.12: (a) Cylindrical LaCoO$_3$ sample before it was cut into pieces for various measurements. (b) Magnetic susceptibility of the sample. The inset shows the data by Zobel *et al.* [55].

The outline of the remainder of this chapter will be as follows. In Chapter 3.2.2 we will discuss results from our diffraction studies followed by an in-depth investigation of lattice vibrations in Chapter 3.2.3. In our analysis of the inelastic neutron data we relied heavily on *ab-initio* lattice dynamical calculations performed in the theory group of our institute. These calculations were analyzed within this PhD project and will be presented first before the experimental results.

3.2.1 Analysis of the lattice dynamical calculations

In this section the analysis of the DFTP calculations (see Chapter 2.6), which were done at our institute by Dr. K.-P. Bohnen, will be explained in more detail. The calculations were done within the local density approximation (LDA) based on a rhombohedral nonmagnetic structure. Figure 3.13 shows a calculated phonon dispersion of LaCoO$_3$.

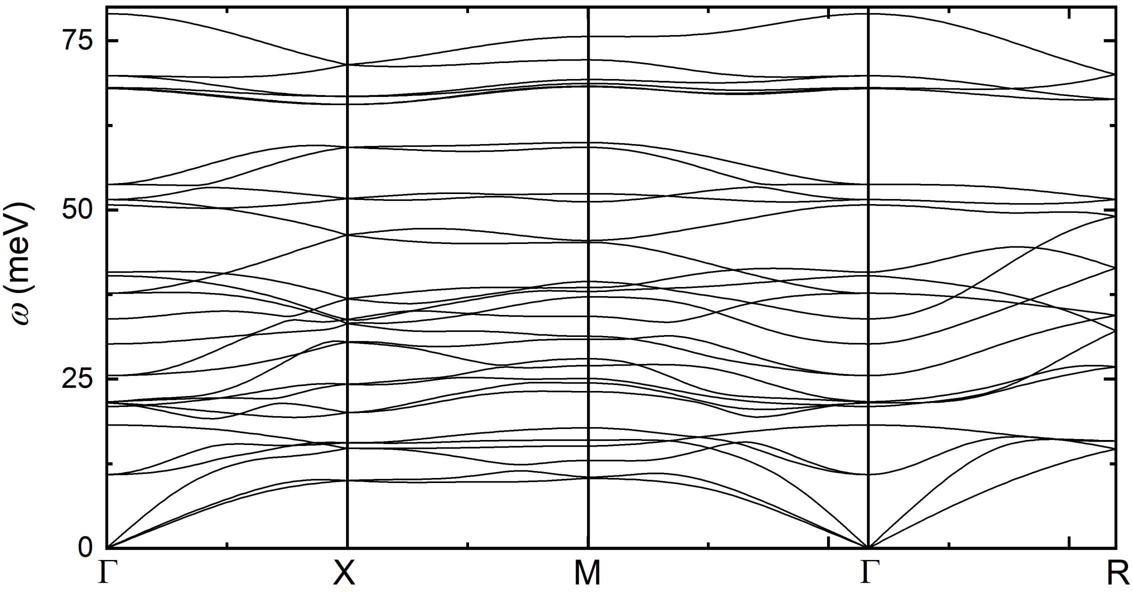

Figure 3.13: Phonon dispersion of LaCoO$_3$ calculated by Dr. K.-P. Bohnen with DFTP calculations using a local density approximation (LDA) based on a rhombohedral nonmagnetic structure.

With the help of the lattice dynamical calculations theoretical predictions of the phonon energies at low temperatures can be made for each energy scan. Using the DFPT calculations the structure factors $\mathcal{F}(\mathbf{Q})$ (see Eq. 2.8) for every single wave vector and its specific phonon energies can be obtained. Since it is proportional to the experimental phonon intensity it can be used to calculate the measured energy scans. The intensity I_{ph} for every single phonon is modeled by a Gaussian peak of the form

$$I_{\mathrm{ph}} \propto \mathcal{F}(\mathbf{Q})/E_{\mathrm{ph}} \cdot \exp(-2.776 \cdot (((x - E_{\mathrm{ph}})/\Gamma)^2)) \tag{3.1}$$

where E_{ph} is the energy of the phonon and Γ its calculated linewidth. The linewidth was calculated using the resolution calculation program *rescal* [76]. As the calculations in this form do not consider temperature effects they are always compared to the low temperature experimental data and the Bose factor has not to be taken into account. The results of the calculations are shown in the next chapters together with the experimental data. At finite temperatures phonon-phonon and electron-phonon interactions cause anharmonic effects. Generally upon increasing temperature they lead to an increase of the phonon linewidth and a softening of the phonon frequency (i.e. decrease of the phonon energy). Therefore a continuous broadening and softening of the phonons can be regarded as normal behavior.
For the measurements the given reciprocal lattice vector is denoted in the represen-

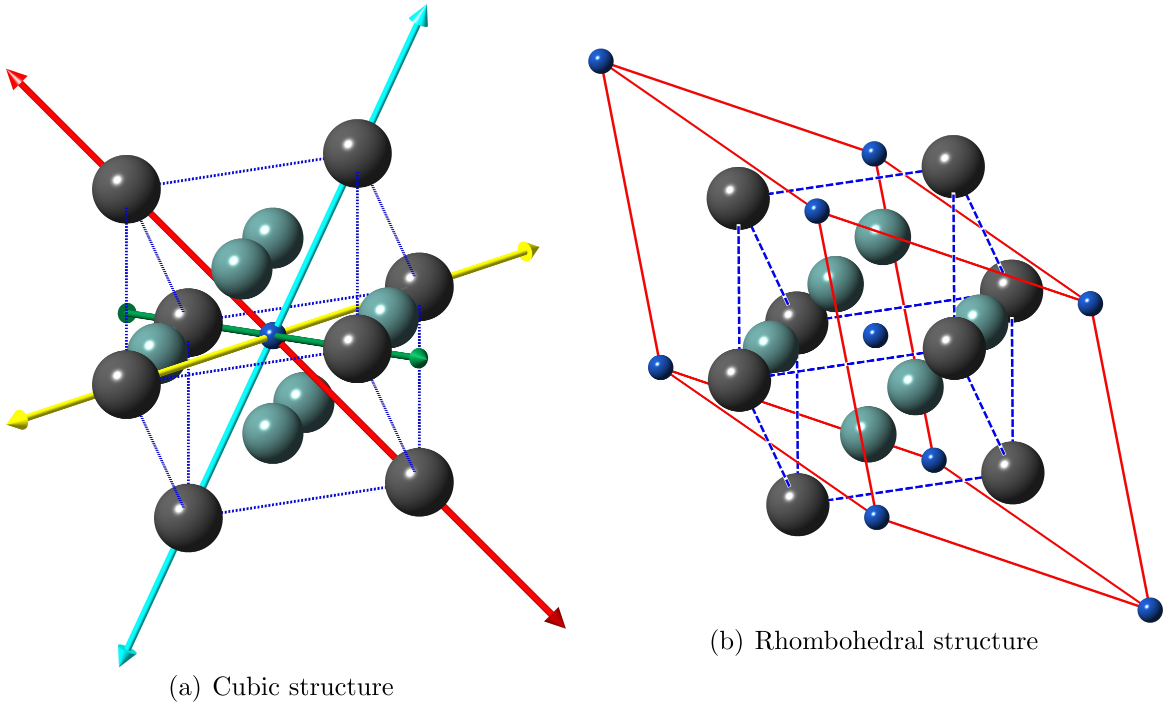
(a) Cubic structure

(b) Rhombohedral structure

Figure 3.14: Comparison of cubic model and the actual rhombohedral crystal symmetries for $LaCO_3$. Cobalt atoms are visualized in blue, surrounded by oxygen octahedra in turquoise and lanthanum atoms in gray. (a) Unit cell (blue dashed line) of $LaCoO_3$ in cubic notation. The arrows indicate the four different directions in which the rhombohedral distortion can take place. These four possibilities for the distortion result in the four different twins in the rhombohedral structure. (b) Unit cell (red line) of $LaCoO_3$ with rhombohedral basis. The blue dashed line shows the pseudo-cubic unit cell.

tation of the pseudo-cubic unit cell setting of $LaCoO_3$ disregarding the rhombohedral distortion. Whereas the lattice dynamical calculations were done with the actual rhombohedral symmetry. Figure 3.14 shows the comparison of the ideal cubic model and the actual rhombohedral crystal symmetries for $LaCO_3$. Cobalt atoms are visualized in blue, surrounded by oxygen octahedra in turquoise and lanthanum atoms in gray. In Figure 3.14(a) the unit cell (blue dashed line) of $LaCoO_3$ in the cubic notation is displayed. The arrows indicate the four different directions in which the rhombohedral distortion can take place. These four possibilities for the distortion result in the four different twins in the rhombohedral structure. Figure 3.14(b) shows the unit cell (red line) of $LaCoO_3$ with the actual rhombohedral basis. The blue dashed line shows the pseudo-cubic unit cell. Before calculating the phonon intensity the cubic notation used for gathering the experimental data has to be converted to the rhombohedral notation with the consideration of all four possible twins (Fig.3.14). At first the wave vector in the pseudo-cubic notation $\mathbf{Q}_c$ has to be transformed into the rhombohedral wave vector $\mathbf{Q}_{rh}$ with the following transformation matrix:

$$\mathbf{Q}_{\mathrm{rh}} = \begin{pmatrix} -2 & 2 & 2 \\ 2 & -2 & 2 \\ 2 & 2 & -2 \end{pmatrix} \cdot \mathbf{Q}_{\mathrm{c}} \tag{3.2}$$

With the first new rhombohedral wave vector $\mathbf{Q}_{\mathrm{rh},1}$ the other three equivalent twins $\mathbf{Q}_{\mathrm{rh},2}$, $\mathbf{Q}_{\mathrm{rh},3}$ an $\mathbf{Q}_{\mathrm{rh},4}$ can now be calculated by repeatedly multiplying it with the following twinning matrix:

$$\mathbf{Q}_{\mathrm{rh},i+1} = \begin{pmatrix} 1 & 0 & -1 \\ 1 & 0 & 0 \\ 1 & -1 & 0 \end{pmatrix} \cdot \mathbf{Q}_{\mathrm{rh},i} \qquad \text{with} \qquad i \in \{1, 2, 3\} \tag{3.3}$$

If the fourth twin $\mathbf{Q}_{\mathrm{rh},4}$ is multiplied with the twinning matrix the result is again$\mathbf{Q}_{\mathrm{rh},1}$. The two operations (Eq. 3.2 and Eq. 3.3) to transform the wave vectors from the pseudo-cubic notation used for the measurements to the actual rhombohedral wave vectors were carried out on all measured wave vectors and are displayed in the following table 3.1:

Table 3.1: Measured wave vectors in cubic notation $\mathbf{Q}_c$ and equivalent wave vectors in rhombohedral notation including all for twins $\mathbf{Q}_{\mathrm{rh},i}$.

$\mathbf{Q}_c$	$\mathbf{Q}_{\mathrm{rh},1}$	$\mathbf{Q}_{\mathrm{rh},2}$	$\mathbf{Q}_{\mathrm{rh},3}$	$\mathbf{Q}_{\mathrm{rh},4}$
(1.5, 1.5, 1.5)	(3, 3, 3)	(0, 3, 0)	(0, 0, -3)	(3, 0, 0)
(1.6, 1.6, 1.6)	(3.2, 3.2, 3.2)	(0, 3.2, 0)	(0, 0, -3.2)	(3.2, 0, 0)
(2.5, 2.5, 2.5)	(5, 5, 5)	(0, 5, 0)	(0, 0, -5)	(5, 0, 0)
(1.5, 1.5, 2.5)	(5, 5, 1)	(4, 5, 0)	(4, 4, -1)	(5, 4, 0)
(0, 0, 2)	(4, 4, -4)	(8, 4, 0)	(8, 8, 4)	(4, 8, 0)
(2.5, 1.5, 0)	(-2, 2, 8)	(-10, -2, -4)	(-6, -10, -8)	(2, -6, 4)
(1.75, 1.75, 2.25)	(4.5, 4.5, 2.5)	(2, 4.5, 0)	(2, 2, -2.5)	(4.5, 2, 0)

It is essential to do the calculations based on the actual rhombohedral structure. This becomes obvious when they are compared with those for a cubic crystal structure and the experimental data (Fig. 3.15). In the experimental data a strong phonon peak at $E_{\mathrm{ph}} = 11.85\,\mathrm{meV}$ can be observed which is relatively close to the $E_{\mathrm{ph}} = 10.92\,\mathrm{meV}$ predicted by the rhombohedral calculation especially when it is compared to $E_{\mathrm{ph}} = 16.24\,\mathrm{meV}$ which is the result of the calculation in the cubic case. Furthermore only the rhombohedral calculation explains the feature around 20 meV in the experimental data whereas the cubic calculation strongly overestimates the intensity of the phonon

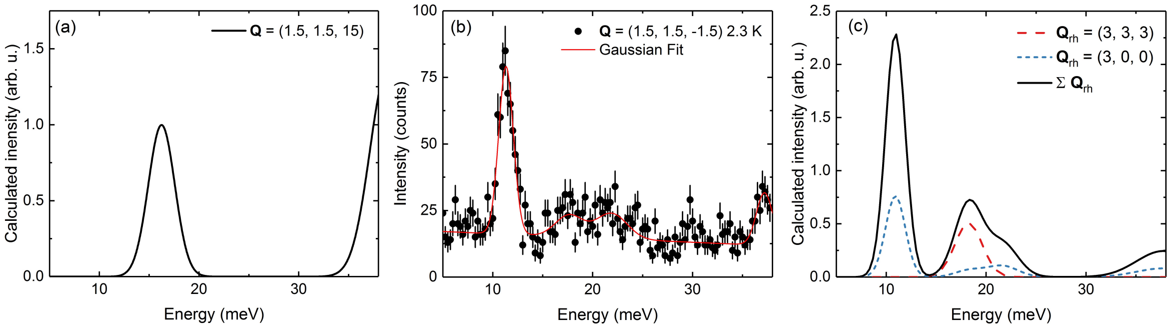

Figure 3.15: Comparison of phonon intensity calculations of $LaCoO_3$ for the pseudo-cubic wave vector $\mathbf{Q}_c = (1.5,\ 1.5,\ 1.5)$. In (a) a cubic and in (c) the actual rhombohedral crystal symmetry was used for the calculations. (b) Experimental data at the equivalent wave vector $\mathbf{Q}_c = (1.5,\ 1.5,\ -1.5)$ obtained from inelastic neutron scattering.

above 35 meV. Hence, the comparison of the experimental data to calculations based on two different crystal structures for $LaCoO_3$ clearly shows that the calculated phonon intensity based on the rhombohedral structure yields a significantly better agreement to the data than the calculations for a cubic crystal lattice. This particular wave vector is only one example to illustrate the superiority and the need of the rhombohedral calculations which can also be observed for other wave vectors.

Although DFPT calculations only provide information for base temperature they can be modified to simulate a temperature dependence of the phonon energies. Using quasi harmonic approximation with temperature dependent lattice parameters obtained from experiments, the influence of temperature on the peak position of the phonons could be studied (Fig. 3.25). For each temperature, different lattice parameters $a = b = c$ are used for the unit cell on which the calculations are based on (Table 3.2). The relative evolution of the lattice parameters with temperature value is based on the experimental diffraction data by Radaelli *et al.* [51].

Table 3.2: Temperature dependent rhombohedral lattice parameters $a = b = c$ used for the quasi harmonic approximation. The relative evolution of the base temperature value is according to the experimental diffraction data by Radaelli *et al.* [51].

T in K	0	200	300	400	600	800
$a = b = c$ in Å	5.261	5.285	5.298	5.311	5.342	5.372

Figure 3.16 shows the example of the temperature evolution of the energy of one specific

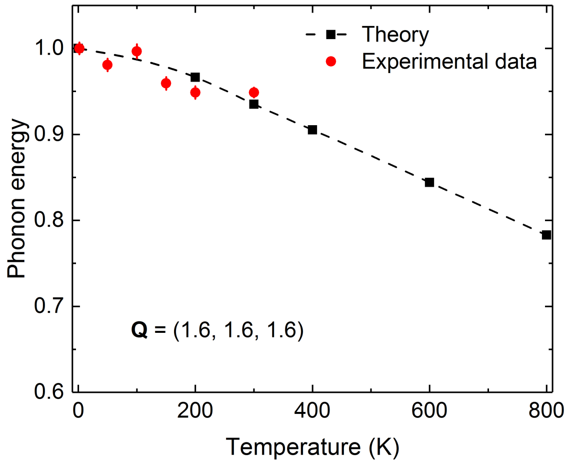

Figure 3.16: Comparison of calculated (black squares) and experimental (red dots) temperature dependence of the normalized energy of a specific phonon at $\mathbf{Q}_c$ = (1.6, 1.6, 1.6) in LaCoO$_3$. The line is a guide to the eye.

phonon at the wave vector $\mathbf{Q}_c = (1.6, 1.6, 1.6)$. The black squares are calculated with the help of the quasi harmonic approximation and the red dots are experimental data. Both data sets show a moderate softening on heating which is, as described earlier, expected to be the usual temperature dependent behavior. In the next chapters the given wave vectors are mostly wave vectors used for the experimental setup. If it is not stated otherwise the vectors have a cubic base and therefore will be written as $\mathbf{Q}_c \equiv \mathbf{Q}$. Wave vectors in the rhombohedral symmetry for the calculations are still marked as $\mathbf{Q}_{\mathrm{rh}}$.

3.2.2 Diffraction

The basic idea of the diffraction measurements was that the expected dynamic order and the accompanied breathing motion of the lattice influences the mean square displacement (MSD) of the atoms in LaCoO$_3$. The mean square displacement is used to quantify the deviation of a particle from its equlibrium position. Due to thermally activated particle motion the MSD should increase continuously on heating. A fluctuating order corresponds to different positions of an particular atom over time. Hence, the MSD of an atom will generally be enhanced if the fluctuations are too fast to be detected within the time resolution of thermal neutrons ($\ll$ ps). If the fluctuations decrease, so should the MSD.

Small pieces of the sample were used for x-ray ($\approx 125\,\mu$m) and neutron (4 mm) diffrac-

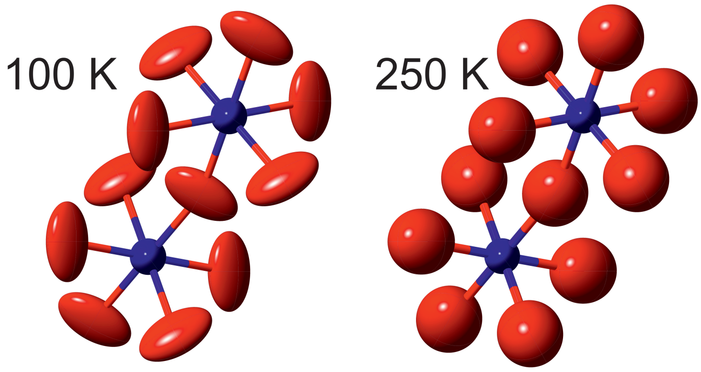

Figure 3.17: Mean square displacement (MSD) of $LaCoO_3$ measured with x-ray diffraction, the cobalt atoms are shown in blue and the oxygen atoms in red. The MSD is shown for two different temperatures, 100 K on the left and 250 K on the right.

tion to observe the temperature dependence of the movement of the atoms in $LaCoO_3$. The first measurements were done on a x-ray diffractometer together with Dr. Michael Merz at our institute. The rhombohedral crystal structure was confirmed for our sample. The x-ray diffraction was carried out in a temperature range from $T = 100 - 250\,\mathrm{K}$ and the focus was on the mean square displacement of the oxygen atoms. Figure 3.17 shows the MSD of the atoms in the CoO_6 octahedra for $T = 100\,\mathrm{K}$ and $T = 250\,\mathrm{K}$. The cobalt atoms are shown in blue and the oxygen atoms in red. The MSD of the cobalt atoms stays more or less constant for the whole temperature range. The MSD of the oxygen atoms exhibits a strong temperature dependence. For $T = 100\,\mathrm{K}$ the oxygen atoms move mostly perpendicular to the Co-O-Co bonds, which seem quite strong and rigid. On heating, the MSD becomes more and more isotropic and the cylindrical shape at $T = 100\,\mathrm{K}$ gradually changes to a sphere at $T = 250\,\mathrm{K}$.

To cover the whole temperature range of both crossovers another experiment at the neutron single-crystal diffractometer HEiDi at the MLZ in Garching (see Chapter 2.3) was performed. The measurement was carried out using a closed cycle liquid He^4 cryostat for $2.5\,\mathrm{K} < T < 300\,\mathrm{K}$ and a furnace for $300\,\mathrm{K} < T < 690\,\mathrm{K}$. Dr. Michael Merz (KIT) and Dr. Martin Meven (MLZ) were strongly involved in the measurements and data analysis.

The data analysis was done using the crystallographic program *JANA2006* [77]. It is a program focused on the solution, refinement and interpretation of even difficult structures. It helps to calculate structures from both powder as well as single crystal data measured with X-ray or neutron diffraction. The input data can be a combination of different data sets of different methods.

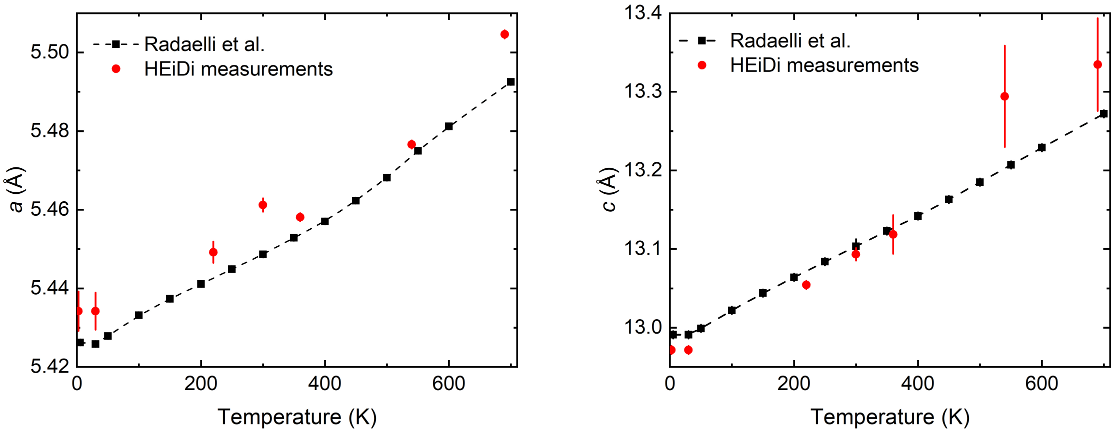

(a) Lattice parameter a (b) Lattice parameter c

Figure 3.18: Lattice parameters (a) a and (b) c of $LaCoO_3$ of the hexagonal unit cell. The single crystal measurements on HEiDi (red dots) are compared to the powder diffraction data by Radaelli *et al.* [51] (black squares). The dashed lines are a guide to the eye.

Figure 3.18 shows the hexagonal lattice parameters a and c obtained from the HEiDi measurements with the help of *JANA2006* (red dots). The comparison of both parameters with neutron powder diffraction data by Radaelli *et al.* [51] (black squares) shows clear deviations. The general temperature dependence of both measurements fits quite well, but the absolute values of our data exhibit a significantly larger scattering due to a different resolution of both methods. However, these effects are in a range that is considered typical for the instrument. Furthermore this does not have a large effect on the refinement and the determination of the MSD. In addition to the lattice parameters the bond lengths can also be determined from the diffraction measurements. The temperature dependence of the longest La-O bond by Radaelli *et al.* [51] was already shown in Figure 3.8. Our neutron single crystal data show deviations from those measurements especially in the low temperature region (Figure 3.19). For temperatures higher than room temperature the absolute values agree quite well. To make further comments on the temperature dependece of the La-O in our study more data points are needed.

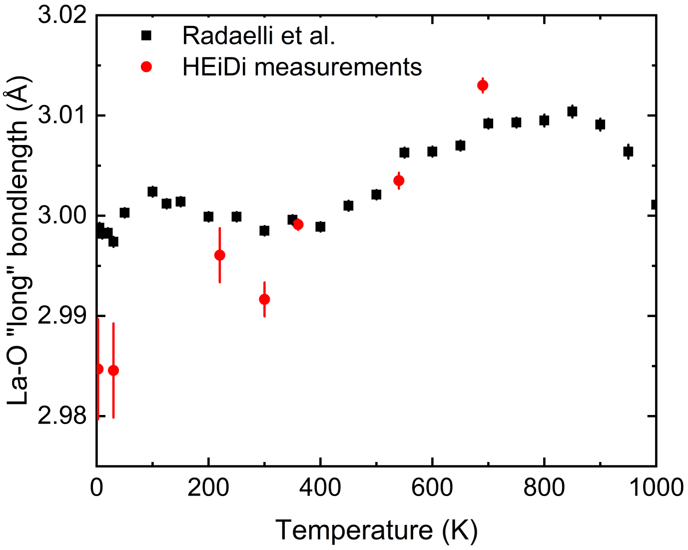

Figure 3.19: La-O bond length in $LaCoO_3$ (see also Figure 3.8. The single crystal measurements on HEiDi (red dots) are compared to the powder diffraction data by Radaelli *et al.* [51] (black squares).

In Figure 3.20 the temperature dependence of the mean square displacement is shown. To determine the MSD a large set of different Bragg peak intensities is measured. Following Equation 2.2 the intensity of the diffraction reflexes is reduced due to thermal displacements from the equilibrium position of the atoms. This reduction is dependent on the Debye-Waller factor $\exp(-W_j)$, with $W \propto \text{MSD} \cdot Q^2$ (see Eq. 2.4). Hence, Bragg peaks with large values for H, K and L are preferred. Therefore hot neutrons are suited perfectly for those kind of measurements due to the possibility of large **Q** transfers.

The upper part of the figure shows a ball stick model of the CoO_6 octahedra to visualize the changes with temperature. The most obvious feature is that the MSD of both atoms, cobalt (blue) and oxygen (red) grows monotonously with increasing temperature. Due to an increased thermal oscillations this is expected. Furthermore the shape of the cobalt displacement changes from cylindrical to spherical on heating from $T = 30\,\text{K}$ to $220\,\text{K}$ above the first crossover. Graphically, one cannot observe a change in the form of the MSD ellipsoid of the oxygen atoms. To get more detailed information the values of the anisotropic MSD along the main different displacement directions can be obtained from the model and can be graphically drawn against the temperature. The lower part of Figure 3.20 shows those values. The temperature dependence of the MSD is shown. The values U1, U2 and U3 correspond to the three main axes of the displacement ellipsoids shown above. For all three elements lanthanum, cobalt and oxygen data can be well-approximated by a smooth, e.g., exponential curve for a wide range of temperatures, except for the values measured at $T = 360\,\mathrm{K}$. This leads to the assumption that there is a temperature region connected to the second crossover at $T_{\mathrm{MI}} \approx 500\,\mathrm{K}$ (shaded areas). Furthermore the MSD of cobalt is anisotropic for low temperatures (below $T_{\mathrm{SS}} \approx 100\,\mathrm{K}$) and becomes isotropic for higher temperatures which was originally proposed for the oxygen atoms but can only be observed for cobalt.

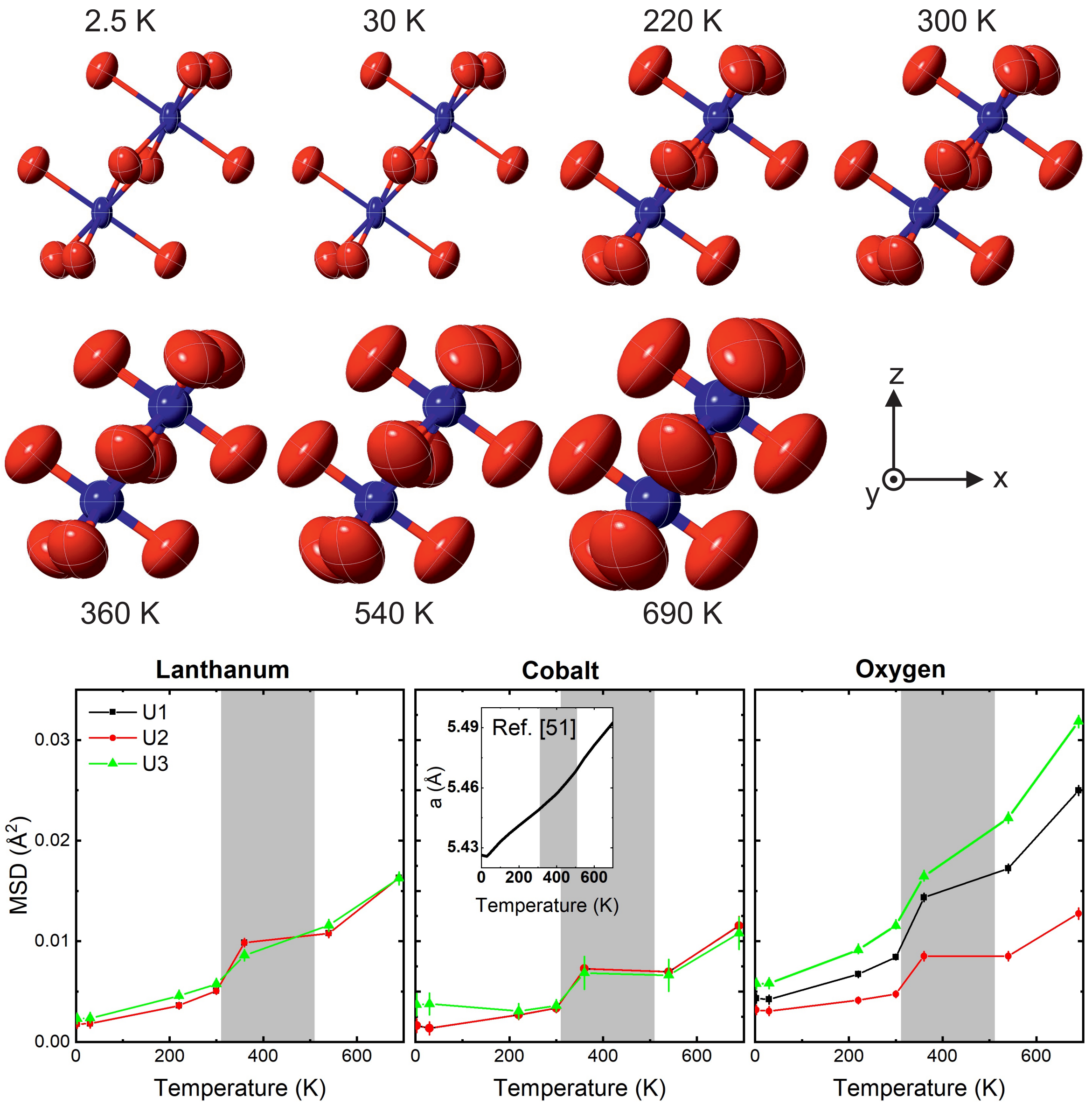

Figure 3.20: Mean square displacement (MSD) of $LaCoO_3$ measured with neutron diffraction. The values U1, U2 and U3 correspond to the three main axes of the displacement ellipsoids shown above.

3.2.3 Inelastic neutron scattering

Low energy phonon measurements at the INS spectrometer 1T

The low energy phonon survey up to 35 meV was done at the thermal triple axis spectrometer 1T at the Laboratoire Léon Brillouin (LLB) at CEA Saclay. A 35 mm long part of the cylindrical sample described in Chapter 3.2 was used for this experiments. The measurements were carried out at a fixed final energy of $E_f = 14.7\,\mathrm{meV}$ in the [1 1 0]-[0 0 1] scattering plane. For the low temperature experiments a small 4 K closed cycle refrigerator system and for higher temperatures a bigger cryostat with an integrated heater which can reach temperatures up to 700 K was used. The collected data points were fitted with several Gaussian functions, one for each observed phonon in each scan. As described in Chapter 3.1.4 the focus was on wave vectors at the zone boundaries along the (111) directions, but also other wave vectors were investigated to look for momentum dependence of phonon renormalization effects for the two crossovers.
At the wave vector $\mathbf{Q} = (1.5, 1.5, 1.5)$ a clear phonon peak can be seen at $E_{\mathrm{ph}} = 11.85\,\mathrm{meV}$, two smaller peaks near 20 meV and another one at over 35 meV [Fig. 3.21(a)]. The peak positions were obtained from a fit consisting of four single Gaussian peaks added up and a linear background. Figure 3.21(b) shows the intensity calculated as described in Chapter 3.2.1 for the same wave vector for comparison. The calculations were carried out for all four twins $\mathbf{Q} = (3, 3, 3)$, $\mathbf{Q} = (3, 0, 0)$, $\mathbf{Q} = (0, 3, 0)$, $\mathbf{Q} = (0, 0, -3)$. Since the results for the latter three are identical the sum for all twins is the combination of $\mathbf{Q} = (3, 3, 3)$ and three times $\mathbf{Q} = (3, 0, 0)$ assuming an equal volume for differently oriented domains. The experiment and the calculation are in reasonable agreement. The peak positions are predicted very well by the calculations as well as the fact that the peak at 11.85 meV is dominating in intensity. The intensity ratio of the peaks around 20 meV does not fit perfectly. One reason might be a slightly unequal distribution of the four different domains. The high energy peak seems to be more narrow in the experiment than in the calculations. This could be due to the incomplete measurement of this peak, the right side was not measured until the intensity was down to the background again. The scan was not carried out to higher energies since at an energy transfer of three times the final energy $3 \cdot 14.7$ a strong spurious signal is expected. For higher energies than shown in the experimental data the energy scan could not be evaluated anymore.

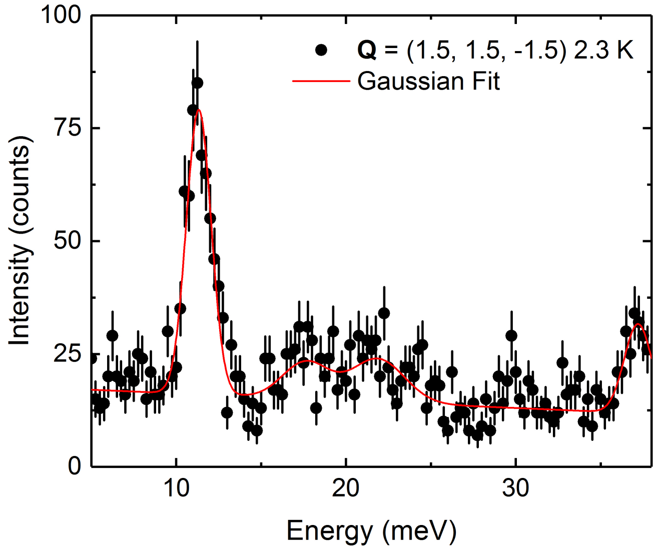

(a) Experimental data

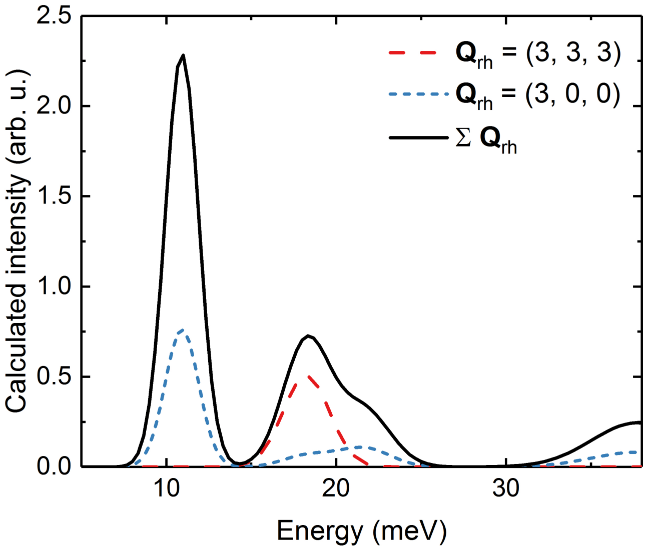

(b) Theoretical calculations

Figure 3.21: (a) Experimental data (black circles) and (b) the calculated structure factor for the wave vector $\mathbf{Q} = (1.5,\ 1.5,\ 1.5)$. The experimental data was taken at 2.3 K at the equivalent wave vector $\mathbf{Q} = (1.5,\ 1.5,\ -1.5)$ to avoid a spurious signal present in the original scan. The raw data was fitted with four Gaussian peaks (red line) analogous to the four peaks in the lattice dynamical calculations. The calculations were carried out for all four twins $\mathbf{Q} = (3,\ 3,\ 3)$, $\mathbf{Q} = (3,\ 0,\ 0)$, $\mathbf{Q} = (0,\ 3,\ 0)$, $\mathbf{Q} = (0,\ 0,\ -3)$. Since the results for the latter three are identical the sum for all twins (black line) is the combination of $\mathbf{Q} = (3,\ 3,\ 3)$ (red dashed line) and three times $\mathbf{Q} = (3,\ 0,\ 0)$ (blue dashed line).

For the wave vector $\mathbf{Q} = (1.6,\ 1.6,\ 1.6)$ a peak at $E_{\mathrm{ph}} = 15.70\,\mathrm{meV}$ can be observed at $T = 2\,\mathrm{K}$ with a broad shoulder on the right side of the peak [Fig. 3.22(a)]. The peak positions were obtained from a fit consisting of two single Gaussian peaks added up and a linear background. The calculations [Fig. 3.22(b)] were carried out for all four twins $\mathbf{Q} = (3.2,\ 3.2,\ 3.2)$, $\mathbf{Q} = (3.2,\ 0,\ 0)$, $\mathbf{Q} = (0,\ 3.2,\ 0)$, $\mathbf{Q} = (0,\ 0,\ -3.2)$. Since the results for the latter three are identical the sum for all twins is the combination of $\mathbf{Q} = (3.2,\ 3.2,\ 3.2)$ and three times $\mathbf{Q} = (3.2,\ 0,\ 0)$. The experiment and the calculation are in reasonable agreement, although in the experiment the shoulder is more pronounced and at a higher energy than in the calculations. Moreover it looks the resolution of the lower energy peak is somewhat better than of the higher one. This could be the case if the corresponding slopes of the dispersion of the two measured phonons are different. The Gaussian fits were not only used to determine the phonon energy but also the phonon linewidth. Figure 3.23 shows the comparison of those two quantities for both wave vectors $\mathbf{Q} = (1.5,\ 1.5,\ 1.5)$ and $\mathbf{Q} = (1.6,\ 1.6,\ 1.6)$ displayed above. The temperature dependence of the phonon energy (i.e. the peak position) is quite different for the two wave vectors. For $\mathbf{Q} = (1.6,\ 1.6,\ 1.6)$ (red squares) a slight and continuous decrease of the phonon energy of a few percent can be observed on heating from base temperature to room temperature as it was expected (see Chapter 3.2.1). A typical temperature behavior of a phonon is that the phonon energy slightly decreases and the linewidth moderately increases on heating [Fig. 3.23(D)]. While the experimental data at $\mathbf{Q} = (1.5,\ 1.5,\ 1.5)$ (black circles) reveal an anomalous softening of the phonon energy on heating to $T = 200\,\mathrm{K}$ of over $20\,\%$ and a normal behavior on further heating to $T = 300\,\mathrm{K}$. At $T = 200\,\mathrm{K}$ for this particular phonon the calculations predict a softening of around $5\,\%$ [Fig. 3.23(d)]. Another difference in the temperature dependence of those two wave vectors can be seen in the behavior of the phonon linewidth. The linewidth of $\mathbf{Q} = (1.6,\ 1.6,\ 1.6)$ (red squares) slightly increases within the error bar on heating as expected. The experimental data were fitted using only free fits without restrictions. All parameters including the intensity evolved constantly and the shoulder of the main peak mentioned above was not a problem. The linewidth of $\mathbf{Q} = (1.5,\ 1.5,\ 1.5)$ (black circles) also increases but not as continuous as at the other wave vector. Here a jump occurs on heating just below $T = 100\,\mathrm{K}$ in an otherwise linear temperature evolution. Before and after the anomaly the slope is comparable to that of $\mathbf{Q} = (1.6,\ 1.6,\ 1.6)$.

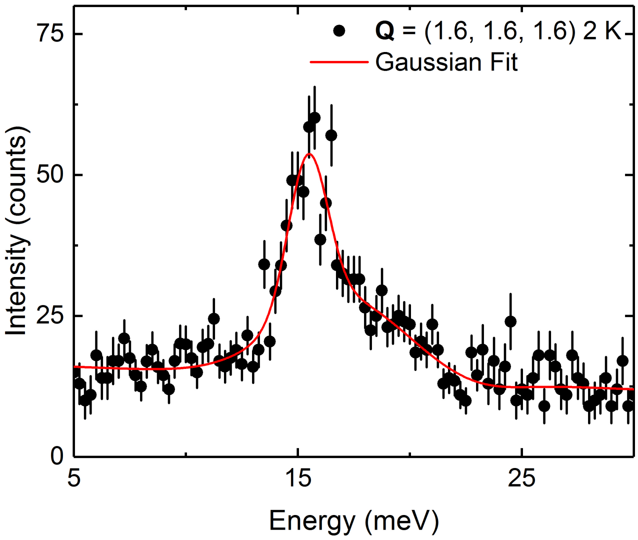

(a) Experimental data

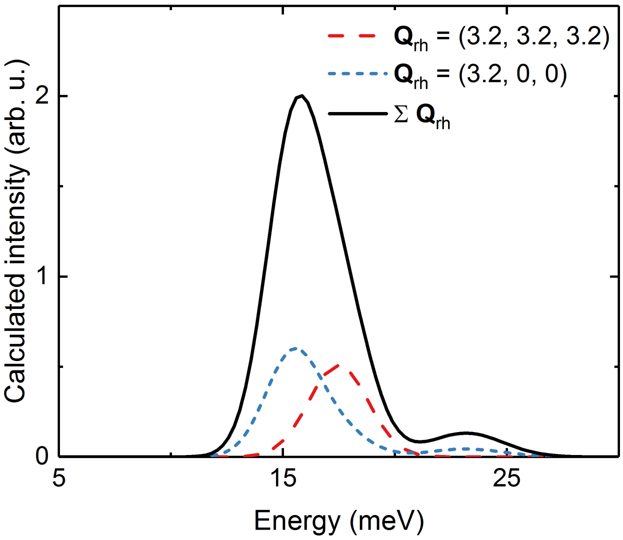

(b) Theoretical calculations

Figure 3.22: (a) Experimental data (black circles) and (b) the calculated structure factor for the wave vector $\mathbf{Q} = (1.6, 1.6, 1.6)$. The experimental data was taken at 2.3 K fitted with two Gaussian peaks (red line) analogous to the peaks in the lattice dynamical calculations. The calculations were carried out for all four twins $\mathbf{Q} = (3.2, 3.2, 3.2)$, $\mathbf{Q} = (3.2, 0, 0)$, $\mathbf{Q} = (0, 3.2, 0)$, $\mathbf{Q} = (0, 0, -3.2)$. Since the results for the latter three are identical the sum for all twins (black line) is the combination of $\mathbf{Q} = (3.2, 3.2, 3.2)$ (red dashed line) and three times $\mathbf{Q} = (3.2, 0, 0)$ (blue dashed line).

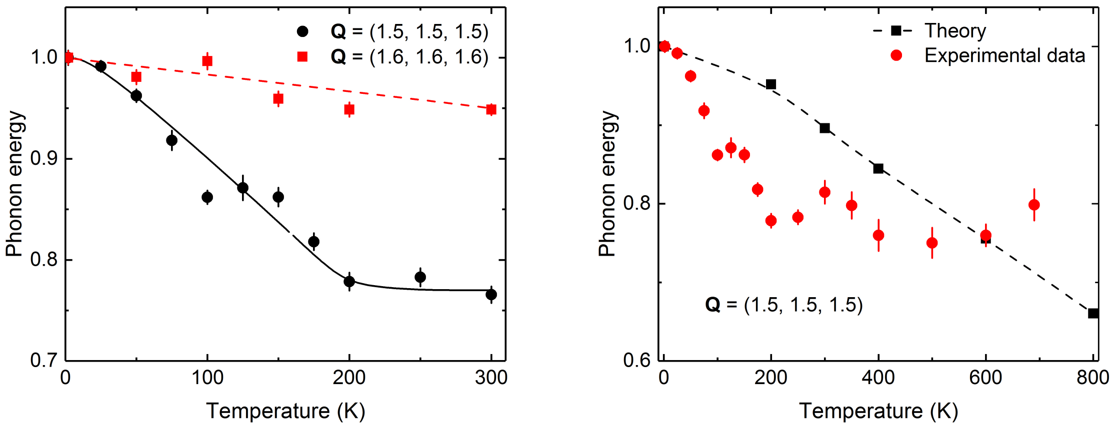

(a) Normalized phonon energy

(b) Phonon energy of **Q** = (1.5, 1.5, 1.5), theory and experiment

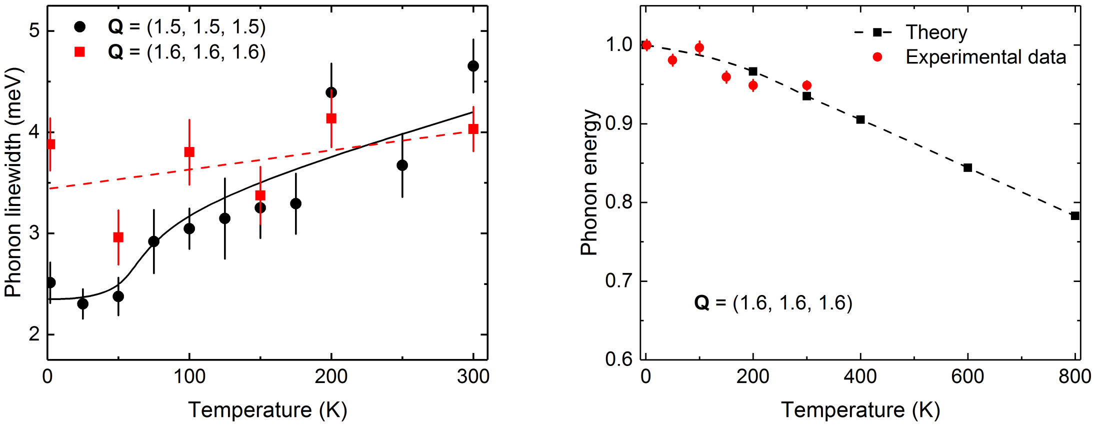

(c) Phonon linewidth

(d) Phonon energy of **Q** = (1.6, 1.6, 1.6), theory and experiment

Figure 3.23: (a) Phonon energy normalized to the low temperature values for the wave vectors **Q** = (1.5, 1.5, 1.5) (black circles) and **Q** = (1.6, 1.6, 1.6) (red squares). The lines are a guide to the eye. (c) Temperature dependence of the phonon linewidth for the wave vectors **Q** = (1.5, 1.5, 1.5) (black circles) and **Q** = (1.6, 1.6, 1.6) (red squares). The lines are a guide to the eye. (b) and (d) Comparison of the calculated (quasi harmonic approximation) and experimental temperature dependence of the phonon energies of two phonons at **Q** = (1.5, 1.5, 1.5) and **Q** = (1.6, 1.6, 1.6). The lines are a guide to the eye. (b) Shows also experimental data for higher temperatures which will be presented next.

The phonon at $E_{\mathrm{ph}} = 11.85\,\mathrm{meV}$ at 2.3 K for $\mathbf{Q} = (1.5, 1.5, 1.5)$ exhibits an anomalous behavior and seems to be sensitive to the first crossover at $T_{\mathrm{SS}} \approx 100\,\mathrm{K}$. Therefore it was essential to follow the temperature evolution to above the second crossover at $T_{\mathrm{MI}} \approx 500\,\mathrm{K}$. Since this was not possible with the small cryostat used for the low temperature measurements a larger cryostat designed for higher temperatures was used. The problem there was that the background much higher [Fig. 3.24(a)]. The signal to background ratio was much higher for the previous measurements and a linear function could be used to perfectly describe the background. To fit the background for $T > 300\,\mathrm{K}$ an exponential function was used. After subtracting the fitted curve from the experimental data [Fig. 3.24(b)] the peak intensity is still pretty low but the peak position (i.e. phonon energy) can be determined reliably by a Gaussian fit. The observed phonon softening on heating from base temperature to room temperature is already clearly visible in the raw data [Fig. 3.25(b)]. Moreover a further softening can be observed on heating to $T = 600\,\mathrm{K}$. Additionally the data show circumstantial evidence that the phonon linewidth decreases on heating to high temperatures after the reported increase on heating to $T = 300\,\mathrm{K}$ [Fig. 3.23(c)]. A detailed analysis of the linewidth for $T > 300\,\mathrm{K}$ was not possible because of the high experimental background with the large cryostat and the resulting large error bars. However the temperature dependence of the phonon energy could be determined very well and is pictured in Figure 3.25(b). As already shown in Figure 3.23(a) the 11.85 meV phonon exhibits a strong softening on heating to $T = 200\,\mathrm{K}$. On further heating the phonon energy indicates a local maximum just above $T \approx 300\,\mathrm{K}$. Above the temperature of the second crossover $T_{\mathrm{MI}} \approx 500\,\mathrm{K}$ the data suggests a slight hardening. Apart from the above presented measurements of phonons along [1 1 1] with longitudinal symmetry, i.e. at $\mathbf{Q}$ with q parallel to tau, we also investigated other symmetries by selecting wave vectors with q not parallel to tau.

Figure 3.26 shows an energy scan at base temperature $T = 2\,\mathrm{K}$ (a) and the calculated phonon intensity (c) for the wave vector $\mathbf{Q} = (2.5, 1.5, 0)$. The experimental data shows three clearly identifiable peaks at $E_{\mathrm{ph}} = 10.14\,\mathrm{mev}$, $17.34\,\mathrm{meV}$ and $24.25\,\mathrm{meV}$ that can be fitted with Gaussian peaks. The calculated phonon intensity on the other hand correctly expects three peaks at $E_{\mathrm{ph}} = 10.92\,\mathrm{meV}$ and two very close to each other around 21.52 meV and 25.55 meV. The one with the lowest and the the one with the highest energy fit quite well to the experimental data. The one in the middle is predicted to high by the lattice dynamical calculations compared with the experiment. The temperature dependence of both the phonon energy and the phonon linewidth exhibit the expected behavior for all three phonons (Fig. 3.26). The phonons soften by less than 10 % on heating from 2 K to 300 K with an linear decrease. Furthermore a normal phonon broadening with increasing temperature can be observed for all three phonons which also occurs continuously with a linear slope. The further away from high symmetry points in reciprocal space the measured wave vector is, generally the more phonons can be seen in these energy scans. Still, the main four phonon peaks

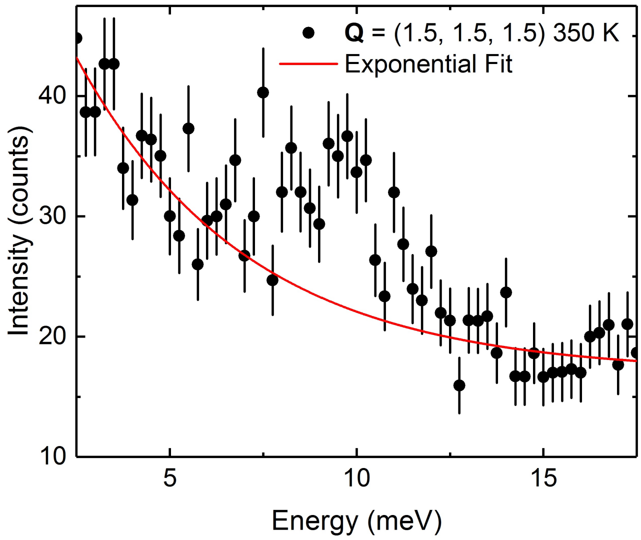

(a) Raw data

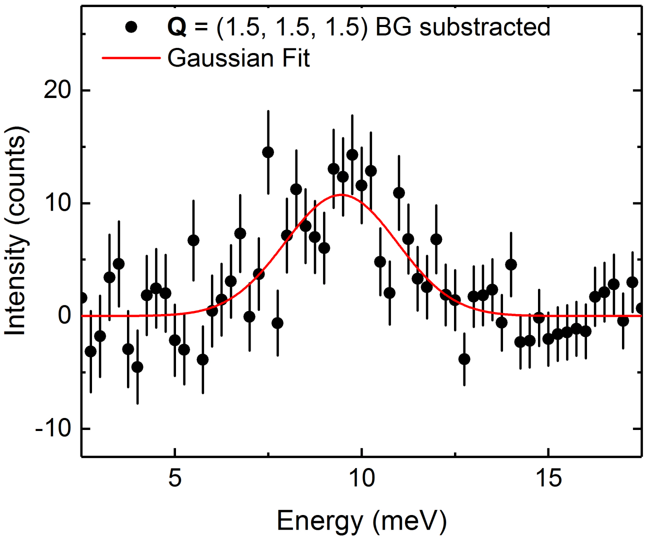

(b) Background corrected data

Figure 3.24: Inelastic neutron scattering data at 350 K at the wave vector $\mathbf{Q} = (1.5, 1.5, 1.5)$ (black circles). (a) Raw data and exponential fit for the background (red line) and (b) the background subtracted data.

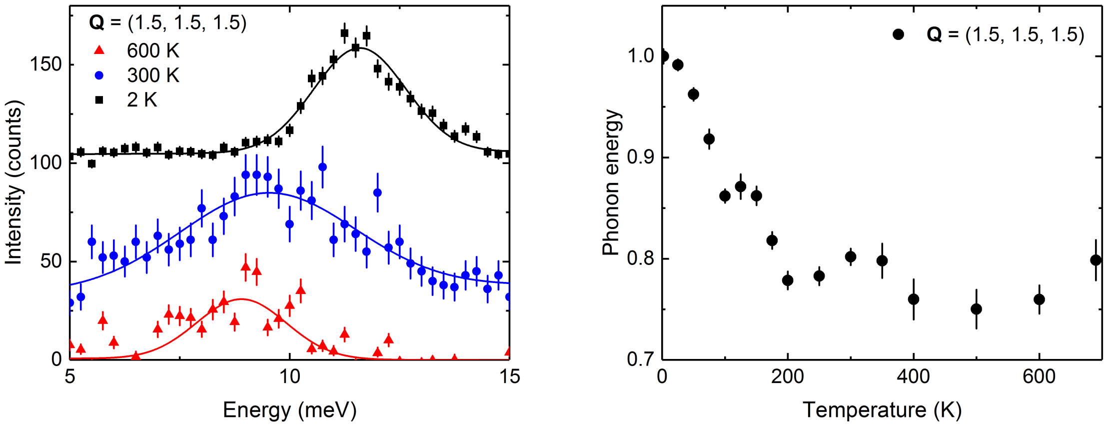

(a) Raw data

(b) Normalized phonon energy

Figure 3.25: (a) Background corrected inelastic neutron scattering data at the wave vector **Q** = (1.5, 1.5, 1.5) for three different temperatures: 2 K (black circles), 300 K (blue squares) and 600 K (red triangles). To get more comparable data the data points of the 2 K and 300 K scans were shifted up and the data points of the 600 K scan were multiplied by 3. (b) Phonon energy normalized to the low temperature value for the wave vector **Q** = (1.5, 1.5, 1.5).

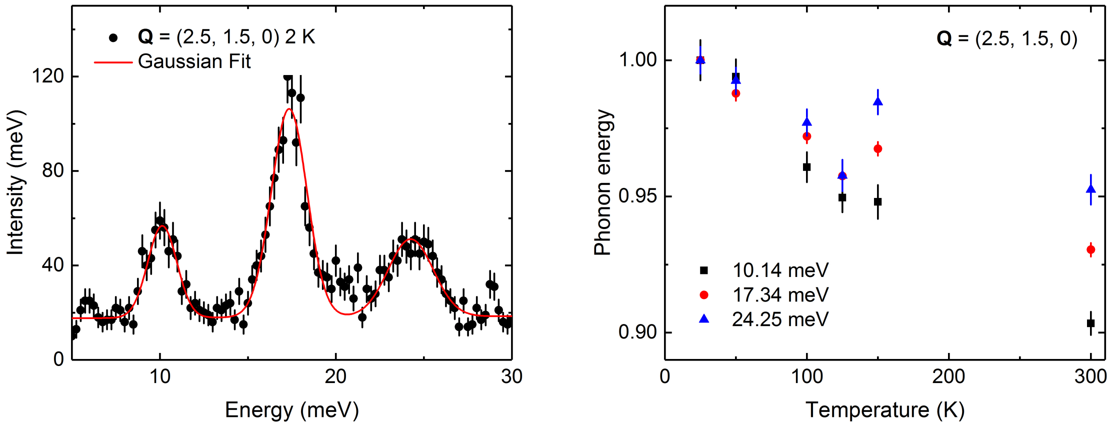

(a) Experimental data (b) Normalized phonon energy

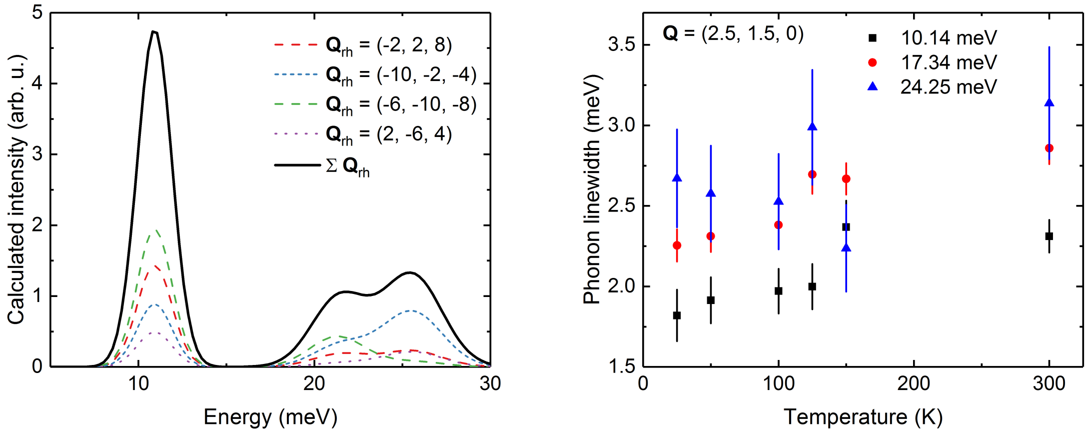

(c) Theoretical calculations (d) Phonon linewidth

Figure 3.26: (a) Experimental data (black circles) and (c) the calculated intensity for the wave vector $\mathbf{Q} = (2.5, 1.5, 0)$. The experimental data were taken at 2.3 K fitted with three Gaussian peaks (red line) analogous to the number of peaks in the lattice dynamical calculations. (b) Phonon energy normalized to the low temperature values for the wave vector $\mathbf{Q} = (2.5, 1.5, 0)$ (see legend for low T values of the phonon energies. (d) Temperature dependence of the phonon linewidth for the wave vector $\mathbf{Q} = (2.5, 1.5, 0)$. In both panels all three phonons at $E_{\mathrm{ph}} = 10.14\,\mathrm{mev}$ (black squares), 17.34 meV (red circles) and 24.25 meV (blue triangles) are shown.

at $E_{\mathrm{ph}} = 10.71\,\mathrm{meV}$, $15.09\,\mathrm{meV}$, $25.00\,\mathrm{meV}$ and $31.78\,\mathrm{meV}$ are well separated and can be analyzed for their temperature dependence. For the calculated intensity peaks can be found at $10.03\,\mathrm{meV}$, around $15.50\,\mathrm{meV}$, at $24.27\,\mathrm{meV}$ and around $33\,\mathrm{meV}$. Except for the third one even the relative intensities of the peaks are in accordance to the experimental data. One more peak can be seen in the lattice dynamical calculations which matches with some intensity in the energy scan around $20\,\mathrm{meV}$. The comparison between theoretical calculations and the experimental data underlines the remarkable quality of the theoretical predictions. Despite the rhombohedral twinning the calculations are able to explain the number of measurable phonons. Furthermore the energies and intensities are predicted correctly with just one exception for each. The four strong phonon peaks were fitted with Gaussian functions and evaluated in terms of the phonon energy and linewidth. The temperature dependence of both is shown in Figure 3.27. All phonons exhibit normal behavior. A small softening of about $3\,\%$ can be observed on heating from base temperature to about $T = 200\,\mathrm{K}$. Additionally a slight and continuous broadening on heating of all four phonons can be observed which is in accordance to a normal temperature dependence.

Figure 3.28 shows the experimental INS data (a) and the theoretical calculations (c) for the wave vector $\mathbf{Q} = (0,\,0,\,2)$. In both panels a clear peak can be observed. In the experimental data with a Gaussian fit the center of the phonon peak can be found at $E_{\mathrm{ph}} = 11.31\,\mathrm{meV}$ which is good agreement with $E_{\mathrm{ph}} = 10.92\,\mathrm{meV}$ resulting from the calculated intensity. For higher energies in the experiment and the calculations (around $20\,\mathrm{meV}$) two broad peaks with a lower peak intensity can be seen. Besides those three signals the experimental data exhibits a tail of the Bragg peak for low energies that is not featured in the lattice dynamical calculations. The temperature dependence of the phonon energy and the linewidth for $\mathbf{Q} = (0,\,0,\,2)$ (Fig. 3.28) behave very similar as for $\mathbf{Q} = (1.5,\,1.5,\,1.5)$ (black circles in Fig. 3.23). The phonon softens about $20\,\%$ upon heating from base temperature to $100\,\mathrm{K}$ and the phonon linewidth increases rapidly to about the double of the low temperature value. For higher temperatures the error bars get larger, especially for the linewidth, but within those the data suggest that the behavior of the phonon energy and linewidth both become linear and show a normal temperature dependence. The analysis of the high temperature measurements in the large cryostat could not be done due to the high background intensity. Particularly the data near and above the second crossover could not be used to get information about the behavior despite extended counting times for each measured energy.

The energy scans for the wave vector $\mathbf{Q} = (1.5,\,1.5,\,2.5)$ exhibit two strong and separated phonon peaks at $E_{\mathrm{ph}} = 11.71\,\mathrm{meV}$ and $21.52\,\mathrm{meV}$ [Fig. 3.29(a)] that can be fitted with Gaussians for a wide range of temperatures. However in the lattice dynamical calculations the peak around $21\,\mathrm{meV}$ consists of various phonon contributions and is broader than in the experiment with shoulders on both flanks that can only slightly be seen in the energy scan. The position of the lower energy peak $10.92\,\mathrm{meV}$ is in accordance to the experimental result.

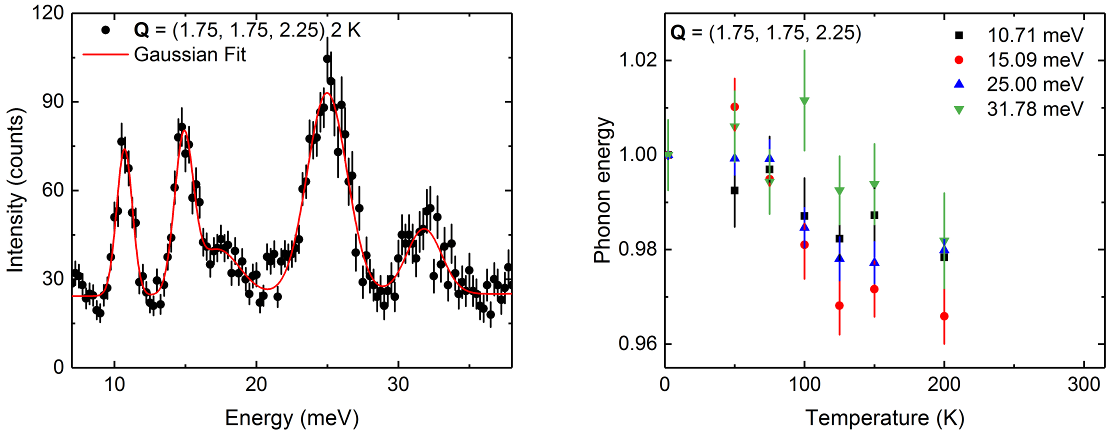

(a) Experimental data (b) Normalized phonon energy

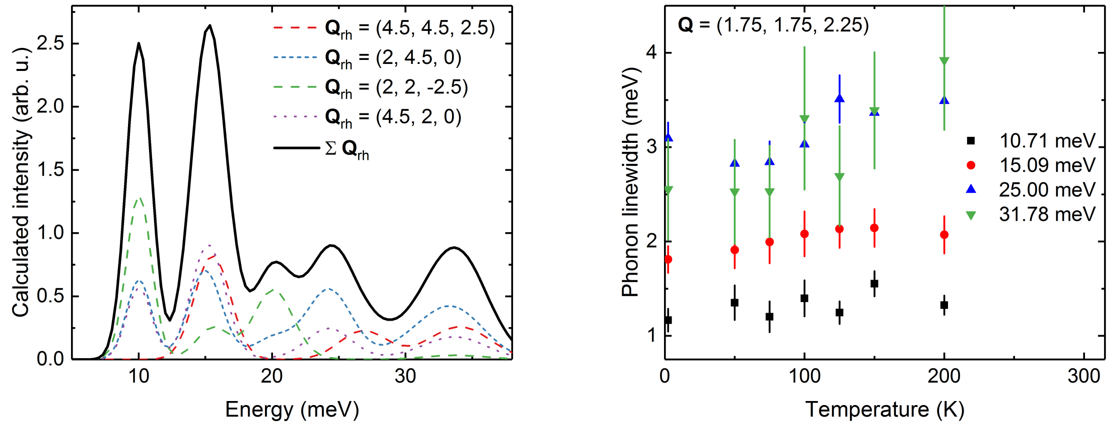

(c) Theoretical calculations (d) Phonon linewidth

Figure 3.27: (a) Experimental data (black circles) and (c) the calculated structure factor for the wave vector **Q** = (1.75, 1.75, 2.25). The experimental data was taken at 2.3 K fitted with five Gaussian peaks (red line) analogous to the peaks in the lattice dynamical calculations. (b) Phonon energies normalized to the respective low temperature values given in the legend for the wave vector **Q** = (1.75, 1.75, 2.25). (d) Temperature dependence of the phonon linewidths for the wave vector **Q** = (1.75, 1.75, 2.25).

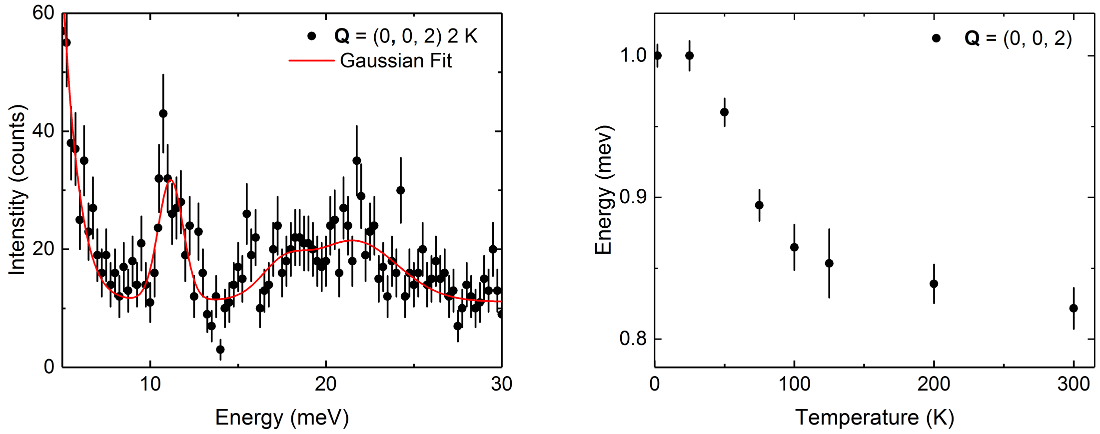

(a) Experimental data (b) Normalized phonon energy

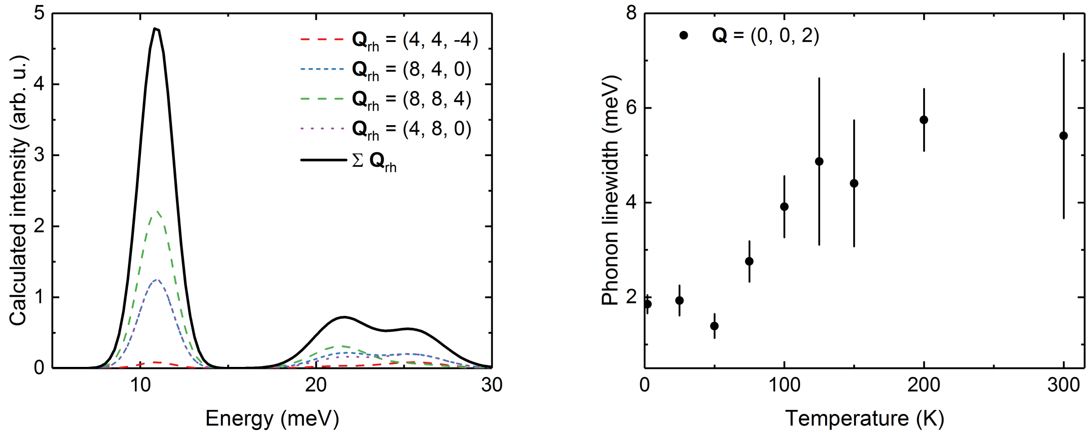

(c) Theoretical calculations (d) Phonon linewidth

Figure 3.28: (a) Experimental data (black circles) and (c) the calculated structure factor for the wave vector $\mathbf{Q} = (0,\ 0,\ 2)$. The experimental data was taken at 2.3 K fitted with three Gaussian peaks (red line) analogous to the peaks in the lattice dynamical calculations. (b) Phonon energy normalized to the low temperature values for the wave vector $\mathbf{Q} = (0,\ 0,\ 2)$. (d) Temperature dependence of the phonon linewidth for the wave vector $\mathbf{Q} = (0,\ 0,\ 2)$.

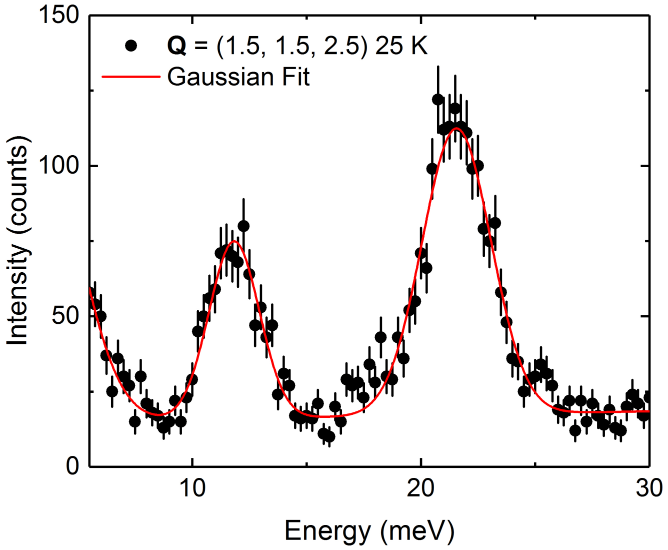

(a) Experiment data

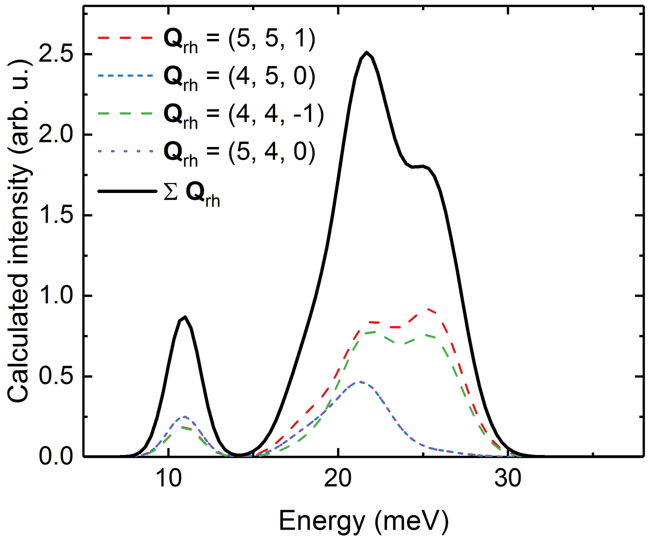

(b) Theoretical calculations

Figure 3.29: (a) Experimental data (black circles) and (b) the calculated structure factor for the wave vector **Q** = (1.5, 1.5, 2.5). The experimental data were taken at 25 K and fitted with two Gaussian peaks (red line). In the lattice dynamical calculations the peak at higher energies consists of several different phonon contributions and is therefore a lot broader with shoulders on both flanks.

Since both peaks can be fitted easily the temperature dependence of both the phonon energy and the linewidth can be determined very well which results in quite small error bars (Fig. 3.30). This gives the opportunity to study two phonons at the same wave vector for a wide temperature range from base to room temperature. The phonon with the higher energy at 21.52 meV shows a normal behavior in the temperature dependence of the energy with a small and linear softening and in the linewidth with a small and linear broadening. On the other hand the phonon at 11.71 meV exhibits anomalous behavior. In the range of the first crossover the phonon energy drops over 15 % from 25 to 100 K and for higher temperatures the energy is linear and nearly parallel to the line of the 21.52 meV phonon. The phonon linewidth of the lower energy phonon behaves very similar to that. It increases rapidly from 50 K to 70 K and jumps to a value about 50 % higher than its low temperature value. Above $T = 100\,\mathrm{K}$, the linewidth evolves linearly and is almost parallel to the second phonon.

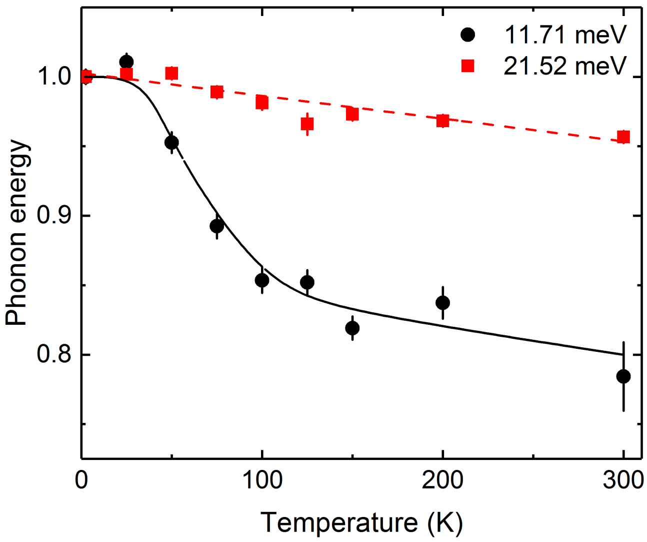

(a) Normalized phonon energy

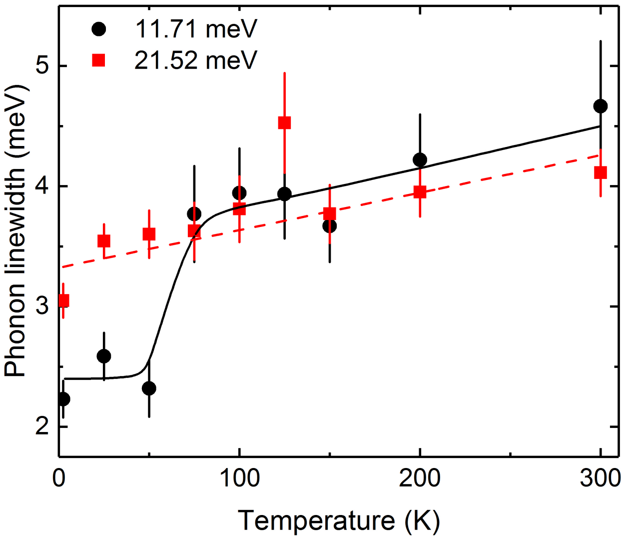

(b) Phonon linewidth

Figure 3.30: (a) Phonon energy normalized to the low temperature values for two phonons at 11.71 meV (black circles) and 21.52 meV (red squares) for $\mathbf{Q} = (1.5, 1.5, 2.5)$. The lines are a guide to the eye. (b) Temperature dependence of the phonon linewidth of the phonons at 11.71 meV (black circles) and 21.52 meV (red squares). The lines are a guide to the eye.

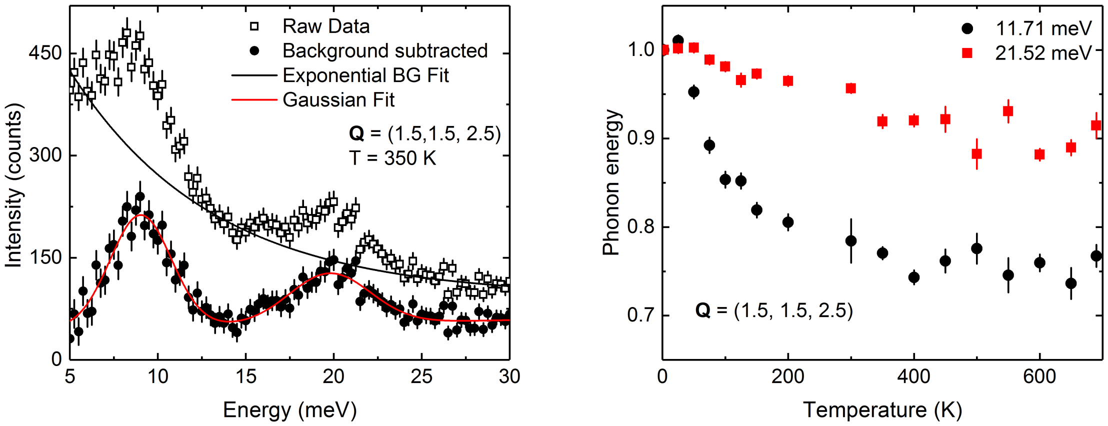

(a) Raw data and background corrected data

(b) Temperature dependence of the normalized phonon energy

Figure 3.31: (a) Energy scan at 350 K at the wave vector **Q**=(1.5, 1.5, 2.5). Raw data (open, black squares), data corrected by an exponential background (filled, black circles) and Gaussian fit (red line). (b) Temperature dependence of the normalized phonon energy for the two phonons at 11.71 meV (black circles) and 21.52 meV (red squares) at the wave vector **Q**=(1.5, 1.5, 2.5).

For $\mathbf{Q} = (1.5,\ 1.5,\ 2.5)$ high temperature measurements were performed using the larger cryostat. As already mentioned the background becomes stronger and can not be fitted by just a straight line. By fitting and subtracting an exponential background the determination of the phonon energy by using a Gaussian fit becomes possible. Figure 3.24(a) shows the raw data (open, black circles) were the fitting of the two phonon peaks would be challenging. The black circles are the background subtracted data were the two phonon peaks are detached and can be fitted easily with two Gaussian peaks. The temperature dependence of the phonon energy that can be determined from those scans is shown in figure 3.24(b). The normal softening of the higher energy phonon (red squares) shown in 3.30 continues on further heating above room temperature. In the vicinity of the second crossover $T_{\mathrm{MI}} \approx 500\,\mathrm{K}$ the measured values scatter stronger around a certain value but the data suggests that a linear fit is still a good model to describe the behavior of this phonon. The anomalously strong phonon softening on heating across the first crossover T_{SS} is followed by a nearly linearly decreasing behavior on further heating towards the second crossover. For both phonons the quasi harmonic approximation can be used to calculate a temperature dependence of the phonon energies. Figure 3.32 shows the comparison of those calculations (black squares) and the experimental data (red dots). The left panel shows the lower energy phonon that was measured at $E(T = 2\,\mathrm{K}) = 11.71\,\mathrm{meV}$. The already shown anomalous behavior can clearly be observed. The softening on heating across the first crossover to temperatures of about $\approx 150\,\mathrm{K}$ is more pronounced than the calculations predict. In an intermediate temperature region below $T \approx 400\,\mathrm{K}$ the smaller slope comparable to that of the calculations. On further heating the slope again becomes smaller and the calculated and experimental values of the phonon energy are in good agreement. The phonon with the higher energy $E(T = 2\,\mathrm{K}) = 21.52\,\mathrm{meV}$ in Figure 3.32(b) on the other hand shows the expected temperature dependence. Both the calculation and the experimental data show a slight softening on heating and are in really good agreement to each other.

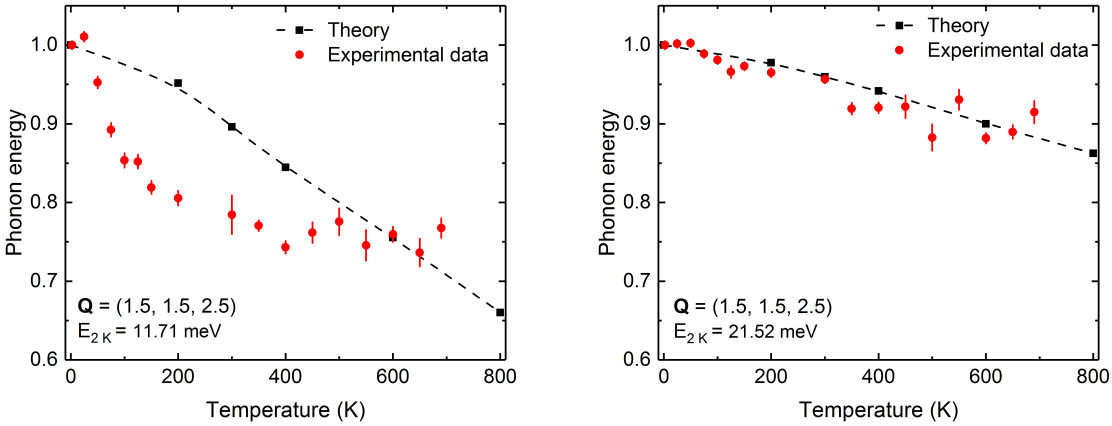

(a) $E(T = 2\,\mathrm{K}) = 11.71\,\mathrm{meV}$

(b) $E(T = 2\,\mathrm{K}) = 21.52\,\mathrm{meV}$

Figure 3.32: Comparison of the calculated (black squares) and experimental (red dots) temperature dependence of the phonon energies at the wave vector **Q**=(1.5, 1.5, 2.5). All energies are normalized to the low temperature values. The lines are a guide to the eye. (a) lower energy phonon with the experimental low temperature phonon energy of $E(T = 2\,\mathrm{K}) = 11.71\,\mathrm{meV}$. (b) higher energy phonon with the experimental low temperature phonon energy of $E(T = 2\,\mathrm{K}) = 21.52\,\mathrm{meV}$

High energy phonon measurements at PUMA

Additionally to the acoustic low energy measurements performed at 1T at the LLB, high energy phonon modes were studied at the triple axis spectrometer PUMA at the MLZ. With its higher flux PUMA is more suitable for the measurement of high energy phonon modes with typically lower neutron counting rates. The layout of the instrument has the same main components as 1T does (see 2.1). The idea to examine the high energy phonons as well is that some of those are associated with the breathing mode we are looking for. The wave vectors $\mathbf{Q} = (2.5, 2.5, 2.5)$, $\mathbf{Q} = (1.5, 1.5, 2.5)$ and $\mathbf{Q} = (2, 2, 2)$ were measured. For the latter two a temperature dependence could not be determined since there were to many peaks in one scan that were moving into each other so that neither the energy and especially the linewidth could not be fitted properly.
For $\mathbf{Q} = (2.5, 2.5, 2.5)$ the raw data of an INS energy scan at 20 K is shown in Figure 3.33(a). In the displayed energy range two clearly separated phonon peaks at 68.26 meV and 82.60 meV can be observed. The calculated intensity also shows two maxima at 67.96 meV and 79.05 . The one at lower energy perfectly fits to the experimental data and the other is estimated lie at a slightly smaller energy. With increasing temperature it becomes obvious that the peak at 82.60 meV in the experimental data consists of two different phonons whose energy shift independently with temperature [Fig. 3.34(a)] which can also be seen in the lattice dynamical calculations.

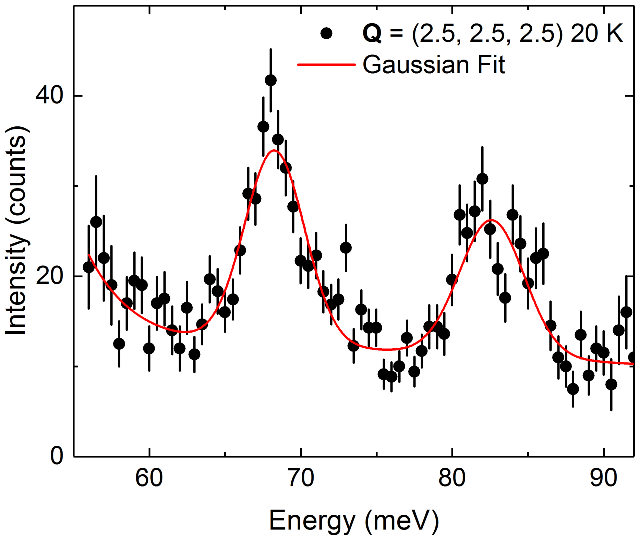

(a) Experimental data

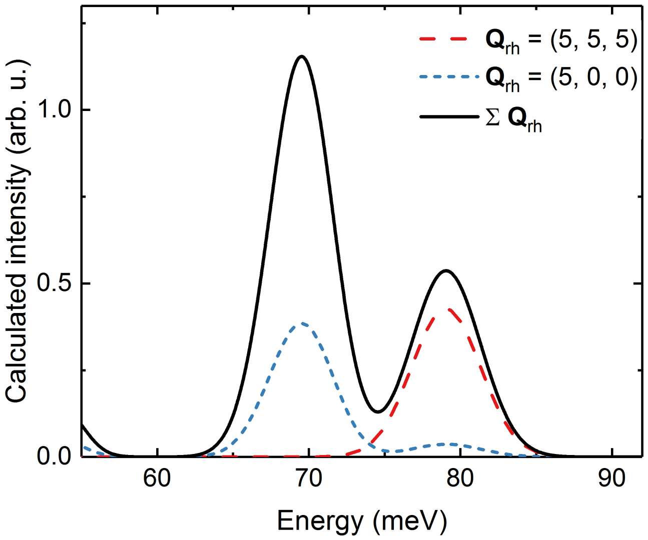

(b) Theoretical calculations

Figure 3.33: (a) Experimental data (black circles) and (b) the calculated structure factor for the wave vector **Q** = (2.5, 2.5, 2.5). The experimental data was taken at 20 K fitted with three Gaussian peaks (red line) analogous to the peaks in the lattice dynamical calculations.

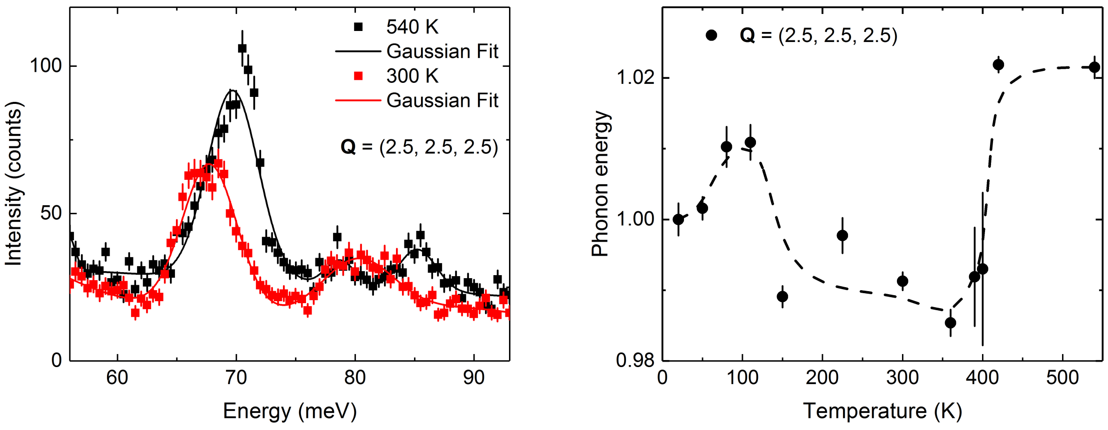

(a) **Q**=(2.5, 2.5, 2.5) (b) **Q**=(2.5, 2.5, 2.5)

Figure 3.34: (a) Inelastic neutron scattering data at the wave vector **Q** = (2.5, 2.5, 2.5) for two different temperatures: 540 K (black circles) and 300 K (red squares). (b) Temperature dependence of the phonon energy of the 68.24 meV phonon for **Q** = (2.5, 2.5, 2.5). The dashed line is a guide to the eye.

Figure 3.34(a) shows the raw data of two different energy scans at 300 K and 540 K for **Q** = (2.5, 2.5, 2.5). It exhibits a clear hardening on heating above the second crossover at $T_{\mathrm{MI}} \approx 500\,\mathrm{K}$ of the lower energy phonon. It was not possible to determine the phonon energy of the other two phonons since in certain scans they cannot be separated from each other as already shown. The full temperature dependence of the 68.26 meV phonon for the whole temperature range is shown in 3.34(b). On heating towards the first crossover at $T_{\mathrm{SS}} \approx 100\,\mathrm{K}$ a phonon hardening can be observed, directly followed by an abrupt softening and more or less linear region from $150\,\mathrm{K} < T < 360\,\mathrm{K}$ where only a slight softening can be seen. Clearly below ($T \approx 400\,\mathrm{K}$) the second crossover the phonon energy increases about 3 % within less than 20 K. For higher temperatures the phonon energy exhibits no further changes. In Figure 3.35 the experimental (red dots) temperature dependence of the 68.26 meV phonon (low T value) for **Q** = (2.5, 2.5, 2.5) is shown together with the calculated (black squares) temperature dependence of the phonon. Both are normalized to the corresponding low temperature value. The calculation yields the behavior for a usual temperature dependence, it exhibits a continuous softening. The experimental data shows an abrupt softening on heating across the first crossover and a stronger hardening on heating to above the second crossover within a few Kelvin. In the intermediate temperature regime $200\,\mathrm{K} < T < 400\,\mathrm{K}$ the experimental phonon energy exhibits a slight and continuous softening with a slope comparable to the calculated behavior. As already mentioned

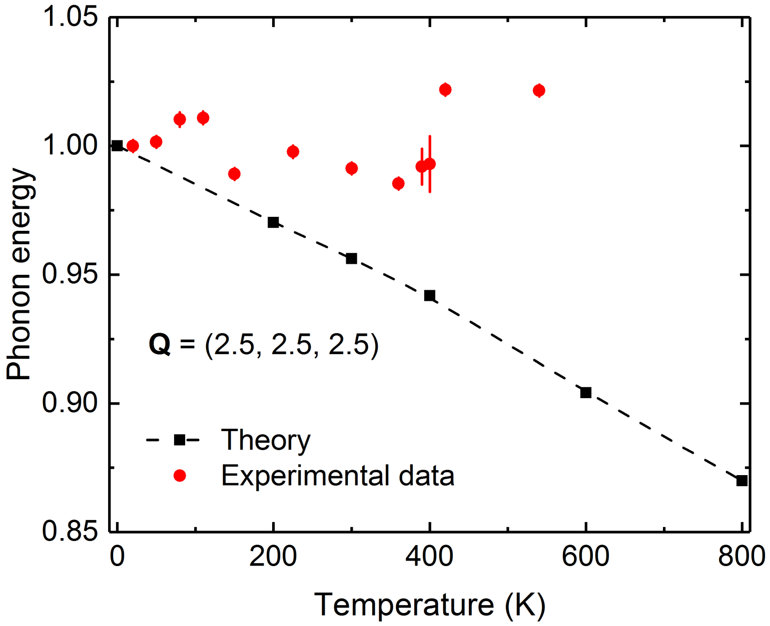

Figure 3.35: Comparison of the calculated (black squares) and experimental (red dots) temperature dependence of the phonon energies at the wave vector **Q**=(2.5, 2.5, 2.5). All energies are normalized to the low temperature values. The lines are a guide to the eye. The experimental phonon energy at the lowest temperature ($T = 20\,\mathrm{K}$) is $E(T = 20\,\mathrm{K}) = 68.24\,\mathrm{meV}$

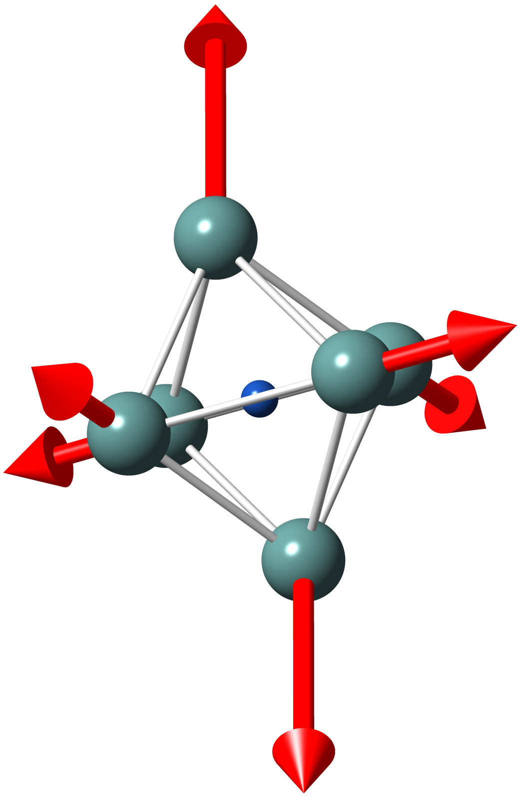

Figure 3.36: Displacement pattern of the 68.26 meV phonon for $\mathbf{Q} = (2.5, 2.5, 2.5)$ from lattice dynamical calculations (red arrows). Shown is the CoO_6 octahedron. The Co atom is displayed in blue and the surrounding O atoms are turquoise.

some of the high energy phonon modes can be associated with the expected breathing mode. The calculations can also be used to determine the displacement patterns of specific phonon modes. If the displacement pattern for the 68.26 meV phonon (low T value) for $\mathbf{Q} = (2.5, 2.5, 2.5)$ is calculated it gets obvious that the movement is dominated by the light oxygen atoms and the heavier lanthanum and cobalt atoms are slightly moving. Figure 3.36 shows the directions in which the oxygen atoms of this phonon mode are moving. All six atoms on the corners of the octahedron are moving away from the central cobalt ion. The volume of the octahedron increases in this processes. This is very similar to the ideal breathing mode that was expected. Hence this phonon is of special interest in two ways. It exhibits both the displacement pattern we were looking for and has the ordering vector $\mathbf{q} = (0.5, 0.5, 0.5)$ we were focusing on.

3.3 Discussion and outlook

3.3.1 Diffraction

The MSD measured on HEiDi clearly showed an anomaly at $T = 360\,\mathrm{K}$ for all three types of atoms. A local maximum that differs from the otherwise exponential behavior can be seen.

Compared to the powder diffraction study of Radaelli *et al.* [51] our measurements show slightly different values of the lattice constants for the temperature of the observed anomaly. In particular, the nonmonotonic temperature dependence of the La-O bond length in $LaCoO_3$ observed by Radaelli *et al.*(Fig. 3.19) could not be resolved. The question emerges if something was not done correctly during the experiments or the data analysis.

Radaelli *et al.* [51] also examined the oxygen MSD (Fig. 3.37). There the high-temperature upturn can also be seen but the anomaly can not be observed.

The measurement at the temperature of the anomaly was checked twice and it showed only small error bars and deviations in the refinement. No obvious mistakes (experimental nor concerning the data analysis) could be found. The only option to answer the question whether the measured anomaly in the MSD is real or not is perform further measurements in the questionable temperature range. This could either be done with neutron or x-ray diffraction.

Although the second crossover takes place at $T_{\mathrm{MI}} \approx 500\,\mathrm{K}$, in other studies anomalies at $T \approx 360\,\mathrm{K}$, i.e., the same temperature where the anomaly in the MSD is observed, were reported. Señarís *et. al* [72] studied the magnetic and transport properties of single phase $LaCoO_3$ (see Chapter 3.1.3). They reported different temperature domains due to the population of the different spin states and proposed a change of domains at around $T \approx 350\,\mathrm{K}$ which fits very well to the temperature region our anomaly takes place. In one of our own measurements we also do see a change of behavior in this temperature region. In the INS data for the high energy phonons at PUMA (see Fig. 3.34) a strong increase of the phonon energy can be seen slightly above $T \approx 360\,\mathrm{K}$. Within just a few Kelvin the phonon energy hardens by more than 2.5 meV and stays constant on further heating even when passing the temperature of the second crossover at $T_{\mathrm{MI}} \approx 500\,\mathrm{K}$. These are hints that the feature in our data is real.

The only way to shine light on the question of the anomaly in the MSD at $T = 360\,\mathrm{K}$ is to take more data points in the vicinity of the anomaly. X-ray and neutron diffraction measurements are planned to answer the open questions.

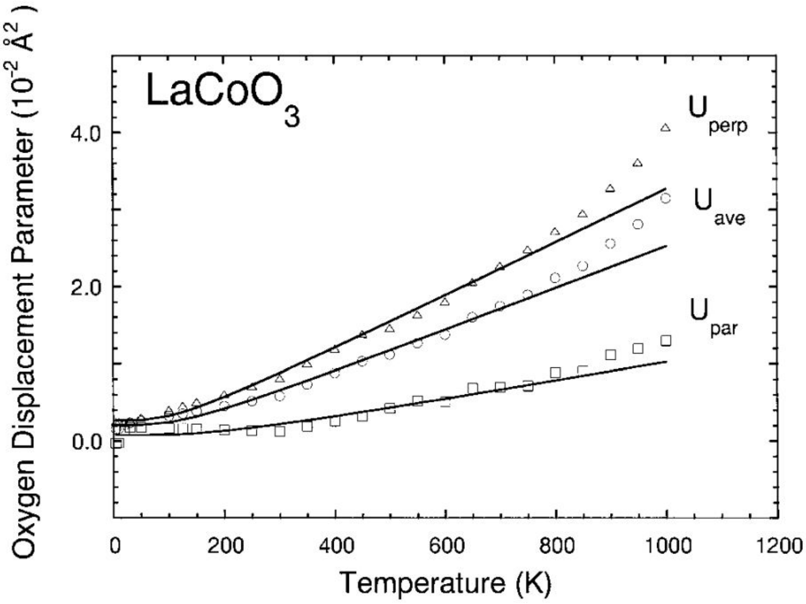

Figure 3.37: Oxygen displacement parameters in $LaCoO_3$. Average value (circles) and projections of the oxygen displacement parameters parallel (squares) and perpendicular (triangles) to the Co-O bond. The solid lines are fit to the data up to $T = 800\,K$, using a simple Einstein oscillator. The Einstein temperatures were 297, 500, and 334 K, respectively. Clearly visible is a high-temperature upturn, probably due to additional disorder from oxygen vacancies. [51]

3.3.2 Inelastic neutron scattering

A number of inelastic neutron scattering measurements had been performed prior to to this thesis. We made considerable progress compared to the previous studies. The measurements for this thesis were done with a better resolution. More importantly we were the first to compare the experimental results with lattice dynamical calculations that take the rhombohedral distortion into account. In Chapter 3.2.1 it was shown that is essential to include the actual rhombohedral structure and the twinning in the lattice dynamical calculations.

Our measurements are in good agreement to the existing INS measurements. Figure 3.38(a) shows the temperature dependent energy of two optical phonon modes measured at $\mathbf{Q} = (2.5, 1.5, 1.5)$ with inelastic neutron scattering in comparison to a Raman study [note that this wave vector corresponds to the Bragg reflection $(-2, 2, 8)$ of the rhombohedral structure]. Both show a similar temperature dependence of both the phonons at this wave vector compared to the corresponding wave vector in our measurements [Fig. 3.38(b)]. The phonon slightly above 20 meV exhibits a slight softening on heating (3 % on heating from 5 K to room temperature) which is considered as usual behavior as underlined by our lattice dynamical calculations. Furthermore the phonon around 11 meV shows the same anomalous strong softening on heating (20 % on heating to room temperature) to temperatures above the first crossover.

Furthermore, our study covered a larger temperature range, $5\,\mathrm{K} \leq T \leq 700\,\mathrm{K}$, i.e., from well below the first crossover to well above the second one. Temperature dependencies were determinded for a number of wave vectors of phonons with usual or anomalous behavior. Theoretically, the temperature dependencies of phonon mode energies were calculated from *ab-initio* lattice dynamical calculations using the quasi-harmonic approximation. The comparison of experiment and theory revealed two situations: (1) For phonons with a usual behavior the calculated temperature dependence is in accordance with the experiment. (2) Some phonons exhibit pronounced softening in certain temperature ranges which strongly deviates from the predicted quasi-harmonic temperature dependence. They show a significantly larger softening but for higher temperatures $T > T_{\mathrm{MI}} \approx 500\,\mathrm{K}$ experiment and theory are very similar again. This behavior is most profound for wave vectors that are in accordance with the proposed ordering vector $\mathbf{q} = (0.5, 0.5, 0.5)$ of the dynamic short-range order. For the wave vectors $\mathbf{Q} = (1.5, 1.5, 1.5)$ ($E_{2\,\mathrm{K}} = 11.85\,\mathrm{meV}$ see Fig. 3.25) and $\mathbf{Q} = (1.5, 1.5, 2.5)$ ($E_{2\,\mathrm{K}} = 11.71\,\mathrm{meV}$, see Fig. 3.32) we identify the anomalous softening as the difference between the calculated phonon energies and the observed ones and plot this difference as an absolute value in Figure 3.39(red symbols).

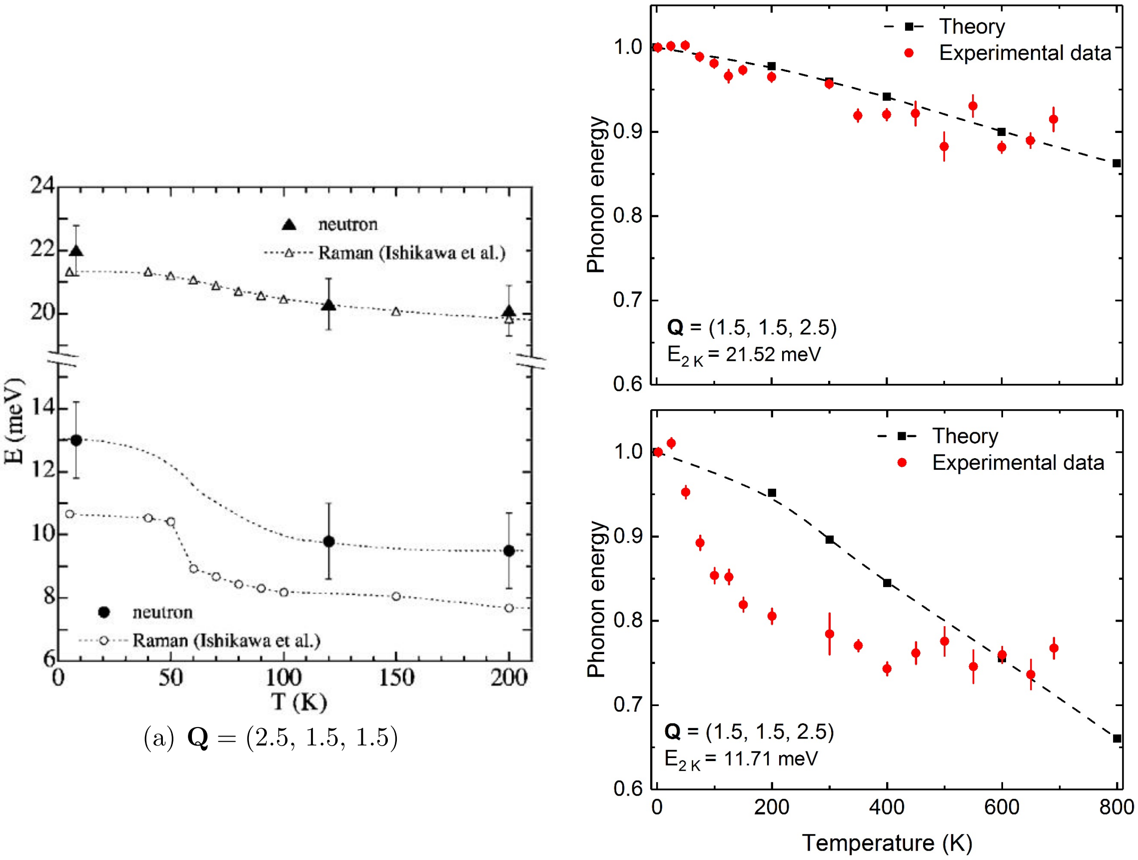

(a) $\mathbf{Q} = (2.5,\ 1.5,\ 1.5)$

(b) $\mathbf{Q} = (1.5,\ 1.5,\ 2.5)$

Figure 3.38: (a) Temperature dependence of the phonon energy at $\mathbf{Q} = (2.5,\ 1.5,\ 1.5)$ from INS (closed symbols). The Raman data (open symbols) are from Ishikawa *et al.* [78]. The circles show the lower energy phonon and the triangles the one with a higher energy. The dashed lines are guides to the eye. [74] (b) Temperature dependence of the phonon energy at $\mathbf{Q} = (1.5,\ 1.5,\ 2.5)$ from our INS study (red dots) and the lattice dynamical calculations (black squares). The lower panel shows the lower energy phonon (11.71 meV at base temperature) which shows a strong and anomalous softening on heating. The higher energy phonon (21.52 meV, upper panel) exhibits a slight softening on heating which is considered as a normal temperature dependence.

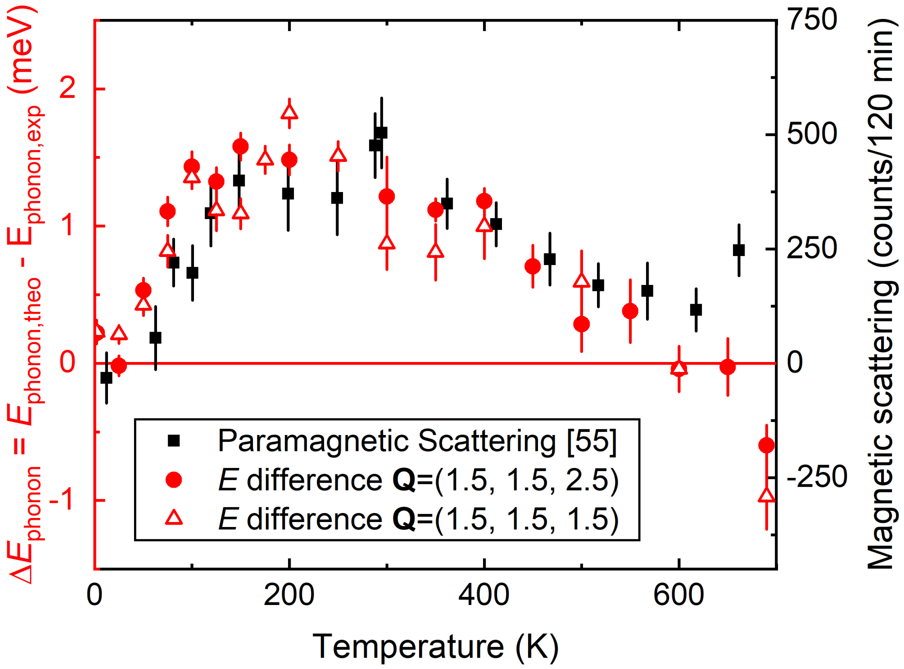

Figure 3.39: Difference in the phonon energy between the lattice dynamical calculations and the experimental data for $\mathbf{Q} = (1.5, 1.5, 1.5)$ ($E_{2\,\mathrm{K}} = 11.85\,\mathrm{meV}$ see Fig. 3.25, red open triangles) and $\mathbf{q} = (1.5, 1.5, 2.5)$ ($E_{2\,\mathrm{K}} = 11.71\,\mathrm{meV}$, see Fig. 3.32, red closed circles). The resulting data points represent the purely anomalous behavior since the calculations predict the normal temperature dependence. The black squares are the paramagnetic scattering at $\mathbf{Q} = (1.07, 0, 0)$ measured by Asai *et al.* [56].

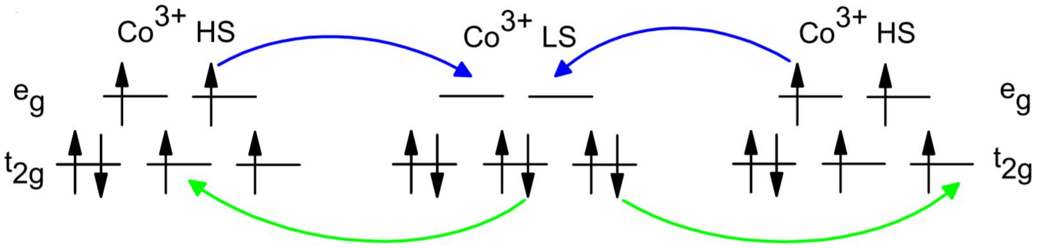

Figure 3.40: Superexchange in $LaCoO_3$. For strained $LaCoO_3$ correlated t_{2g} and e_g hopping processes between Co^{3+}(LS) and Co^{3+}(HS) neighbors lead to a ferromagnetic superexchange. Due to the correlated hopping of t_{2g} and e_g electrons, spin states are interchanged without a net transfer of charge. In the sketch,only the local t_{2g} and e_g hopping processes for the transformation of a Co^{3+}(LS) into a Co^{3+}(HS) ion are considered. [79]

For both phonons a very similar behavior can be observed. The difference in the phonon energy of the theoretical calculations and the experimental data, due to normalization, start at zero and strongly increase on heating to above the first crossover at $T_{\mathrm{SS}} \approx 100\,\mathrm{K}$. In the intermediate temperature range between the two crossovers the difference just slightly decreases and is nearly constant. On further heating ($T > 400\,\mathrm{K}$) a stronger decrease can be seen. After passing the second crossover at $T_{\mathrm{MI}} \approx 500\,\mathrm{K}$ the difference is almost zero again. The shape of both data sets is very similar to the paramagnetic cross section at $\mathbf{Q} = (1.07,\ 0\,, 0)$ measured by Asai *et al.* [56] shown in Figure 3.10. Near a Bragg peak the paramagnetic cross section has a more paramagnetic-ferromagnetic character a strong correlation to the population of HS states is assumed.

In epitaxially strained $LaCoO_3$ thin films [80] and at the surface of a $LaCoO_3$ single crystal [81] a ferromagnetic order was found. Merz *et al.* [79] studied this order in more detail with x-ray absorption and magnetic circular dichroism. They reported that the ferromagnetism in epitaxial $LaCoO_3$ arises from a superexchange between Co^{3+} high-spin and Co^{3+} low-spin ions where the spin and orbital moments of t_{2g} electrons fluctuate on Co^{3+}(HS)-O-Co^{3+}(LS) bonds (Fig. 3.40). Therefore, it is essential that HS and LS states are alternating. If this order is broken, the ferromagnetism vanishes. This rationalises the proposed dynamic LS/HS order and the results for $LaCoO_3$. The different spin states are arranged in a fluctuating checkerboard pattern until the order is melting in the temperature region of the second crossover. The decreasing paramagnetic scattering (Fig. 3.39) and the sample susceptibility (see Fig. 3.3) support this scenario. Moreover this is further evidence that the proposed short-range dynamic order becomes visible in the anomalous softening in this temperature range.

The temperature evolution of certain phonon energies seems to be correlated with the magnetic/spin properties of the Co ions. In order to study the influence of magnetism on the phonon energies, calculations with spin-polarization for a ferromagnetic state were performed. In general, the whole phonon spectrum is softened. For the particular case of the phonon observed at $E(T = 2\,\mathrm{K}) = 11.85\,\mathrm{meV}$ for $\mathbf{Q} = (1.5,\ 1.5,\ 1.5)$, the observed and calculated temperature dependencies are displayed in Figure 3.41. The HS state is represented by the spin-polarized calculation which is about 25 % softer than the LS state calculation without spin-polarization. The experimental data was scaled to the calculation without spin-polarization at low temperatures since the ground state of $LaCoO_3$ is purely LS. The behavior on heating is in good agreement with the theoretical models described in Chapter 3.1.2: More and more HS states are populated on heating across the first crossover, the experimental data softens towards the predicted phonon energies of the spin-polarized calculations. In an intermediate temperature range an dynamical order of LS/HS is stabilized, less HS states are newly populated and the temperature dependence of the experimental phonon energy is more or less parallel to the calculations and behaves normally in this temperature range. On further heating towards the second crossover the order of the LS/HS states arranged in a dynamic checkerboard pattern starts melting. In agreement to the discussion above the paramagnetic-ferromagnetic scattering cross section decreases. The experimental phonon energy now is in good agreement again with the calculations without spin-polarization.

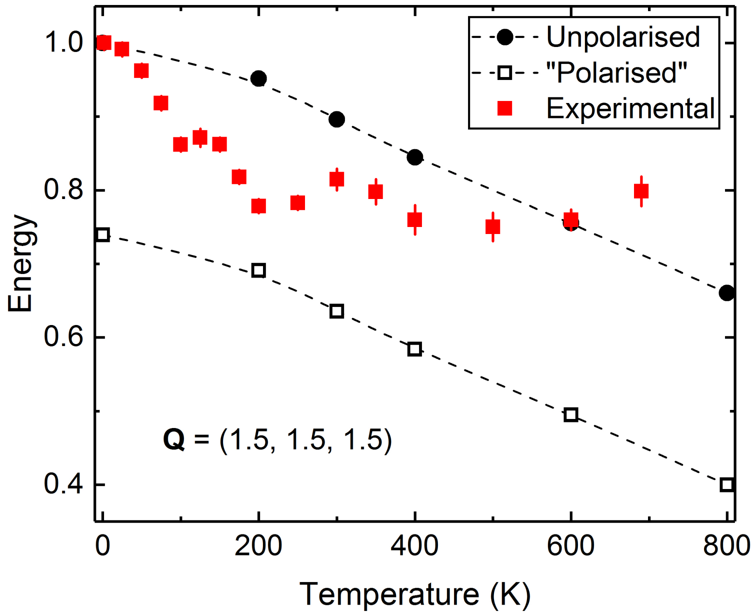

Figure 3.41: LS and HS state phonon energy simulated by calculations for **Q** = (1.5, 1.5, 1.5). The red squares are the experimental data, the black circles are the unpolarized calculation data and the black open squares polarized. The polarized calculations assume the Co ions to be magnetic trying to recreate the HS state in the calculations and the unpolarized calculations representing the LS state. The temperature dependence of the unpolarized data was accomplished by using a quasi harmonic approximation with experimental lattice parameters in the underlying crystal structure. The temperature dependence of the polarized data was then directly scaled with the same factor. The lines are a guide to the eye.

Chapter 4

Iron-based superconductors

A new route to high-temperature superconductivity was discovered in 2008 by Kamihara *et al.* with the discovery of superconductivity at 26 K in LaFeAsO [82]. In the following years the family of iron-based superconductors has grown. With superconducting transition temperatures as large as 55 K [83] and high critical fields they offer a high potential for future applications [84, 85, 86]. These materials show rich phase diagrams (see Fig. 4.2) with several competing or cooperative phases which have been the driving force for fundamental research to understand the physical properties of these materials and get more information about the fundamental pairing mechanism causing high-temperature superconductivity [87, 88, 89].

One of the peculiarities of the Fe based superconductors is the emergence of a nematic phase. In such a phase there is already a preferred direction for, depending on the theoretical model, spin- or orbital fluctuation, however without long-range order of the same degrees of freedom [90]. In fact, this is similar to observations in liquid crystals where the term nematic has been coined [91]. Such a phase is found, e.g., in electron-doped $\mathrm{Ba(Fe_{1-x}Co_x)_2As_2}$ (Co-Ba122) on cooling: Before long-range magnetic order sets in, the tetragonal symmetry of the lattice is already reduced to orthorhombic at a higher nematic/structural transition temperature. It is widely believed that the nematic transition is driven by magnetic or orbital fluctuations, i.e., by the same degrees of freedom as the long-range magnetic or orbital order setting in at slightly lower temperatures. The role of the nematic phase and its fluctuations for emerging superconductivity has been discussed since the phase diagram was first established.

Within this thesis the focus is on the $\mathrm{BaFe_2As_2}$ family which exhibits a combined magnetic and structural phase transition for pure samples at $T_s = T_\mathrm{N} = 135\,\mathrm{K}$ [92]. On electron doping T_N is more rapidly suppressed than T_s and a nematic phase emerges. The origin of the nematic phase is still unclear, but there are two possible scenarios (spin or orbital order driven) discussed (see Chapter 4.1.1). The superconducting phase competes with nematicity. Therefore nematicity might be a key to understanding unconventional superconductivity.

Since the nematic/structural phase transition is driven by magnetic/orbital degrees of freedom, there is, apparently, a strong coupling between the magnetic/orbital degrees of freedom and the lattice [93]. There is experimental evidence that the structural transition from tetragonal to orthorhombic is driven by magnetism, which underlines this coupling [94]. As a consequence lattice dynamical studies are can be used to examine nematicity.

The outline of the remainder of this chapter will be as follows. In Chapter 4.1 the basic physical properties of the $BaFe_2As_2$ family and especially the structural phase transition of the cobalt doped compounds will be discussed. The results of previous work on optimally doped $Ba(Fe_{x-1}Co_x)_2As_2$ ($x \approx 0.06$) that lead to a puzzling discrepancy between INS results and measurements of the elastic moduli will be shown in Chapter 4.2. To answer the open question of the difference between those two measurements more inelastic neutron scattering data was taken (see Sec. 4.3.1). The results were used to develop a theoretical model [(together with J. Schmalian (KIT) and R. Fernandes (University of Minnesota)] for the nematic fluctuations and a new quantity, the nematic correlation length, will be introduced in Chapter 4.3.2. The results of further measurements on optimally doped $Ba(Fe_{x-1}Co_x)_2As_2$ addressing the temperature dependence of the phonon lifetime (see Sec. 4.3.3) and the phonon dispersion (see Sec. 4.3.4) are shown in this chapter. In the last Chapter 4.3.5 the first measurements on hole doped samples using inelastic x-ray scattering will be discussed.

4.1 Motivation

4.1.1 Basics

There are various types of iron-based superconductors which are named according to their crystal structure. The shared, central, structural element of these compounds is a quasi-two-dimensional FeX sheet. The X = As, P, S, Se or Te atoms occupy slightly distorted tetrahedral positions above and below a square array of Fe ions (Fig. 4.1).

Most of these systems become superconducting by chemical substitution of various elements in the parent compound or by applying hydrostatic pressure. A schematic phase diagram of the $BaFe_2As_2$ family is shown in Figure 4.2 since it is the class of materials studied and described in this thesis.

In the undoped parent compound $BaFe_2As_2$ the orthorhombic distortion and the stripe-type antiferromagnetism, which are closely connected by symmetry, nearly [95] coincide. Upon electron doping they split continuously. Here the structural transition precedes the magnetic one, but it is still unanswered which instability is the primary one [89]. The fact that both transitions track each other closely in most phase diagrams leads to the assumption that they are intimately connected. In the temperature between those two transitions an orthorhombic and a paramagnetic phase emerges where the rotational symmetry is broken but time-reversal symmetry is still preserved. Since the order parameter here defines an axis but has no sense of direction, similar to the order parameter in the nematic phase of liquid crystals, this order is also called nematic. A dome of superconductivity (yellow) emerges upon both hole and electron doping in the vicinity of the doping range where the structural and magnetic phase transitions are suppressed. The interrelationship of these phases could be the key to understanding the fundamental mechanism responsible for the emergence of superconductivity in the iron-based systems.

The effects of the nematic order can be observed in many other quantities like transport [96], occupation of orbitals [97], spin excitations [98], Young's modulus [99] and charge fluctuations [100]. In most of those measurements the nematicity manifests itself in a directional dependence which already emerges clearly above the structural/magnetic phase transition due to nematic fluctuations (red shaded area in Fig. 4.2). The twinning in the orthorhombic phase typically aggravates the observation of this directional dependence. The samples have to be detwinned, i.e. by uniaxial stress. There is still an ongoing argument about the origin of the electronic nematic behavior in iron-based superconductors, both spin and orbital scenarios have been proposed [101].

.

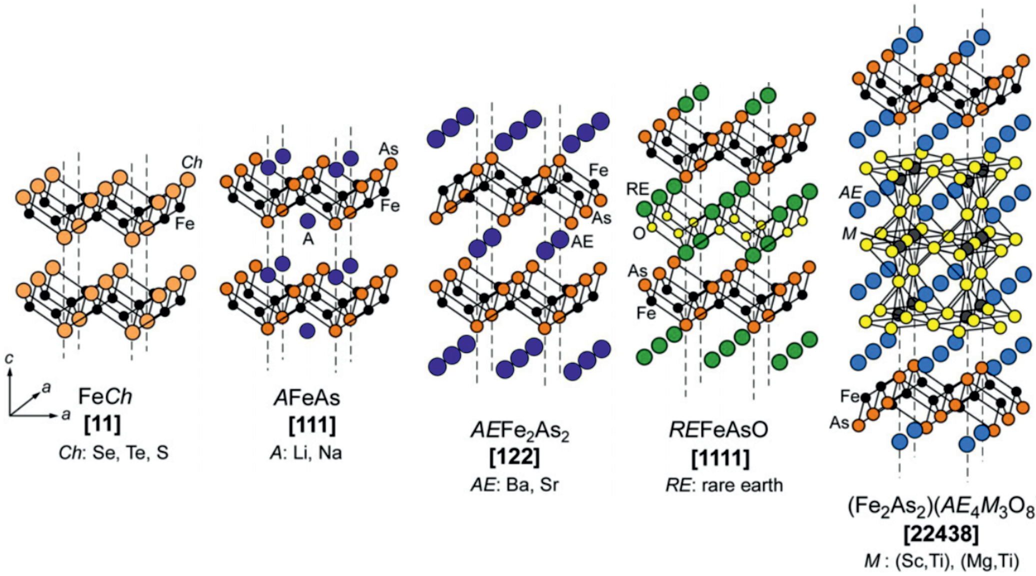

Figure 4.1: Crystal structures of representatives of iron-based superconductors. The most common families 11, 111, 122, 1111 and one example of a more complex-system 22438 (containing a perovskite-type oxide layer). The common structural element of all systems are FeX sheets (with X = As, Se, Te, S or P) in which the Fe atoms are arranged on a square lattice with a pnictogen or chalcogen atom in tetrahedral coordination around them. [86]

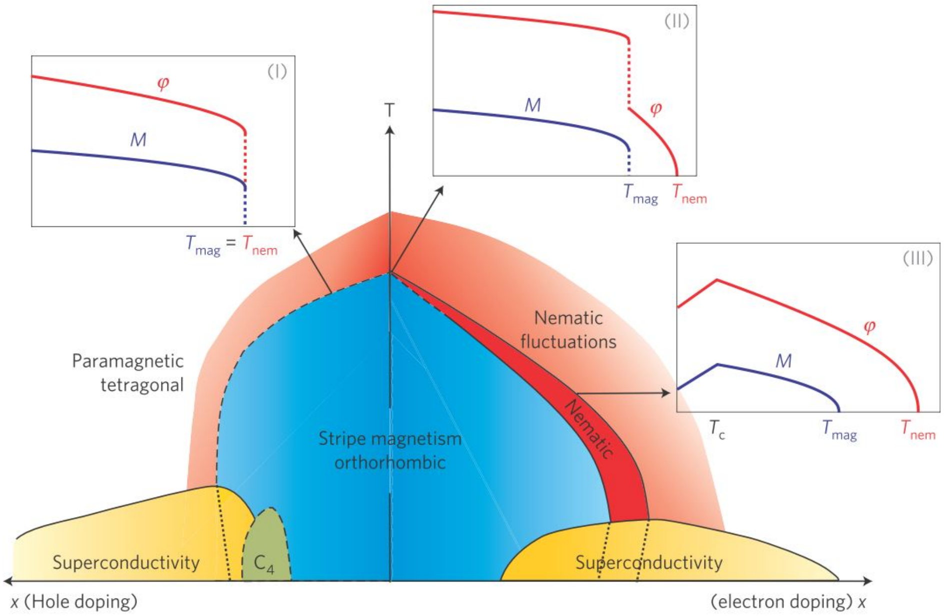

Figure 4.2: Schematic phase diagram of hole-doped and electron-doped iron pnictides of the $BaFe_2As_2$ family. The blue area denotes stripe-type orthorhombic magnetism, the red area denotes nematic/orthorhombic paramagnetic order and the yellow are superconductivity. The green area corresponds to a magnetically ordered state with tetragonal (C_4) symmetry. The dark red region denotes to a regime with strong nematic fluctuations. The dotted lines illustrate the magnetic and nematic transition lines inside the superconducting dome. Second-order (first-order) transitions are denoted by solid (dashed) lines. The insets show the temperature-dependence of the nematic (ϕ) and magnetic (M) order parameters in different regions of the phase diagram: region (I) corresponds to simultaneous first-order magnetic and nematic transitions; region (II) corresponds to split second-order nematic and first-order magnetic transitions; and region (III) corresponds to split second-order transitions. At $x = 0$ the transitions are split, like in region (II), but their separation is small. [89]

In one model the main idea is that the orbital order can induce changes in the magnetic correlation length what could lead to magnetism [102, 103]. The starting point is the degeneracy of the iron d_{xz} and d_{yz} orbitals in the tetragonal phase. Basically this degeneracy can be lifted by a distortion quite similar to the Jahn-Teller effect, which would lead to a lowering of the total energy of the system (Fig. 4.3). In this case the nematic order parameter is given by the difference in the orbital occupation. In this model the structural transition naturally occurs above the magnetic one. On the other hand, the magnetic transition does not have to take place at all in this scenario.

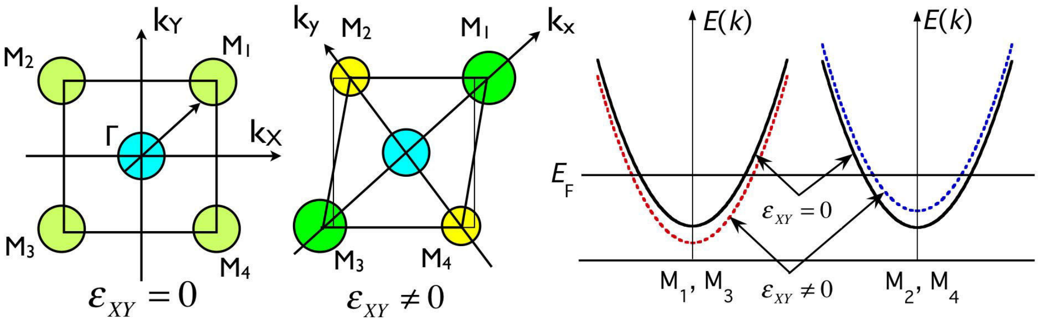

Figure 4.3: Schematic drawing of how the orthorhombic distortion ϵ_{XY} (left) may lift the degeneracy of the electronic dispersion near M points of the Brillouin zone and induce anisotropic orbital occupation [104].

The spin-nematic model is built on spin fluctuations as the driving force for the structural and magnetic transition [89]. The observed magnetic order of the Fe atoms is of the stripe type with the in-plane ordering vectors $\mathbf{Q}_1 = (\pi, 0)$ or $\mathbf{Q}_2 = (0, \pi)$, where along one direction the spins are parallel to each other and anti-parallel along the other [105] [Fig. 4.4 (a)]. The symmetry of the magnetic order parameter is not only the spin rotational $O(3)$ which is broken for any magnetic state but also a discrete, two-fold (Ising-type) Z_2 symmetry that describes the orientation of the ferromagnetic stripes. The latter reduces the 90 ° lattice rotational symmetry to 180 ° by choosing between the ordering vectors $\mathbf{Q}_1$ and $\mathbf{Q}_2$. The order parameter is then enhanced by the additional tetragonal symmetry breaking to $O(3) \times Z_2$. The two ordering vectors can be associated with two magnetic order parameters $\mathbf{M}_1$ and $\mathbf{M}_2$. The breaking of the $O(3)$ symmetry means $\langle \mathbf{M}_i \rangle \neq 0$ and breaking the Z_2 symmetry $\langle M_1^2 \rangle \neq \langle M_2^2 \rangle$ [104]. As calculations by Fernandes *et al.* [90] show, spin fluctuations might lead to an intermediate phase at $T_{\mathrm{mag}} < T < T_{\mathrm{nem}}$ where the tetragonal Z_2 symmetry is already broken (and an orthorhombic distortion occurs) but the spin-rotational $O(3)$ symmetry is not ($\langle M_1^2 \rangle \neq \langle M_2^2 \rangle$, because $\langle \mathbf{M}_i \rangle = 0$. This order is by definition nematic (additional lowering of the rotational symmetry), which is an unconventional magnetic order with time-reversal symmetry preservation (see Fig. 4.4). Moreover this could explain why, even with magnetic fluctuations as a driving force for both transitions, the structural precedes the magnetic transition. As shown in figure 4.4(b), the stripe magnetic state can be visualized in real space by dividing the square iron-lattice into two inter-penetrating Néel sublattices with staggered magnetizations $\mathbf{M}_A = \mathbf{M}_1 + \mathbf{M}_2$ and $\mathbf{M}_B = \mathbf{M}_1 - \mathbf{M}_2$. The nematic state is characterized by the spin nematic order parameter $\Psi = \langle \mathbf{M}_A \cdot \mathbf{M}_B \rangle$ (while $\langle \mathbf{M}_i \rangle = 0$) which determines the orientation of the ferromagnetic stripes.

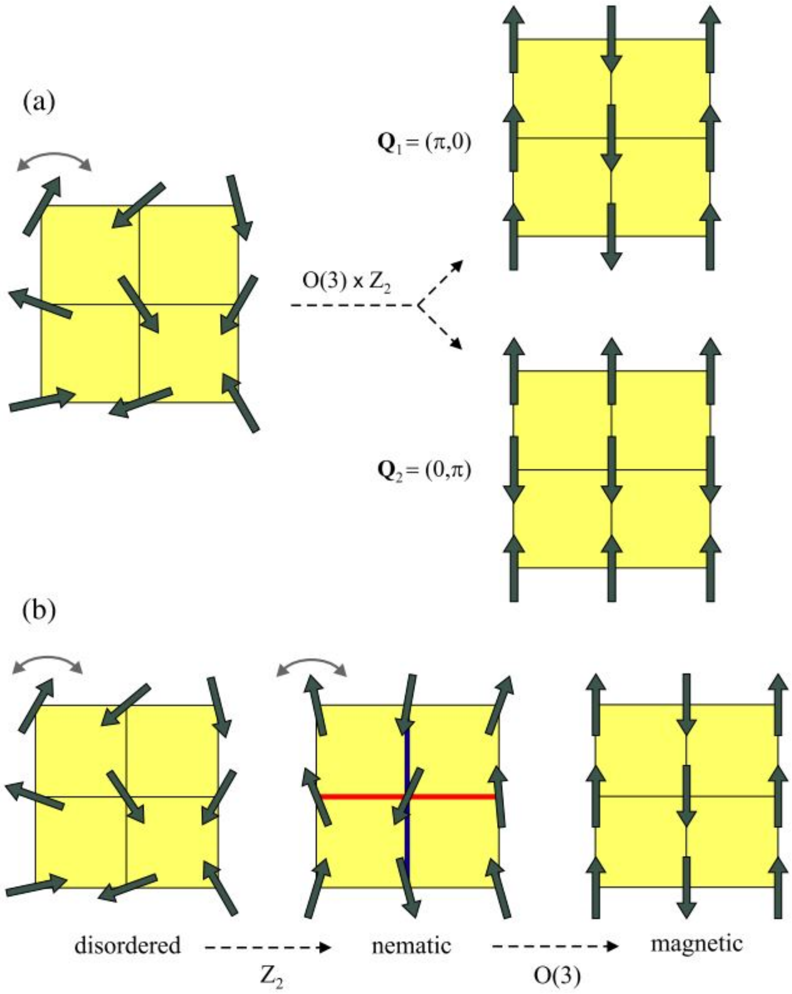

Figure 4.4: Schematic representation of nematic transition in real space. (a) The transition from the disordered phase to the SDW phase breaks an $O(3)\times Z_2$ symmetry. The $O(3)$ symmetry refers to rotations in spin space while the Z_2 (Ising) symmetry refers to the two degenerate ground states of magnetic stripes with parallel spins along the y axis (ordering vector $\mathbf{Q}_1 = (\pi, 0)$) or along the x axis (ordering vector $\mathbf{Q}_2 = (0\,, \pi)$). (b) The $O(3) \times Z_2$ symmetry can be broken in two steps. First, only the Z_2 symmetry is broken: the system is still paramagnetic, since $\langle \mathbf{S}_i \rangle = 0$ (indicated by the gray double arrow on top of the spins), but the spin correlations break the tetragonal symmetry, $\langle \mathbf{S}i \cdot \mathbf{S}_{i+\mathrm{x}} \rangle = -\langle \mathbf{S}i \cdot \mathbf{S}_{i+\mathrm{y}} \rangle$ (red and blue bonds, respectively). In the second step, the $O(3)$ symmetry is broken and the system acquires long-range magnetic order. [104]

4.1.2 The structural phase transition in Ba($Fe_x$$Co_{1-x}$)$_2$$As_2$

In the crystals structure of $BaFe_2As_2$, barium atoms sit between sheets of iron and arsenic atoms [Fig. 4.5(a)]. Figure 4.5(b) shows the schematic phase diagram of cobalt doped $BaFe_2As_2$. In the undoped parent compound a simultaneous structural and magnetic phase transition at $T_{s,\mathrm{N}} \approx 140\,\mathrm{K}$ can be observed. The tetragonal and paramagnetic high-temperature phase becomes orthorhombic and antiferromagnetic with a stripe order of the spins [106]. Moreover, a superconducting dome, with the highest $T_c \approx 25\,\mathrm{K}$ for the optimally doped sample with a cobalt amount of $x \approx 6\,\%$, emerges close to the point where both the structural and magnetic phase transitions are suppressed.

The tetragonal unit cell is defined with its axes along the next-nearest neighbor iron atoms. The distortion of the structural phase transition manifests itself in a shear distortion between the tetragonal in-plane axes (see Fig. 4.6) and corresponds to the transverse acoustic phonon along one of the two main tetragonal directions with a polarization in the a-b-plane. In the antiferromagnetic phase the orthorhombic unit cell is then two times larger and rotated by 45 ° compared to the tetragonal one. The transition is accompanied by the formation of four degenerate domains. In the following the wave vectors will always be given in the tetragonal notation if not stated otherwise.

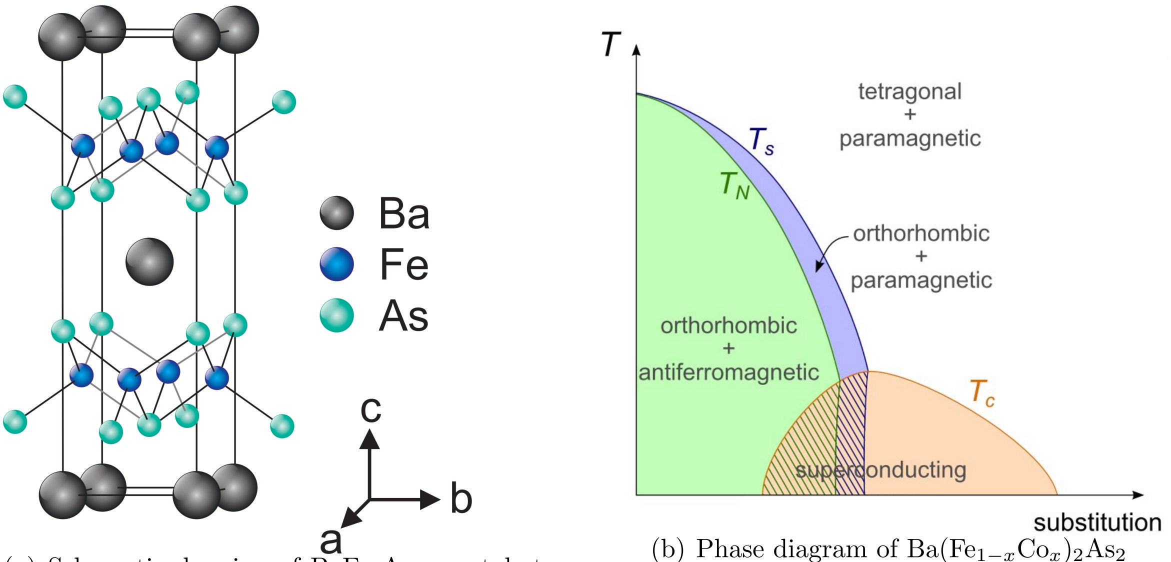

(a) Schematic drawing of $BaFe_2As_2$ crystal structure

(b) Phase diagram of Ba($Fe_{1-x}$$Co_x$)$_2$$As_2$

Figure 4.5: (a) Schematic drawing of the crystal structure of $BaFe_2As_2$. See [107]. (b) Phase diagram of Ba($Fe_{1-x}$$Co_x$)$_2$$As_2$. [108]

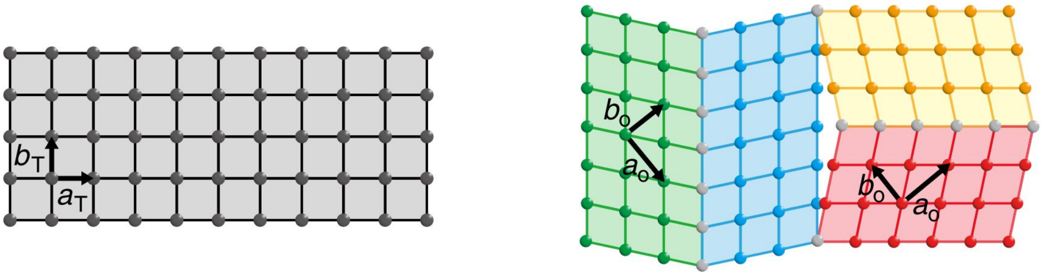

Figure 4.6: Schematic Ba atom arrangements in the basal plane of $Ba(Fe_{1-x}Co_x)_2As_2$ and the formation of four degenerate domains on the structural phase transition sketched by different colors. The tetragonal phase for $T > T_s$ (left) and the orthorhombic phase for $T < T_s$ (right). a_T and b_T are the tetragonal and a_O and B_O the orthorhombic lattice constants. [109]

$BaFe_2AS_2$ exhibits a mixed-order phase transition with a partial discontinuity in the order parameter at the transition temperature. On doping the second-order character becomes more dominant. The order parameter Q is given by the monoclinic strain $a_m c_m \cos\beta$ [110]. The temperature dependence of the order parameter can for example be determined by using elastic scattering to measure the splitting of the Bragg peak $(200)_m$, which is twice the deviation angle from $90\,^\circ$. Figure 4.7(a) displays that in the underdoped $Ba(Fe_{1-x}Co_x)_2As_2$ ($x = 4.7\,\%$) sample the order parameter is decreasing monotonically towards the transition temperature $T_{s,\mathrm{N}}$. The transition occurs continuously and its character therefore is mostly second-order. A typical feature of second-order structural transitions is a soft phonon mode. There are two distinct scenarios for soft phonon modes depending on the ordering wave vector of the distorted lattice. If $\mathbf{q}$ is nonzero, a phonon at finite energy with an atomic displacement pattern corresponding to the incipient structural phase transition softens on cooling and reaches zero energy at the phase transition temperature. Simply speaking the phonon displacement pattern freezes into the static lattice distortion at T_s. If the ordering wave vector is zero, the soft phonon mode is an acoustic mode. In this scenario, which applies to the situation in the 122 family of iron-based superconductors, the slope of the dispersion of the soft acoustic mode softens on cooling towards the phase transition temperature. The slope of the phonon dispersion at the transition temperature is zero, i.e. a small distortion corresponding to the phonon displacement pattern can be done without any cost in energy. Below the structural transition temperature, the slope of the dispersion increases on further cooling. The temperature dependence described above is typically restricted to a small region of reciprocal space around the finite or zero ordering wave vector $\mathbf{q}$. As an example we show results for the seminal A-15 superconductor Nb_3Sn in Figure 4.7(b). This material, which is used for superconducting magnets [111], has

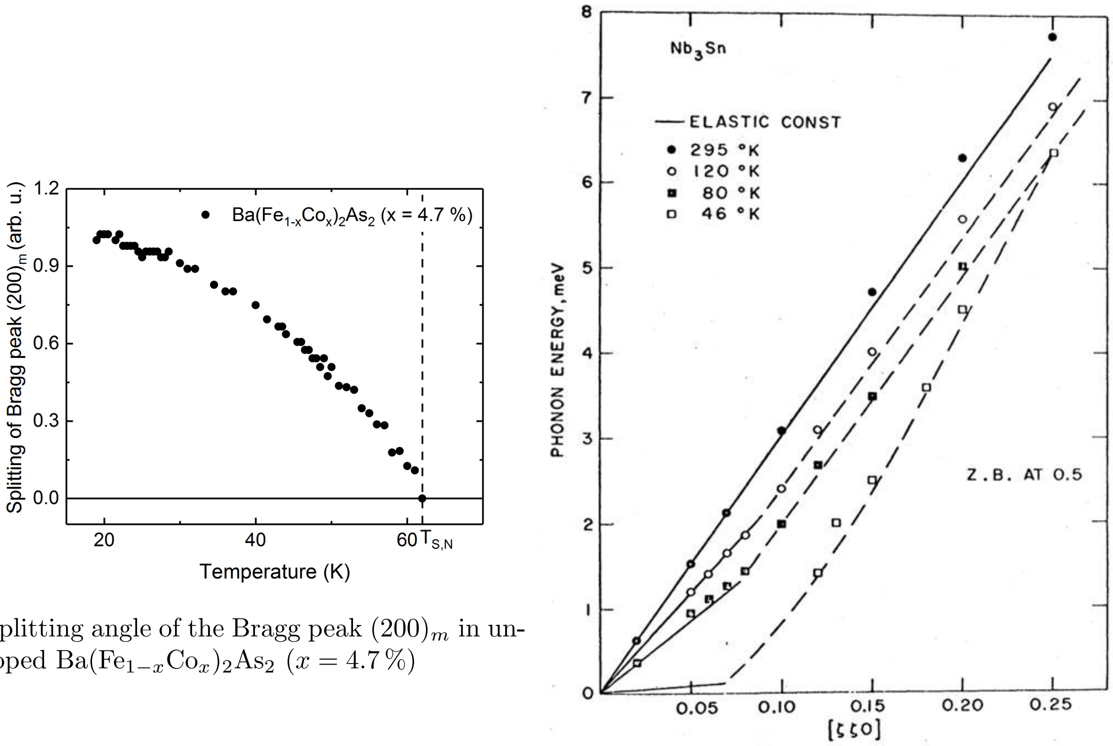

(a) Splitting angle of the Bragg peak $(200)_m$ in underdoped $Ba(Fe_{1-x}Co_x)_2As_2$ ($x = 4.7\,\%$)

(b) Soft phonon mode in Nb_3Sn

Figure 4.7: (a) Temperature dependence of the splitting angle of the Bragg peak $(200)_m$ in an underdoped $Ba(Fe_{1-x}Co_x)_2As_2$ ($x = 4.7\,\%$) sample. The splitting of the Bragg peak in the orthorhombic phase was measured by neutron diffraction. (b) Acoustic phonon dispersion curves for wave vectors parallel to $\mathbf{q}\,[110]$ with a polarization in $[1\bar{1}0]$ direction in Nb_3Sn for different temperatures (symbols). Elastic moduli (solid curve) from [113]. [112]

a structural phase transition at $T_s = 43\,\mathrm{K}$ [112]. The symbols represent the phonon energy measured with inelastic neutron scattering, the dashed lines are a guide to the eye. The solid line shows the elastic constant measured with ultrasound [113] and corresponds to C_{66} in Ba122 in our measurements. For high temperatures ($T = 295\,\mathrm{K}$, black dots) the phonon dispersion is linear. On cooling the dispersion becomes nonlinear with the highest curvature just above T_s ($T = 46\,\mathrm{K}$). The soft phonon mode can also be seen in overdoped and optimally doped $Ba(Fe_{1-x}Co_x)_2As_2$ ($x = 6\,\%$) used for the investigations reported in this thesis. Although there is no actual structural phase transition it can be observed as a precursor effect.

Due to the unique physics of the Ba122 family the structural phase transition is also nematic (see Chapter 4.1.1). In the following this nematic/structural phase transition is often referred to as nematic phase transition for a better readability. There are different

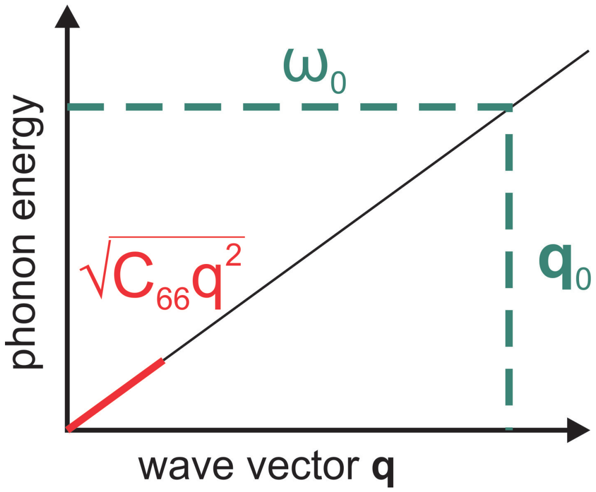

Figure 4.8: Comparison of C_{66} and INS measurements of a linear phonon dispersion. Ultrasound and three-point bending measurements probe the shear modulus/Young's modulus at $\mathbf{q} = 0$. Since the dispersion of the TA soft mode at small wave vectors is given by $\sqrt{C_{66}q^2}$ (red), we can extract the slope of the dispersion from C_{66} and compare it to the slope corresponding to the inelastic neutron scattering results at finite wave vectors. Inelastic neutron scattering measurements are carried out at finite $\mathbf{q}$ (turquoise).

methods of investigating the nematic fluctuations in iron-based superconductors. $C_{66} \equiv \mathrm{C}_{66}(\mathbf{q} = 0)$ has been measured either directly by resonant ultrasound [103] or indirectly via Young's modulus $Y_{[110]}$ in three-point bending setups [114]. In three-point bending setups Young's modulus along [110] is dominated by the elastic shear modulus C_{66} as long as C_{66} is smaller the other C_{ij} [108]:

$$Y_{[110]} = 4\left(\frac{1}{C_{66}} + \frac{1}{\gamma}\right)^{-1} \quad \text{with} \quad \gamma = \frac{C_{11}}{2} + \frac{C_{12}}{2} - \frac{C_{13}^2}{C_{33}} \tag{4.1}$$

The elastic constants determined from these techniques are directly linked to the slope of the acoustic phonon dispersion at zero momentum transfer $\mathbf{q} = 0$ (Fig. 4.8). Hence, measurements of C_{66} in Ba122 can be directly compared to phonon measurements with inelastic scattering but keeping in mind that acoustic phonons can only be measured by INS at finite wave vectors. However, for a linear dispersion it should be equivalent to the ultrasound and three-point bending measurements, since it measures the same slope of the dispersion.

Figure 4.9 displays shear modulus measurements with ultrasound [Fig. 4.9(a)] and three-point bending [Fig. 4.9(b)] for differently doped $\mathrm{Ba(Fe_{1-x}Co_x)_2As_2}$ samples. Both measurements are in reasonable agreement to each other except for the given concentrations. The observed effects are similar but occur at different concentrations. The concentrations from Böhmer *et al.* [99] were determined with the same experimental setups in crystals from the same crystal grower as the samples we used. In the following we compare our data to the measurements of Böhmer *et al.*. Strongly overdoped samples exhibit a small hardening on cooling as they do not show any nematic fluctuations. In slightly overdoped and optimally doped samples a softening on cooling towards the superconducting transition temperature T_c is followed by a smaller hardening below T_c. Underdoped samples which show a structural phase transition exhibit strong softening towards T_s. C_{66} measurements in the orthorhombic phase are not reliable because the temperature evolution of C_{66} in different domains in the naturally twinned samples strongly affect each other. Comparing all samples the softening is more pronounced the less cobalt the sample contains. Inelastic neutron and x-ray scattering are capable of predicting the evolution of the TA mode also in the orthorhombic phase which was the motivation for INS measurements prior to this work.

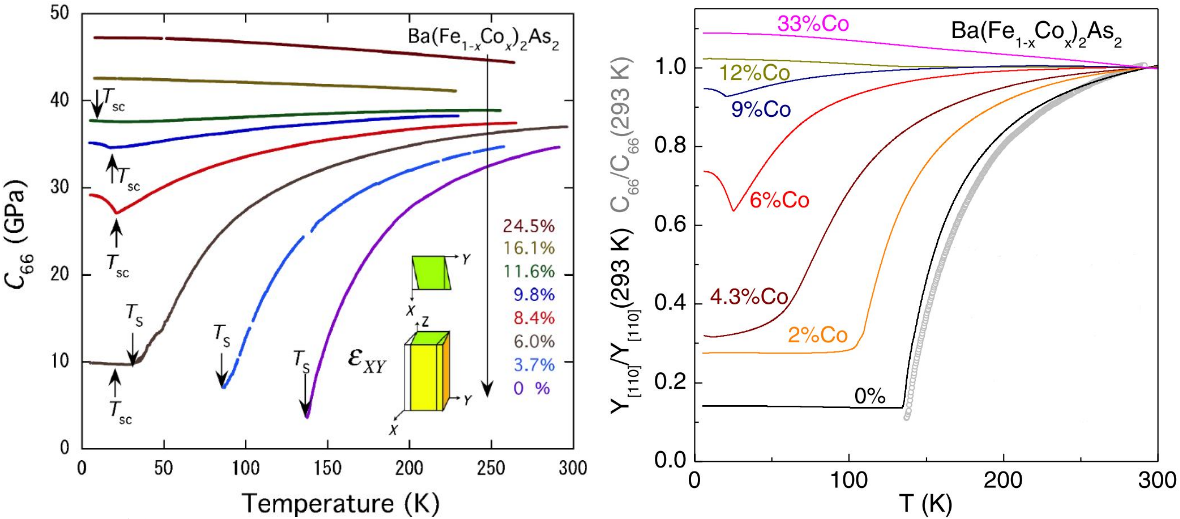

(a) Elastic shear modulus C_{66}

(b) Young's modulus

Figure 4.9: (a) Elastic shear modulus C_{66} for a wide substitution range of $Ba(Fe_{1-x}Co_x)_2As_2$ measured using ultrasound. [103] (b) Young's modulus of of $Ba(Fe_{1-x}Co_x)_2As_2$ normalized at room temperature. For comparison the C_{66} mode of pure $BaFe_2As_2$ measured by Yoshizawa *et al.* [103] (gray circles) is shown [114]. The cobalt concentrations of both measurements are deviant, for further discussion see text.

4.2 Previous results from inelastic neutron scattering

The original idea of the present project on inelastic neutron and x-ray scattering was to determine the temperature dependence of the phonon energy and the peak position of the soft phonon mode. The focus here was mainly on samples which show a tetragonal to orthorhombic transition, as the ultrasound and three-point bending measurements are not reliable here (see Chapter 4.1.2). Parshall *et al.* [92] had found a close relation between magnetic properties and the soft phonon mode of the structural transition in $BaFe_2As_2$ and $SrFe_2As_2$. The observed transverse acoustic phonons propagate along the tetragonal [1 0 0] direction and are polarized along [0 1 0]. The distortion from tetragonal to orthorhombic symmetry is accompanied by the transition to the antiferromagnetically ordered state at $T_{s,\mathrm{N}} = 135\,\mathrm{K}$ in $BaFe_2As_2$. The TA phonon softens for small $\mathbf{q} = 0.07$ on cooling towards T_s and hardens abruptly below T_s (Fig. 4.10). For a higher $\mathbf{q} = 0.25$ the softening above T_s can not be observed but below the transition temperature a smaller hardening still takes place. Here and in $SrFe_2As_2$ it is found that the closer to the Bragg peak the phonon is measured the stronger the effects of softening and hardening are. The effects should be in reasonable agreement to the previously reported shear modulus in $BaFe_2As_2$ based on resonant ultrasound measurements if extrapolated to $\mathbf{q} = 0$. The discrepancy in the strength of the hardening below T_s might be explained by the twin domain boundaries in the orthorhombic phase which influence the ultrasound measurements but not the phonon energy measurements. Furthermore they found that the softening of the examined phonon modes in both undoped compounds is proportional to the volume of fluctuating magnetic domains.

Other investigations focused on samples where the structural phase transition is suppressed. Inelastic neutron scattering measurements were done on optimally doped $Ba(Fe_{1-x}Co_x)_2As_2$ with $x = 6\,\%$ to check the comparability to the ultrasound and three-point bending measurements. Figure 4.11 shows the comparison of INS momentum scans to the data from three-point bending measurements from Böhmer *et al.* [114].

In the momentum scans a phonon softening leads to an increasing $\mathbf{Q}$, e.g. K value. That means that the phonon is shifted further away from the Bragg peak. Since the reader might be used to a decreasing phonon energy for a phonon softening the y-axis in Figure 4.11 is inverted. The data from the three-point bending measurement were scaled to fit the high temperature values of the INS data. The neutron data shows a softening towards $T_c \approx 25\,\mathrm{K}$ with kind of a plateau just above the transition temperature. Below T_c a further softening can be observed. The red curve is based on Young's modulus and scaled to the neutron data. It also exhibits a softening towards T_c but other than the inelastic neutron data the softening becomes stronger below $T < 70\,\mathrm{K}$ where the INS data is more or less constant. Furthermore the three-point bending data

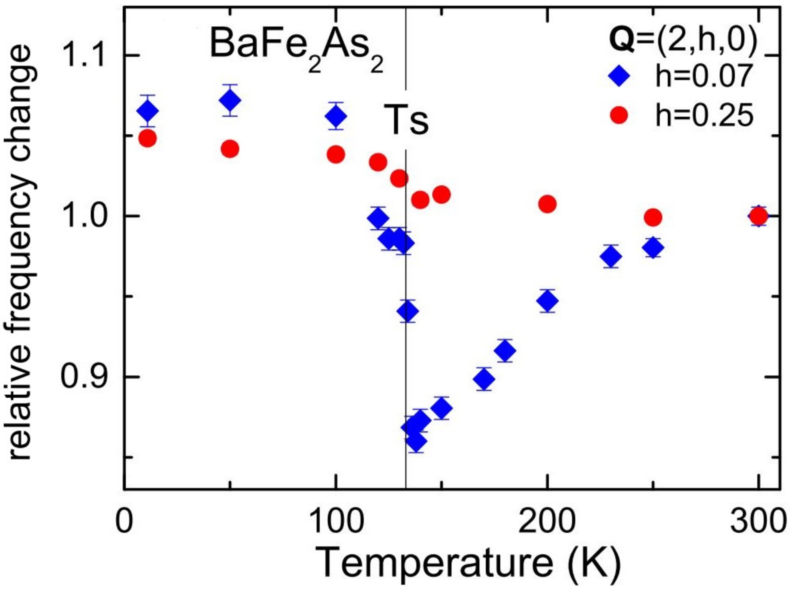

Figure 4.10: Phonon renormalization in $BaFe_2As_2$ as a function of temperature at the wave vector $\mathbf{Q} = (2, h, 0)$. Shown is the relative phonon frequency change as a function of temperature for two different wave vectors with $h = 0.07$ (blue) and $h = 0.25$ (red). [92]

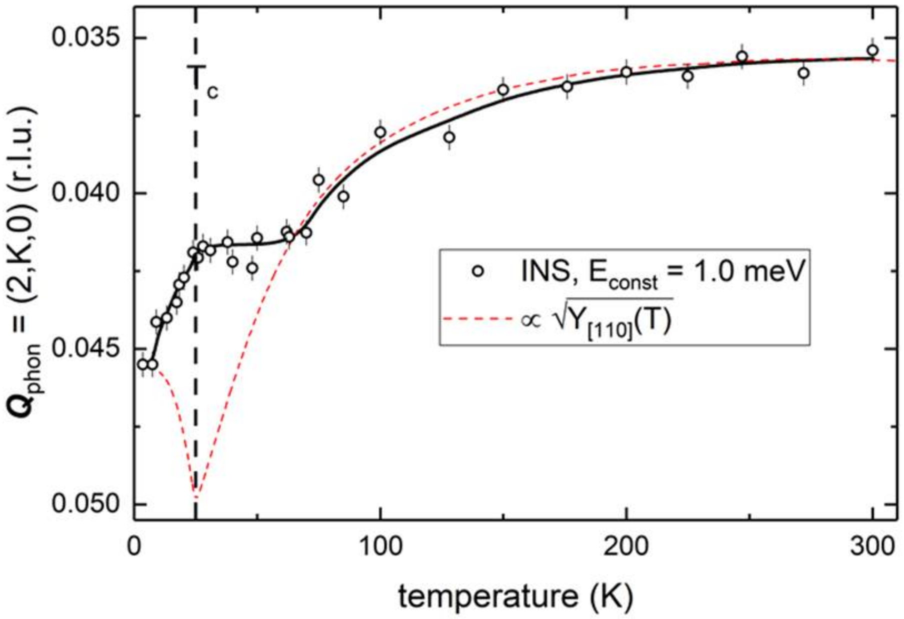

Figure 4.11: Temperature dependence of the peak positions extracted from momentum scans along the tetragonal $\mathbf{Q} = (2, K, 0)$, $-0.1.\,\text{r.l.u.} \leq K \leq 0.1\,\text{r.l.u.}$ (reciprocal lattice units), with a constant energy transfer of $E = 1.0\,\text{meV}$. Because a phonon peak position at an increasing value of K corresponds to a softening of the phonon mode, the vertical $\mathbf{Q}$ scale is plotted upside down for convenience, i.e. resulting in a graphically similar plot to Fig. 4.9. The solid line is a guide to the eye. The dashed (red) line denotes the expected behavior because of the three-point bending measurements on a sample with the same doping [114]. The results from three-point bending were scaled to match the evolution of the INS data in the temperature range $100\,\text{K} \leq T \leq 300\,\text{K}$. The vertical dashed line denotes the superconducting transition temperature $T_c = 25\,\text{K}$ in our sample. [115]

exhibits a hardening below T_c in contrast to the further softening in the INS data. This discrepancy for $T < 70\,\mathrm{K}$ down to base temperature could not be explained at the at the time the work for this thesis was started.

4.3 Results

To resolve the puzzling discrepancy described above, various experiments have been proposed and were carried out in the framework of this thesis. A four to five times larger sample of optimally doped $\mathrm{Ba(Fe_{1-x}Co_x)_2As_2}$ ($x = 6\,\%$), compared to the $\approx 1\,\mathrm{g}$ sample from previous INS measurements, from the same crystal grower could be reobtained. Moreover the mosaicity of the new sample is significantly better than that of the one used so far ($\approx 0.1\,^\circ$ compared to $\approx 0.6\,^\circ$). A few years ago the sample was handed over to a scientist at the Jülich Centre for Neutron Science (JCNS) for INS, but we managed to recover this larger sample.

Inelastic neutron scattering measurements with a better resolution due to the larger sample size were performed to observe the described effects in the raw data (4.3.1). Furthermore the temperature dependence of the phonon dispersion (chapter 4.3.4) and the phonon lifetime (chapter 4.3.3) were studied. Besides that first inelastic x-ray measurements on various hole doped samples were carried out (chapter 4.3.5). Alongside with the experimental measurements a theoretical model was developed together with Rafael Fernandes (University of Minnesota) and Jörg Schmalian (KIT) to understand and explain the observed behavior (chapter 4.3.2).

4.3.1 Inelastic neutron scattering on 1T

The neutron scattering experiments, both the inelastic measurements on the triple axis spectrometer 1T at the Laboratoire Léon Brillouin and the linewidth determination on TRISP at the Heinz Maier-Leibnitz-Zentrum, were carried out on the same $\mathrm{Ba(Fe_{0.94}Co_{0.06})_2As_2}$ sample with a weight of roughly $4\,\mathrm{g}$ and a mosaic spread of $0.095\,^\circ$ (measured at room temperature on TRISP, see Fig. 4.19).

The wave vectors here and in the following chapters are always given in the tetragonal representation. The momentum transfer $\mathbf{Q} = H\mathbf{a}^* + K\mathbf{b}^* + L\mathbf{c}^*$ is denoted as $\mathbf{Q} = (H,\, K,\, L)$ in reciprocal lattice units (r.l.u.), with $\mathbf{a}^* = \hat{\mathbf{a}}2\pi/a$, $\mathbf{b}^* = \hat{\mathbf{b}}2\pi/b$ and $\mathbf{c}^* = \hat{\mathbf{c}}2\pi/c$. For the experiment at 1T the sample was mounted in the scattering plane that is spanned by the reciprocal lattice vectors $\mathbf{G} = (1,\, 0,\, 0)$ and $\mathbf{G} = (0,\, 1,\, 0)$ and collimator blades were inserted in the neutron beam before and after the sample. Achieving a good resolution required to choose a small final energy of $E_f = 8\,\mathrm{meV}$. The transverse acoustic phonon was measured in energy scans at a fixed $\mathbf{Q} = (2,\, 0.08,\, 0)$ and momentum scans with a constant energy $E = 1.7\,\mathrm{meV}$ in a range from $2\,\mathrm{K} \leq T \leq 300\,\mathrm{K}$. The values for $\mathbf{Q}$ and E were chosen in accordance to the previous INS measurements in Ba122 since the observed effects are stronger close to the Bragg peak. At first the raw data of both energy scans and momentum scans are presented before the temperature dependencies are displayed.

The determination of the background plays a major role in the process of analyzing the data for both types of scans. In Figure 4.12(a) the energy scan at 1.7 meV is shown. It clearly exhibits a spurious signal that is T independent which complicates the fitting process since the scan does not reach the background on both sides of the phonon. The origin of the spurious signal might be that a part of the resolution ellipsoid was also scanned through the tails of the Bragg peak and some of its really high intensity got picked up. The value of the background at this energy (≈ 1 meV) was determined from the different background momentum scans at $E = 1.0$ meV. There is no strong change from base temperature up to $T = 60$ K, so the same background curvature was used at all temperatures and only the constant offset y_0 was fitted and adjusted for each temperature. The background is depends on energy and an exponential fit can be used for fitting the background [see black dotted line in Fig. 4.12(a)].

The experimental phonon spectra can be described using a convolution of a damped harmonic oscillator function including the Bose factor and the experimental Gaussian resolution of roughly 0.4 meV. Figure 4.12 (a) shows both the individual blue dashed lines for the spurious signal (at ≈ 0.8 meV) and the phonon (at ≈ 1.8 meV) and the total fit as a solid red line at $T = 15$ K. If the background [black dotted line in Fig. 4.12(a)] is subtracted from the raw data the scans of two different temperatures can be compared more easily [see Fig. 4.12(b) for $T = 15$ (red solid dots) and $T_c = 25$ K (black open circles)]. A clear narrowing on cooling from T_c can be observed.

For the momentum scans the raw data reaches the background on both sides of the phonon peak, so the background determination is straight forward. Here also a curved background was used [black dotted line in Fig. 4.13(a)] with the same averaged curvature for all temperatures and only the constant offset y_0 was adapted. The phonon peaks in the momentum scans were fitted with a pseudo-Voigt function with a variable Lorentzian contribution. For almost every temperature the Lorentz share was roughly around 10 % using the free fits except for $T = 2$ K where it would have been 40 % but was fixed at 10 % to get consistent data. Figure 4.13 shows background and Bose factor corrected data for $T = 15$ (black open circles) and $T_c = 25$ K (red solid dots). The data analysis reveals a narrowing of the phonon on cooling below T_c.

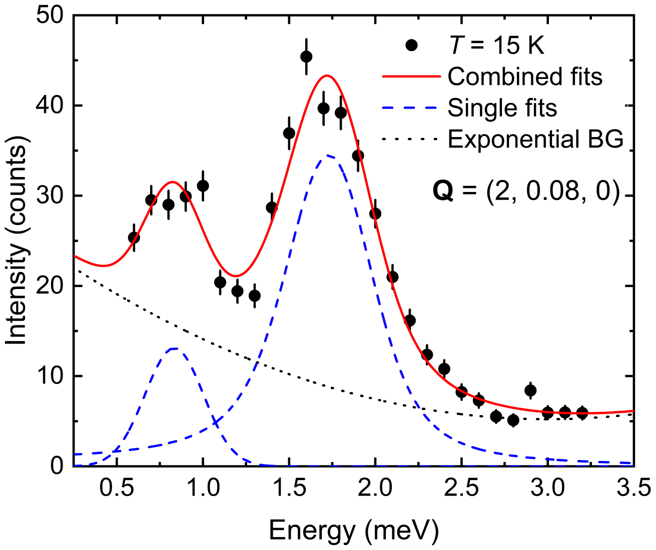

(a) Raw data fitting routine

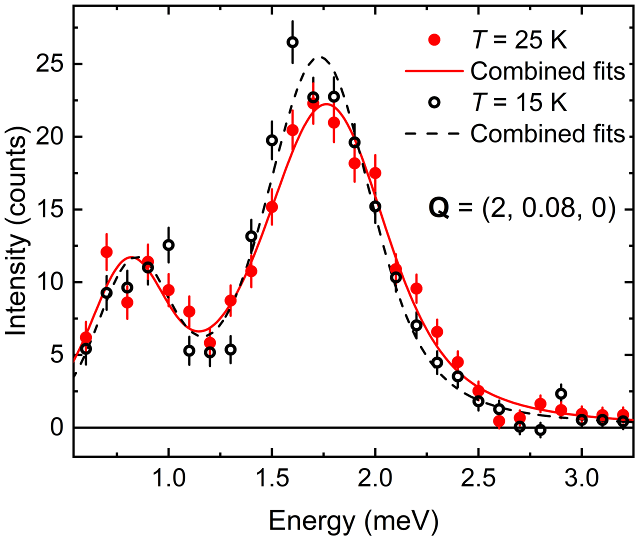

(b) Raw data comparison

Figure 4.12: Raw data of the energy scans at $\mathbf{Q} = (2, 0.08, 0)$. (a) Fitting routine for a typical scan performed at $T = 15\,\mathrm{K}$. The total fit (red solid line) consists of a DHO function convoluted with the Gaussian resolution and a single Gaussian peak for the low energy spurious feature (individual peaks shown as dashed blue lines) and additionally an exponential function as the experimental background (dotted black line). (b) Comparison of the energy scans at $T = 15\,\mathrm{K}$ (black) and 25 K (red). Backgrounds were subtracted and the neutron counts divided by the Bose factor, i.e. 1.3522 for $T = 15\,\mathrm{K}$ and 1.7769 for $T = 25\,\mathrm{K}$ corresponding to the observed energy of the TA mode.

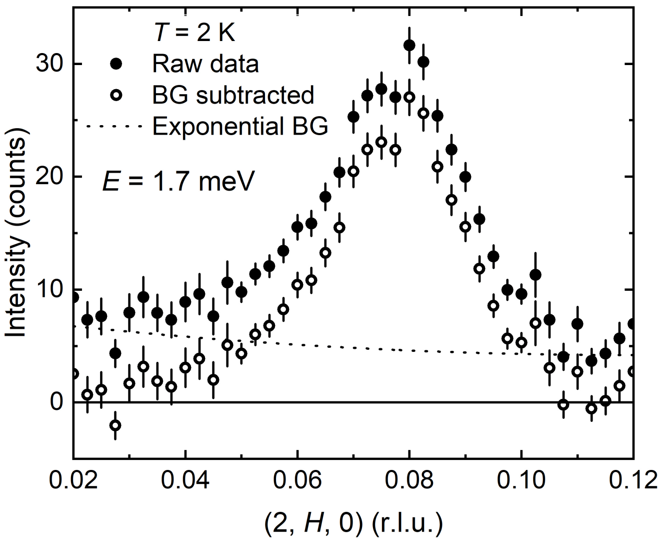

(a) Raw data fitting routine

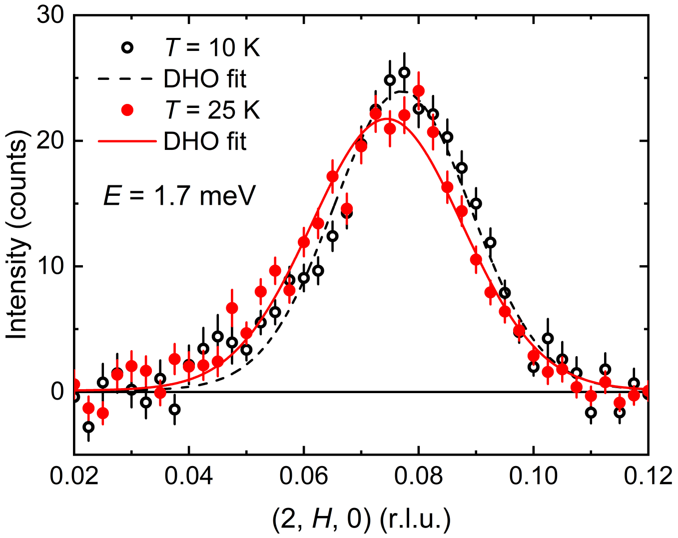

(b) Raw data comparison

Figure 4.13: Raw data of momentum scans at $E = 1.7\,\mathrm{meV}$. (a) Raw data (filled circles) and background (dotted line) for a typical scan performed at $T = 2\,\mathrm{K}$. The open circles represent the background subtracted data. The background on the left side does not reach zero since it was determined in a way that it behaves consistent for all different temperature. (b)Comparison of the momentum scans at $E = 1.7\,\mathrm{meV}$ for $T = 10\,\mathrm{K}$ and $25\,\mathrm{K}$. The backgrounds were subtracted and the neutron counts divided by the Bose factor.

From the fits of the energy scan raw data the phonon linewidth and the phonon energy and from the momentum scans the peak position in momentum space and the the full width half maximum (FWHM) of the phonon peak can be extracted. Figure 4.14 shows the temperature dependence of those values. In the energy scans [4.14(a)] the phonon energy is decreasing towards T_c which is equivalent with a phonon softening. Furthermore the phonon linewidth is increasing on cooling towards the transition temperature and clearly decreasing below that value. In the momentum scans [4.14(b)] there is a drop in the FWHM when the temperature is below T_c, but more important a softening of the phonon can be observed via the increasing value of K on cooling below the superconducting transition temperature.

If the new data are compared to the previous INS data already mentioned, a good agreement between both can be found. Both show a softening on cooling towards $T = 70\,\mathrm{K}$ followed by a plateau and a further softening below T_c. A main difference in the new data is that the softening on cooling below T_c is quite abrupt and is followed by a temperature range of constant energy down to base temperature in contrast to a continuous softening observed in the previous measurements. However, the new data strongly support the previous results. Therefore there is no need to measure each wave vector or energy transfer again. It has to be stated that gathering the new data presented here took about ten days of beamtime at 1T. Due to this accordance of the data it is instructive to use the previous data for a comparison with a model.

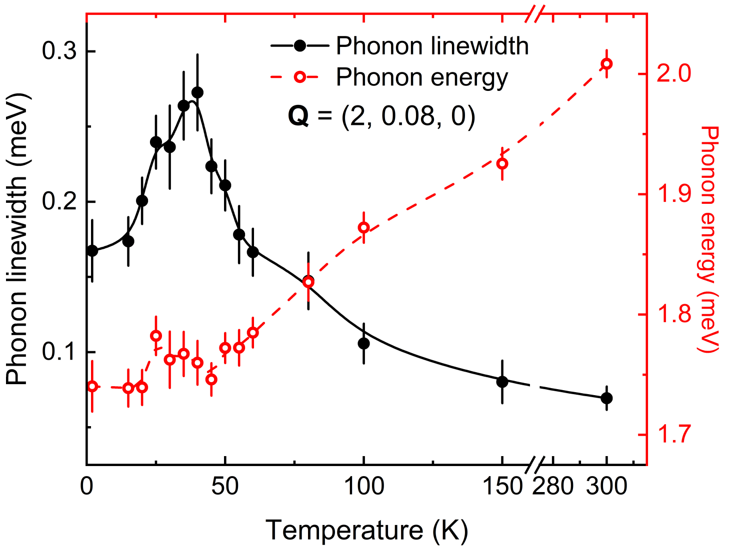

(a) Energy scans

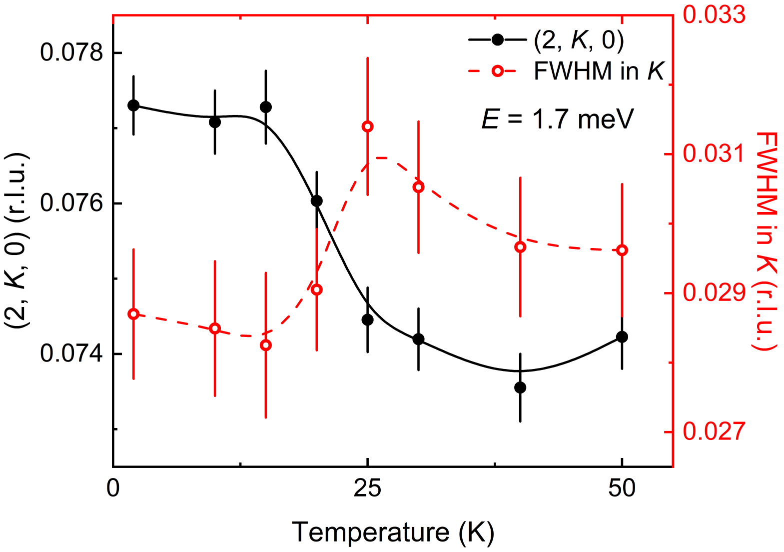

(b) Momentum scans

Figure 4.14: Temperature dependence of (a) the phonon energy (red) and linewidth (black) as deduced from the energy scans at $\mathbf{Q} = (2, 0.08, 0)$ and (b) the position $(2, K, 0)$ (black) and linewidth (FWHM in K) (red) as deduced from the momentum scans at $E = 1.7\,\mathrm{meV}$. The lines are a guide to the eye.

4.3.2 Theoretical model

During this thesis a theoretical model was developed together with Jörg Schmalian (KIT) and Rafael Fernandes (University of Minnesota) to explain our observations and (potentially) reconcile the inelastic neutron scattering and the three-point bending measurements [115]. The phonon measurements with INS were done at small but finite momentum transfers $\mathbf{q} \neq 0$. In this regime the typical assumption is a strictly linear dispersion [see inset Fig. 4.15(a)]

$$E(\mathbf{q}) = \sqrt{\frac{C_{66}}{\rho}}\,|\mathbf{q}|\,. \tag{4.2}$$

This is applicable for high temperatures $T \gg T_c$, but on cooling towards T_c this linear model does not fit anymore. The experimental data for $T = 250\,\mathrm{K}$ [see Fig. 4.17(a)] can be perfectly described by a linear fit. With this it can be ruled out, that the data points at $T = 28\,\mathrm{K}$ [red dots in Fig. 4.15(b)] can be fitted by a straight line with a small offset in x due to resolution effects but instead show a non-linear behavior with a finite curvature of the dispersion. One model to solve this issue of the non-linear dispersion is to allow a momentum dependent shear modulus $C_{66}(\mathbf{q})$

$$E(\mathbf{q}) = \sqrt{\frac{C_{66}(\mathbf{q})}{\rho}}\,|\mathbf{q}|\,. \tag{4.3}$$

Rafael Fernandes and co-workers [90] derived an expression for the momentum-dependent shear modulus

$$C_{66}(\mathbf{q}) = \frac{C_{66}^{0}}{1 + \frac{\lambda^2}{C_{66}^{0}}\chi_{\mathrm{nem}(\mathbf{q})}} \tag{4.4}$$

which takes the coupling of the nematic fluctuations to the lattice into account with the nemato-elastic coupling constant λ and the nematic susceptibility χ_{nem}. C_{66}^{0} is the pure elastic modulus without nematicity. Furthermore, we introduce the correlation length of nematic fluctuations ξ and write:

$$\chi_{\mathrm{nem}}(\mathbf{q}) = \frac{\chi_{nem}(\mathbf{q} = 0)}{1 + \xi^2 q^2} \tag{4.5}$$

Combining Eqs. 4.2-4.5, the dispersion relation of the TA phonon can be written as

$$E(\mathbf{q}) = \sqrt{\frac{C_{66}^{0}}{\rho\left(1 + \frac{\lambda^2 \chi_{\mathrm{nem}}(\mathbf{q}=0)}{C_{66}^{0}(1+\xi^2 q2)}\right)} q^2}. \tag{4.6}$$

The nematic susceptibility of $\mathrm{Ba(Fe_{0.94}Co_{0.06})_2As_2}$ for zero momentum transfer $\chi_{\mathrm{nem}}(\mathbf{q} = 0)$ is already known from the three-point bending measurements and can be expressed

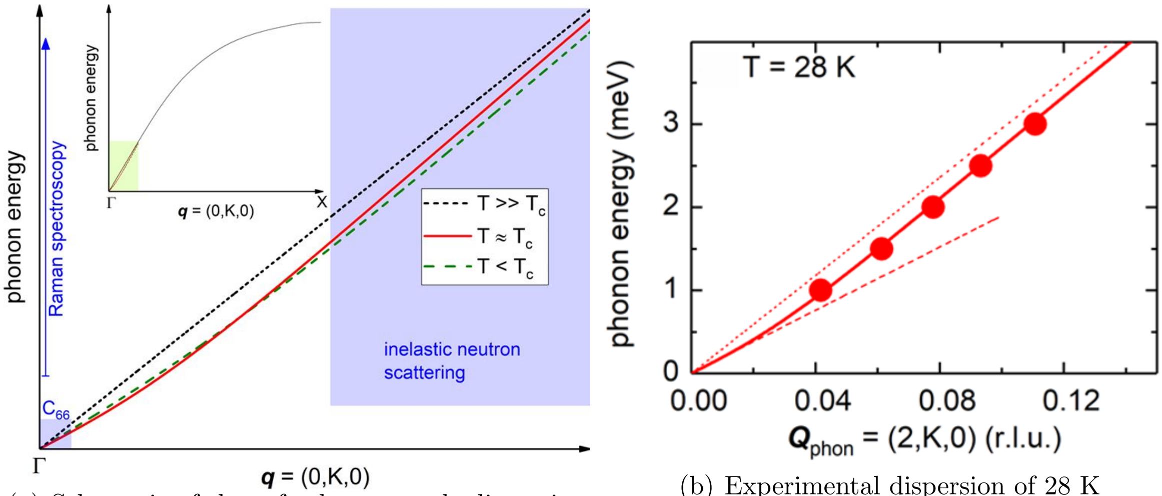

(a) Schematic of the soft phonon mode dispersion

(b) Experimental dispersion of 28 K

Figure 4.15: (a)Schematic of the temperature dependence of the soft phonon mode dispersion observed in $Ba(Fe_{0.94}Co_{0.06})_2As_2$. The inset displays the full dispersion from the zone center, Γ, to the zone boundary, X; the main panel zooms the small-momentum green-shaded area. Shown are the characteristic evolution of the TA dispersion described by Equation 4.6 from high temperatures, $T \gg T_c$, down to the superconducting transition temperature T_c and below, $T < T_c$. The values of ξ used to generate the curves were taken from the fits figure 4.18 at the corresponding temperatures. The blue vertical arrow and shaded areas indicate the energy-momentum range probed by Raman spectroscopy ($\mathbf{q} \approx 0$, $\omega > 0$), measurements of the elastic constant $C_{66}(0)$ ($\mathbf{q} \approx 0$, $\omega = 0$) and the inelastic neutron scattering investigation ($\mathbf{q} \neq 0$). (b) Phonon dispersion measurements of the soft phonon mode of $Ba(Fe_{0.94}Co_{0.06})_2As_2$ at 28 K. The red dots were measured with INS on 1T, the red solid line was fitted with Equation 4.6. The dotted and dashed lines are corresponding to a linear dispersion. [115]

in terms of temperature dependent values of $C_{66}(T)$ and $C_{66}^0(T)$ only with the following equation:

$$\lambda^2 \chi_{\mathrm{nem}}(\mathbf{q}=0) = C_{66}^0 \left(\frac{C_{66}^0}{C_{66}} - 1 \right) \tag{4.7}$$

The final equation to describe the non-linear dispersion relation in the wave vector range of our measurements can be written as

$$E(\mathbf{q}) = \sqrt{\frac{C_{66}^0}{\rho \left(1 + \frac{C_{66}^0 (C_{66}^0 / C_{66} - 1)}{C_{66}^0 (1 + \xi^2 q^2)} \right)} q^2}. \tag{4.8}$$

Although this equation looks complicated, it has just one single fit parameter, i.e., the nematic correlation length ξ. The values for $C_{66}(T)$ and $C_{66}^0(T)$ can be deduced from the already mentioned measurements of Young's modulus $Y_{[110]}(T)$ by Böhmer *et al.* [99]. One can assume that nematic fluctuations are negligible at room temperature, since Young's modulus is nearly temperature independent at $T = 300\,\mathrm{K}$ [see Fig. 4.16(b)], hence $C_{66}(T = 300\,\mathrm{K}) = C_{66}^0(T = 300\,\mathrm{K})$. In the linear phonon dispersion regime with a slope corresponding to $C_{66}(T)$ it is expected that the temperature dependence of $\sqrt{Y_{[110]}}$ and of the phonon energies are equal:

$$E_{\mathrm{Phonon}}(T) \propto \sqrt{Y_{[110]}(T)} \tag{4.9}$$

For $T \geq 90\,\mathrm{K}$ where the phonon dispersion can be well described by linear fits [Fig. 4.17(a)], we can thus extract $C_{66}(T)$ from our phonon measurements.

We need to scale the reported values of Young's moodulus because the three-point bending experiment yields only qualitative values normalized typically to the value at room temperature. Hence, it would be sufficent to just scale the normalized value at $T = 300\,\mathrm{K}$ to that deduced from our INS measurements. However, when $Y_{[110]}/Y_{[110]}(T = 300\,\mathrm{K})$ is plotted only scaled to match the average high temperature value of $C_{66} = 47.9\,\mathrm{GPa}$ (blue dashed line in Fig. 4.16) the softening observed in INS for $T \geq 90\,\mathrm{K}$ is somewhat larger than the temperature dependence of $Y_{[110]}/Y_{[110]}(T = 300\,\mathrm{K})$ suggests. The data shows that C_{66} softens to 63 % of its room temperature value whereas a decrease down to 42 % can be observed when scaled to the phonon softening seen in INS on cooling to $T = 90\,\mathrm{K}$. Physically it would not make sense if the slope of the phonon dispersion at $\mathbf{q} = 0$ results in larger energies than could be observed with at finite momenta INS. One reason for the scaling mismatch could be the presence of strain/pressure that has to be exerted to determine $Y_{[110]}(T)$ with three-point bending technique. Also the alignment of the crystal axis with the experimental setup for the bending experiment may be an error source. This might change the reported temperature dependence compared to the behavior in a non-strained sample. The analysis of the phonon dispersion data (see Figs. 4.17 and 4.18) was based on the red solid

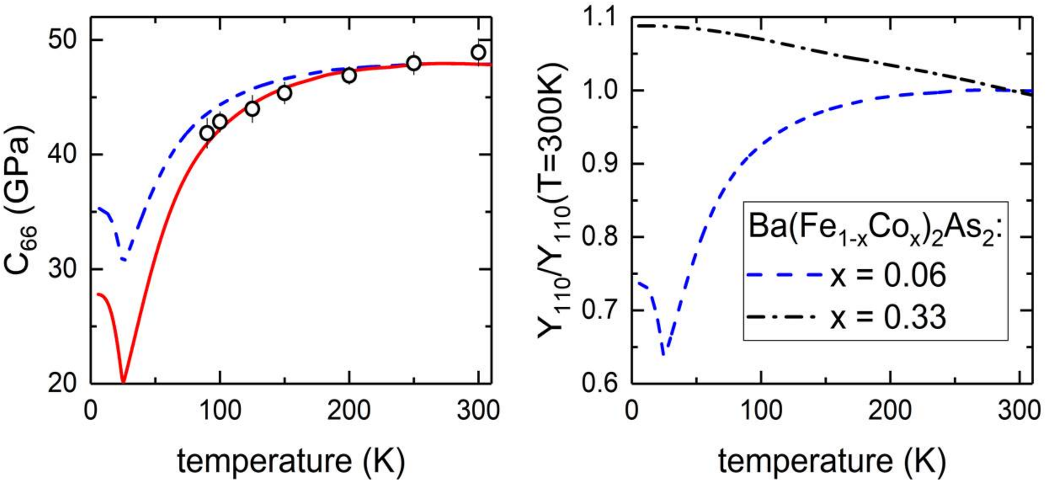

Figure 4.16: (a) Temperature dependence of C_{66} as deduced from linear fits to INS data for $T \geq 90\,\mathrm{K}$. The dashed line represents the reported T dependence of Young's modulus $Y_{[110]}/Y_{[110]}(T = 300\,\mathrm{K})$ [99] scaled to fit the high temperature value of 47.9 GPa observed in linear fits to our INS data for $T \geq 200\,\mathrm{K}$. The solid line represents the T dependence of $Y_{[110]}$ but scaled to fit the T dependence of $C_{66}(T)$ deduced from linear fits, i.e. using $\xi = 0$, to the neutron data in the temperature range $T \geq 90\,\mathrm{K}$ (open black circles). (b) Young's modulus normalized to its value at $T = 300\,\mathrm{K}$ from three-point bending experiments for $Ba(Fe_{1-x}Co_x)_2As_2$ with $x = 0.06$ (blue dashed line) and $x = 0.33$ (black dash-dotted line). [115]

line in figure 4.16(a) which are in accordance to the rescaled values of $C_{66}(T)$. It has to be remarked that the high temperature value of $C_{66} = 47.9\,\mathrm{GPa}$ based on the INS data is significantly higher than the value measured by Yoshizawa *et al.* [103] $C_{66} \approx 38\,\mathrm{GPa}$. This mismatch might be explained by the difference in the experimental method. During the ultrasound experiments the sample needs to put under certain stress and the sample orientation is not as exact as for INS. The phonon dispersion $E(\mathbf{q})$ (see Fig. 4.17) were measured prior to this work with inelastic neutron scattering using the triple-axis spectrometers 4F2 and 1T at the Laboratoire Léon Brillouin. All measurements were done in the [100]-[010] scattering plane on a 1 g single crystal of $Ba(Fe_{1-x}Co_x)_2As_2$ with $x = 0.06$ and a superconducting transition temperature of $T_c = 25\,\mathrm{K}$. The doping value was determined by energy-dispersive x-ray spectroscopy and single-crystal x-ray diffraction [116]. The data were analyzed within this thesis using the model described above. Figure 4.17 shows the resulting fits of Equation 4.8. For high temperatures $T \geq 90\,\mathrm{K}$ [250 K and 100 K, Figs. 4.17(a) and (b)] the experimental dispersion is linear within the experimental uncertainty, indicating a correlation length smaller than $\xi \leq 10\,\text{Å}$. Linear fits to this data (assuming $\xi = 0$) were used to determine the linear coefficient C_{66} and are shown as circles in the inset of figure 4.18. For lower temperatures the described non-linearity of the phonon dispersion can be observed (see Figs. 4.17(c) and (d), solid line), especially when compared to the linearly extrapolated dispersions based on the coefficients C_{66}^0 (dotted lines) and C_{66} (dashed lines) which constrain our fits taken from three-point bending experiments [99].

Figure 4.17 shows selected results when the nematic correlation length ξ is treated as a free parameter. The temperature dependence of the correlation length $\xi(T)$ (see Fig. 4.18) deduced from those fits shows a sharp peak with a maximum at T_c. The decrease of ξ below the transition temperature promotes the observed phonon softening at finite momenta measured by INS, emerging from the non-linearity of the phonon dispersion. The strong increase of the non-linear term in the dispersion relation causes the weak temperature dependence of the phonon for $T_c \leq T \leq 70\,\text{K}$ described earlier (see Fig. 4.11).

At $T = 250\,\text{K}$ the dispersion is described by a straight line [Fig. 4.17(a)]. That means that the sample exhibits normal behavior without nematic fluctuations at this high temperature limit.

The measurement at $T = 100\,\text{K}$ is the upper limit for the definition of the nematic correlation length. For higher temperatures the nematic correlation length is shorter than $\xi < 10\,\text{Å}$ for $T > 100\,\text{K}$. The data points were taken in a momentum range of $0.04 \leq K \leq 0.12$ which corresponds to a correlation length of roughly $100\,\text{Å} \geq \xi \geq 30\,\text{Å}$, so the curvature of the dispersion can not be seen. To measure a nematic correlation length of $\xi \leq 10\,\text{Å}$ and below the measurement should be done as far out as $K = 0.4$. For $T = 100\,\text{K}$ [see Fig. 4.17(b)] the dispersion fitted to the experimental data looks like a straight line and the point where the dispersion goes back to C_{66}^0 is out of the range of this experiment. Here it is still possible with the fit function to get a reasonable value for ξ. For higher temperatures and smaller ξ this is not possible anymore with the current data set (gray area in Fig 4.18).

Figure 4.17(c) shows a measurement done at a temperature $T = 28\,\text{K}$ very close to T_c. Here the data from INS and three-point bending show the biggest deviation (see Fig. 4.11). The dispersion at this temperature shows the strongest curvature which results in the biggest nematic correlation length. The larger ξ becomes the harder the effects are to measure. The deviations are then only measurable at very small $\mathbf{q}$ which limits the possibility to determine and analyze the nematic correlation length analogous to the lower limit.

In the temperature range below the superconducting transition temperature $T < T_c$ Figure 4.11 suggests that the deviation between the two techniques is strongest. Figure 4.17(d) indeed displays that the curvature is getting smaller and the different results approach each other. It has to be mentioned that it is not necessary in Figure 4.11 that the INS data and the scaled three-boint bending measurements are compatible at base temperature. The only restriction is that the INS data can not be lower than the value of C_{66} based on three-point bending.

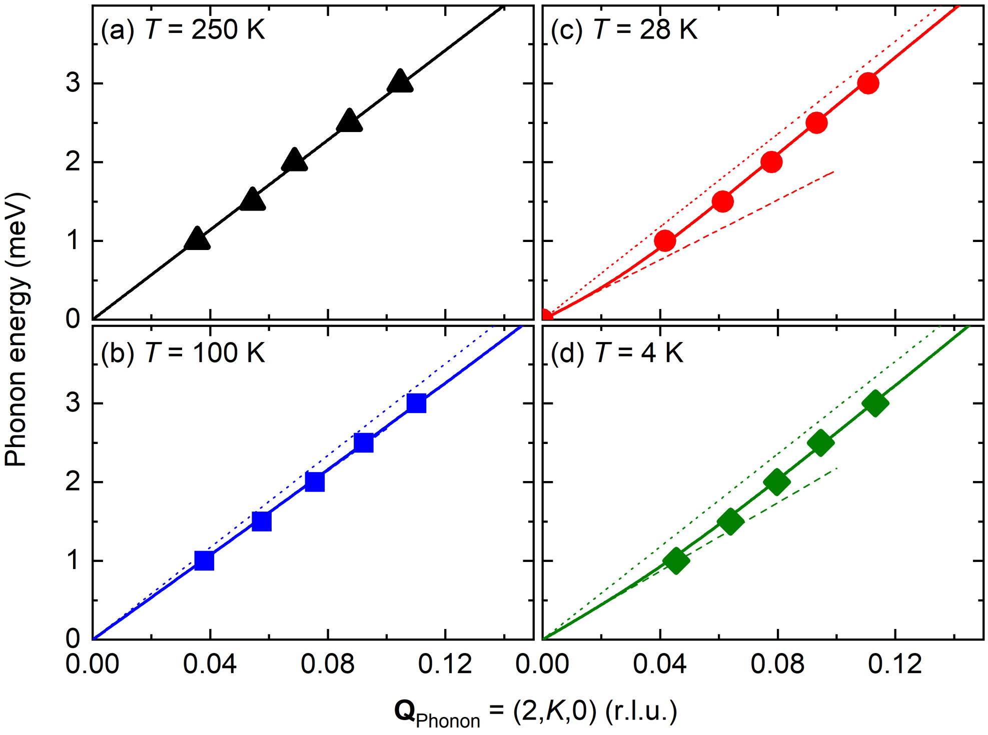

Figure 4.17: Analysis of the observed phonon dispersion (symbols) using Equation 4.5 (solid lines) at four different temperatures: two well above ($T = 250\,\mathrm{K}$, $100\,\mathrm{K}$), one close to ($T = 28\,\mathrm{K}$), and one well below $T_c = 25\,\mathrm{K}$ ($T = 4\,\mathrm{K}$). Dashed lines represent the linear component of the approximated dispersions at $\mathbf{q} = 0$ ($E_{\mathrm{lin}}(\mathbf{q} \approx 0) = \sqrt{C_{66}(T) \cdot q^2/\rho}$, visible only for $T \leq 28\,\mathrm{K}$). Dotted lines represent the linear component of the estimated dispersion in the absence of nematic fluctuations ($E_{\mathrm{linear}}(q \gg 0) = \sqrt{C^0_{66}(T) \cdot q^2 \rho^2}$). Error bars in K of the experimental data are smaller than the symbol size. [115]

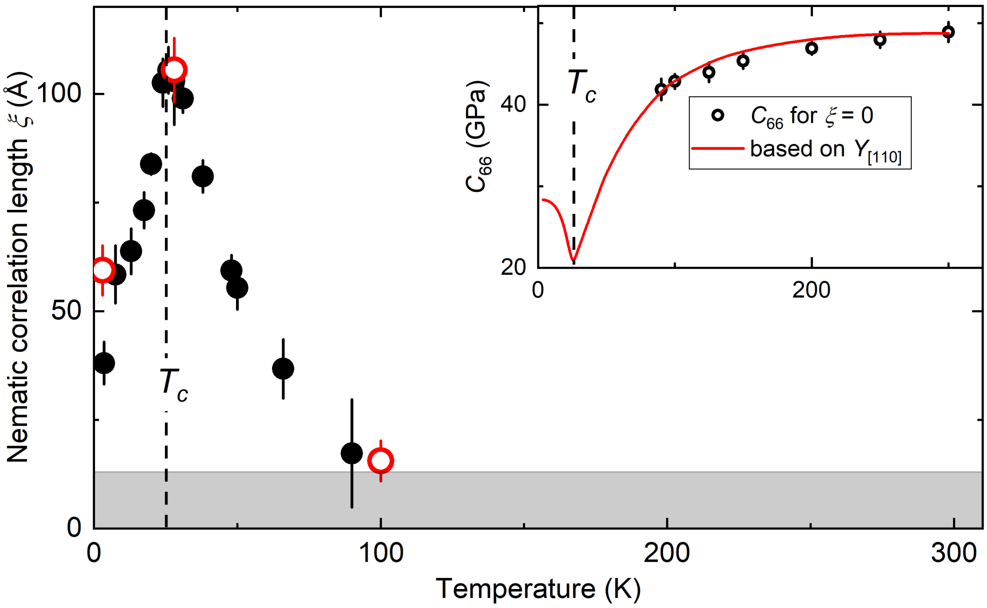

Figure 4.18: Temperature dependence of the nematic correlation length ξ deduced from the fits shown in figure 4.17 (red circles). The full black dots represent the results from the analysis with only three data points, i.e. taken at constant energies of $E = 1.9\,\text{meV}$, $1.5\,\text{meV}$ and $2.5\,\text{meV}$. The gray are indicates the limit below which we can not resolve ξ anymore. The inset shows $C_{66}(T)$ (circles) deduced from linear fits ($\xi = 0$) to the phonon dispersion data for $T \geq 90\,\text{K}$ (circles are the same as in inset of figure 4.16). The red line was obtained by scaling the reported behavior of Young's modulus $Y_{[110]}$ [99] to these measurements (same as in inset of Fig. 4.16).[115]

In general the analysis above can be applied to other structural phase transitions with an ordering vector $\mathbf{q}$=0, i.e. the structural phase transition in Nb$_3$Sn (see Chapter 4.1.2).

In the spin driven nematic scenario the nematic fluctuations are closely connected to magnetic fluctuations. Moreover the nematic correlation length ξ is coupled to the magnetic correlation length ξ_{AFM}, if one increases (decreases) so does the other. Following Karahasanovic *et al.* [117] J. Schmalian expressed this relation by:

$$\begin{aligned} \xi^2 &\propto \xi_{\text{AFM}}^{6-d} \qquad \text{for} \qquad |\mathbf{q}| \gg \xi_{\text{AFM}}^{-1} \\ \xi^2 &\propto \xi_{\text{AFM}}^{d-2} \qquad \text{for} \qquad |\mathbf{q}| \ll \xi_{\text{AFM}}^{-1} \end{aligned} \tag{4.10}$$

The well known phase competition between magnetism and superconductivity will naturally reduce the magnetic correlation length and due to the Equations 4.10 will also reduce the nematic correlation length on cooling below T_c. With this effect the sharp maximum of the nematic correlation length ξ shown in figure 4.18 and the strongest curvature of the experimental dispersion at T_c both can be explained as being due to the competition between nematic/magnetic fluctuations and superconductivity. Furthermore it resolves the obvious discrepancy between the phonon renormalization and the behavior of $C_{66}(0)$ in the superconducting state (see Fig. 4.11).

4.3.3 Phonon lifetime measurements on the three axes spin echo spectrometer (TRISP)

Although the INS data from 1T looks quite convincing, the spurious signal in the energy scans might lead to questioning the reliability of the phonon linewidth data. Therefore the very same sample was used for another measurement on the three axes spin echo spectrometer (TRISP) to dispel any doubts of the temperature dependence of the phonon linewidth.

As described in chapter 2.5 the high resolution neutron spectrometer TRISP combines triple axes (TAS) and neutron resonance spin echo (NRSE) techniques. For the measurements on TRISP the 4 g $Ba(Fe_{0.94}Co_{0.06})_2As_2$ sample was mounted in the [1 0 0]-[0 1 0] scattering plane. The actual linewidth measurements were carried out at a fixed final energy of $E_f = 12.927\,\text{meV}$. The mosaicity measured using Larmor-diffraction [118] is 0.095 ° at room temperature and increases on cooling towards T_c and decreases again on further cooling below T_c (Fig. 4.19). This behavior indicates the incipient structural phase transition of the sample. Even with an absent phase transition local orthorhombic fluctuations were observed in iron-based superconductors (for further discussion see Chapter 4.4.1). The small mosaicity underlines the excellent quality of the used sample. The effect of the temperature dependent mosaicity was taken into account in the analysis of the phonon linewidth data since it leads to a broadening of the Bragg peaks which affects the resolution of the phonon linewidth measurement. Overall the effect is quite small ($\approx 10\,\mu\text{eV}$) and does not alter the values obtained on TRISP significantly. For measuring the phonon life time, which corresponds to the phonon linewidth, for the particular phonon mode the triple axis spectrometer had to be set to fixed values for the wave vector $\mathbf{Q} = (2,\, 0.08,\, 0)$ and the energy $E = 1.7\,\text{meV}$ which were obtained in a regular triple axis scan at $T = 26\,\text{K}$ (see Fig. 2.8 in Chapter 2.5). These conditions were kept during all of the spin-echo scans. Apart from using full polarization analysis and the concomitant reduced neutron flux for the data acquisition on TRISP described in detail in Chapter 2.5 at least four (in our case even more) different spin-echo times are needed to get a reliable polarization analysis which is really costly in terms of neutron beam time. These so called *frequency scans* were done for ten temperatures over the whole temperature range ($3\,\text{K} \leq T \leq 300\,\text{K}$) and took from 7 hours ($T = 300\,\text{K}$) up to 21 hours ($T = 3\,\text{K}$) because the phonon in-

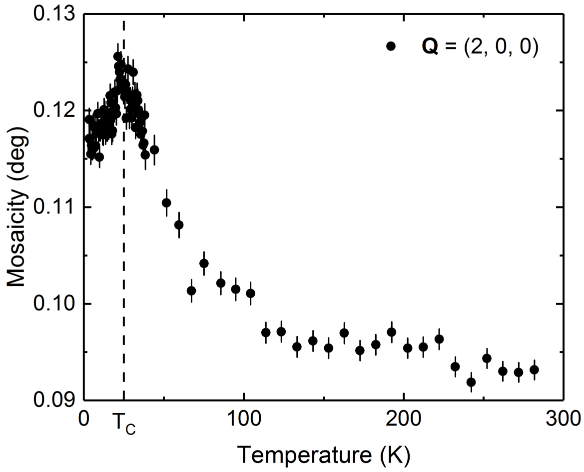

Figure 4.19: Mosaicity (in degrees) sample as a function of the temperature (in K). It slightly increases on cooling towards T_c and decreases on further cooling below T_c.

tensity decreases rapidly with the Bose factor at low temperatures. A faster but less accurate method is the so-called *temperature scans*. For this type of measurements the spin-echo time is kept fixed. Hence for each temperature there is only one value of the polarization and an extrapolation to other spin-echo times is needed to determine the phonon linewidth. It is important to choose a suitable spin-echo time. The measured polarization for the selected τ needs to strongly depend on the spin-echo time. Hence, it is important to know the scale of the phonon linewidth in advance. Comparing both data sets both methods of collecting data are in good agreement with each other [see Fig. 4.20 for a comparison of temperature scans (black) and frequency scans (red)].

During the analysis of data with MATLAB several effects on the raw data had to be taken into account and several corrections had to be made. Besides estimating a reasonable background the particular mosaicity for each temperature was used in the analysis for all the frequency scans to get rid of the effects due to different mosaic spreads. These effects were really small although a slight difference in the corrected data can be observed ($\approx 10\,\mu$eV). Furthermore for the polarization fits P_0 was kept constant (= 1) by explicitly assuming that the peak shape is Lorentzian.

The raw data can also be used to calculate the energy shift of the phonon peak normalized to base temperature [$\Delta E(3.4\,\mathrm{K}) = 0$ with $E = 1.7\,\mathrm{meV}$]. When measuring the intensity oscillations to determine the polarization the period length depends on the phonon energy [see Fig. 2.8(b) in Chapter 2.5]. A change of the phonon energy leads to a different final energy of the neutron and in turn to a change of the time for

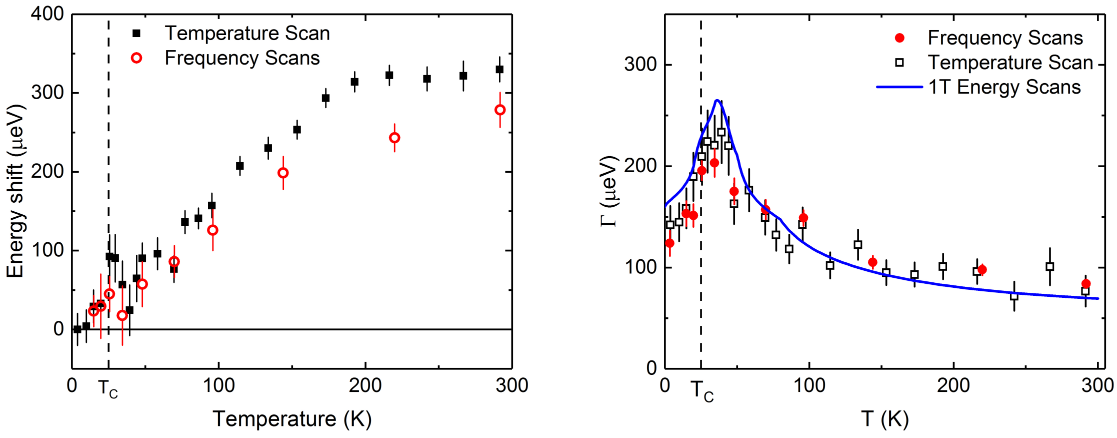

(a) Energy shift (b) linewidth

Figure 4.20: Results from TRISP. (a) Energy shift of the phonon normalized to the low temperature value at $T = 3.4\,\mathrm{K}$ with $E = 1.7\,\mathrm{meV}$. The black squares show the data from the temperature scans and the red circles the data from the frequency scans. (b) Phonon linewidth (in μeV) over the sample temperature (in Kelvin) of the frequency scans (red closed dots) and the temperature scans (black open squares) compared to the results from the INS energy scans measured at 1T (blue line).

passing the second magnetic field section (of which the length is scanned here). Figure 4.20(a) shows the temperature evolution of this energy shift (not absolute energy values). On cooling the energy decreases towards T_c, stays more or less constant around this value and decreases below that temperature. The maximum of the energy shift from $T = 300\,\mathrm{K}$ to base temperature is about $\Delta E(300\,\mathrm{K} - 3\,\mathrm{K}) \approx 300\,\mu\mathrm{eV}$, which is consistent with the measurements on 1T [see Fig. 4.14(a)]. Nevertheless the main interest of this experiment was to gain information about the phonon linewidth and, thus, about the phonon life time. In figure 4.20(b) the temperature dependence of the phonon linewidth extracted from temperature scans (black), frequency scans (red) and 1T energy scans are displayed. All three data sets are in reasonable agreement to each other. The linewidth stays more or less constant on cooling from 300 K to 100 K at $\Gamma \approx 100\,\mu\mathrm{eV}$. On further cooling the linewidth increases to about $\Gamma \approx 200\,\mu\mathrm{eV}$ and , in fact, shows only little to no temperature dependence (within the experimental error) in the range $40\,\mathrm{K} \geq T \geq T_c = 25\,\mathrm{K}$ before decreasing again for temperatures below T_c.

The phonon lifetime measurements on TRISP could be of great importance for the further discussion of superconductivity in iron-based superconductors. The results present the very first data that show a significant change of the phonon linewidth, e.g. the phonon lifetime. This is the first evidence of a damping mechanism similar to conventional superconductors, e.g. electron-phonon coupling.

4.3.4 Inelastic x-ray scattering measurements at the APS and at SPring-8

Inelastic x-ray measurements at sector 30 at the APS

The IXS measurements in hole-doped materials below (see Chapter 4.3.5) show a different behavior than we observed via INS in Co-Ba122. Hence, we wanted to verify that we indeed find the same results for Co-Ba122 using IXS. Therefore we went with a 6 % doped sample to the high energy-resolution x-ray (HERIX) spectrometer at the inelastic beam line Sector 30 at the Advanced Photon Source (APS) at the Argonne National Lab (ANL) in the United States of America (see chapter 2.4). To study the phonon behavior we performed constant **Q** scans. We always measured the phonon at positive and negative energy transfers, i.e., the Stokes and anti-Stokes lines, in a single scan. To minimize effects of misalignment we took data on both sides of the Bragg peak as well [e.g. $\mathbf{Q} = (4, 0.075, 0)$ and $\mathbf{Q} = (4, -0.075, 0)$] [see Fig. 4.21(a)]. Another issue we faced was the stability of the energy at the monochromator and the analyzers. The temperature of both the monochromator and the analyzers has to be held as constant as possible during the experiment. For example a change of $\Delta T = 0.1\,\mathrm{K}$ at the monochromator leads to a change of about $\Delta E \approx 10\,\mathrm{meV}$ in the selected energy. There are future plans to place the monochromator in a vacuum to improve the temperature control and thus the stability of the energy. To reduce the effects of energy drift we decided to perform scans for each **Q** value (positive and negative, so six scans in total) and each temperature instead of one long scan. The six scans where then combined to one scan for each temperature before fitting. We also checked for some temperatures if there is a difference for fitting the different **Q** values on the different sides of the (4 0 0) Bragg reflection. separately and then calculating the mean value of these two fits instead of combining both sides before fitting. The difference compared to the method we chose was small than the typical error bars, so it is legitimate to add up all six scans before fitting. To enhance the readability in the following the given wave vectors $\mathbf{Q} = (4, K, 0)$ for the experiments at the APS always also include both sides of the Bragg peak at $\pm K$. To fit the combined scans for each temperature we used a fit function consisting of three different parts: a straight line (background), a pseudo-Voigt function (elastic line) and a damped harmonic oscillator (DHO) convoluted with the experimental resolution (phonon) [see Fig. 4.21(b)].

The resulting temperature dependence of the phonon energy and the phonon linewidth are shown in Figure 4.22. The phonon energy decreases on cooling towards the superconducting transition temperature. Around T_c it stays more or less constant before another slide hardening below can be observed. This behavior is in good agreement to

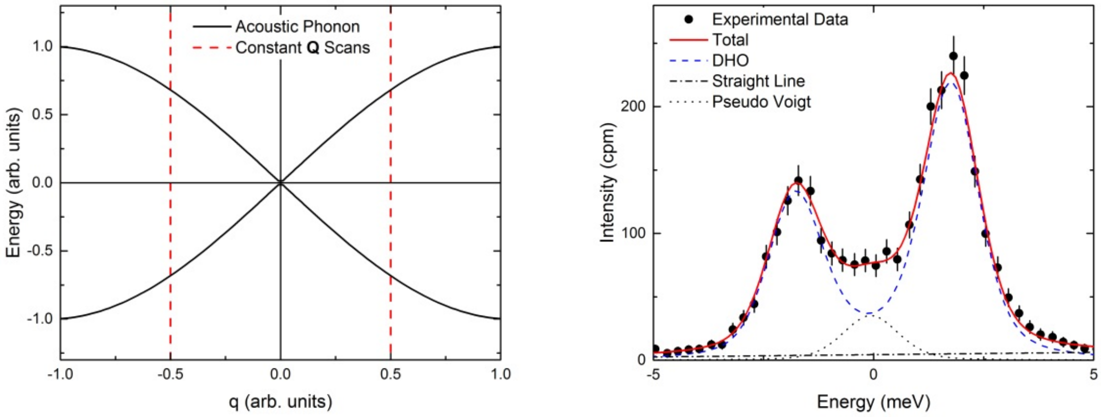

(a) Constant **Q** scans

(b) Fitting routine

Figure 4.21: (a) Schematic picture of the dispersion of an acoustic phonon (black) and the performed constant **Q** scans (red). The scans were done for both negative and positive values. The scans also covered the positive and negative energy range. (b) Experimental data (black dots) of $Ba_{1-x}Na_xFe_2As_2$ for $\mathbf{Q} = (4, 0.075, 0)$ and $T = 40\,\mathrm{K}$. The fit function (red solid line) consists of three different contributions: a damped harmonic oscillator (DHO) convoluted with the experimental resolution to fit the Stokes and anti-Stokes part of the phonon (blue dashed line), a straight line to fit the background (black dashed-dotted line) and a pseudo-Voigt function to take elastic scattering into account (black dotted line).

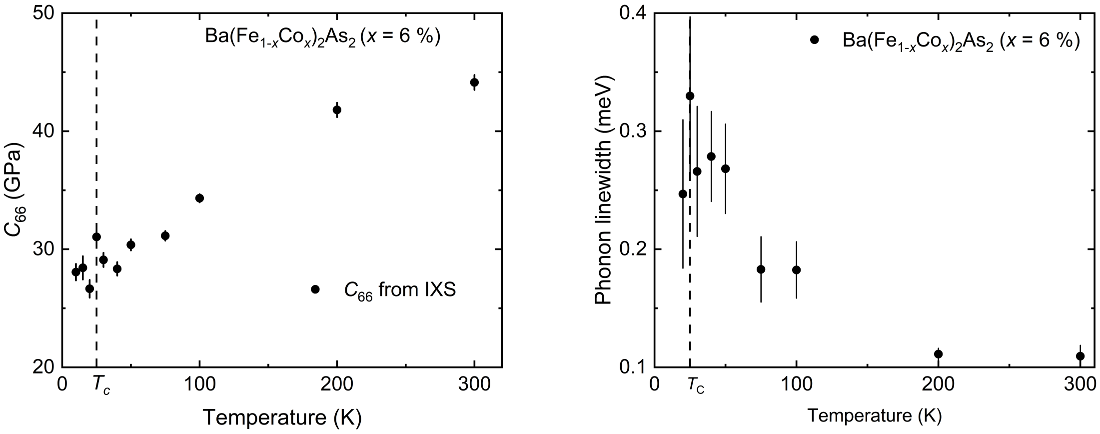

(a) Phonon energy (b) Phonon linewidth

Figure 4.22: (a) Phonon energy of Ba(Fe$_{0.94}$Co$_{0.06}$)$_2$As$_2$ (black dots) derived from inelastic neutron scattering. The energy scans where taken at the wave vector $\mathbf{Q} = (4, 0.075, 0)$. To fit the data a DHO function was used and if necessary a pseudo-Voigt function for the elastic line. (b) The phonon linewidth increases on cooling towards T_c. Below the transition temperature the both the energy and the linewidth could not be resolved properly.

the results from the energy scans with INS at 1T [see Fig. 4.14(a)]. The phonon linewidth increases clearly on cooling with its maximum at T_c. This confirms qualitatively the results from INS and NRSE measurements [see Fig. 4.20(b)].

Dispersion measurements at SPring-8

The inelastic x-ray spectrometer at SPring-8 in Japan offers a special setup of analyzers which allows to measure up to four different wave vector positions of the TA phonon dispersion in Co-Ba122 simultaneously and, thus, speed up the measurements tremendously. The two dimensional analyzer array that is used at the sepectrometer allows to parallelize data collection [15] and is a way more efficient method to measure a dispersion. Figure 4.23 shows a picture of the grid of different analyzers. In general it is only possible to put one analyzer precisely to a high symmetry point. However, it is possible that various analyzers are in the vicinity of the symmetry direction (4.23). A horizontal line of analyzers in the scattering plane is arranged nearly along the symmetry for a longitudinal phonon mode and a vertical line on the symmetry direction for a transverse mode. This analyzer geometry can help measuring the transverse dispersion along $\mathbf{Q}$ = (4, K, 0) by using four analyzers in the vertical line at once to gather data for four different K values simultaneously.

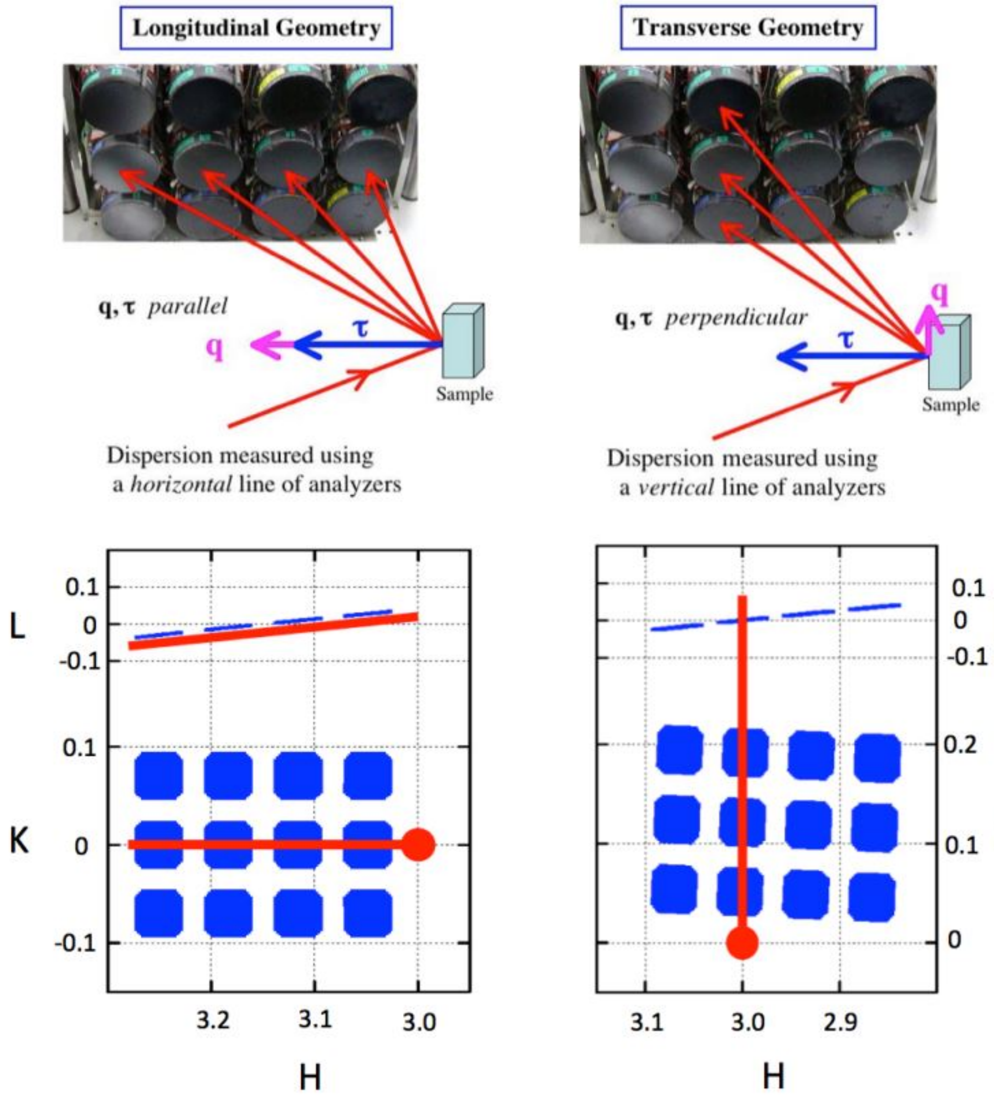

Figure 4.23: A two dimensional analyzer array can be used to parallelize measurements of longitudinal (left) and transverse phonons (right). In each case the top panel shows a schematic while the lower panel shows an exact calculation for a specific array and material. [15]

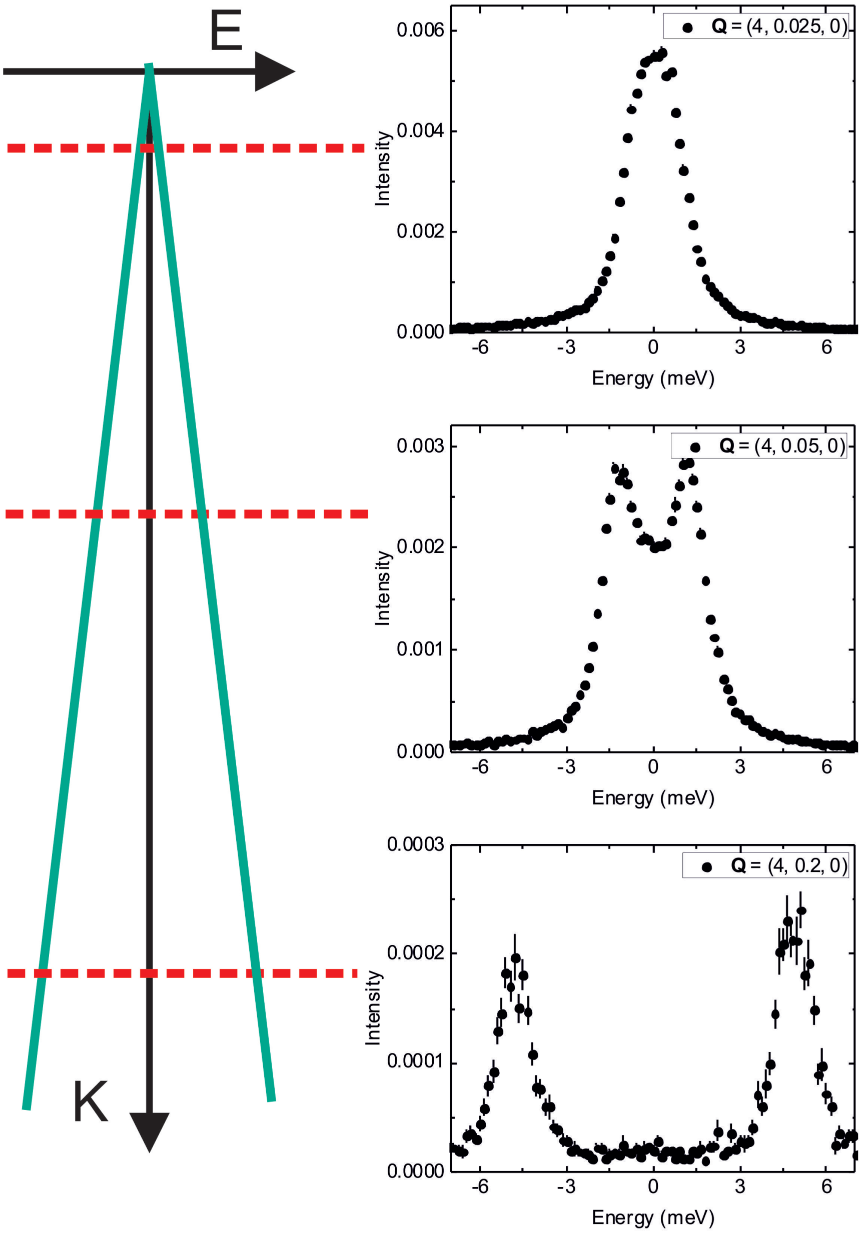

Figure 4.24: Inelastic x-ray scattering raw data taken at different K values. The energy scans where taken at the wave vectors (from left to right) $\mathbf{Q} = (4, 0.2, 0)$, $\mathbf{Q} = (4, 0.05, 0)$ and $\mathbf{Q} = (4, 0.025, 0)$. To fit the data a DHO function was used and if necessary a pseudo-Voigt function for the elastic line. For decreasing K the Stokes and Anti-Stokes parts of the phonon scattering are shifted more and more towards zero.

To fit the raw data of the energy scans (see Fig. 4.24) a combination of convoluted damped harmonic oscillator function (phonons) and if necessary a pseudo-Voigt function (elastic line) was used. With decreasing values of K the peaks from creation and annihilation of phonons (Stokes and anti-Stokes) approayh each other and tend towards zero.

For $K \geq 0.05$ the data could be fitted relatively easy and with a convincing result. At smaller wave vectors the two phonon peaks cannot be resolved anymore due to the finite energy resolution of about 1.3 meV of the spectrometer. Since this introduces an uncertainty in the fitting parameters we decided to neglect these data and will only present results down to $K = 0.05$ r.l.u..

Figure 4.25 shows the fits according to the model explained in Chapter 4.2 to the experimental dispersion data. The dashed lines represent the bare elastic modulus C_{66}^0 without nematicity. For high temperatures ($T = 290$ K, green triangles) the fit of dispersion is equivalent with C_{66}^0. The dispersion shows no curvature, e.g. the nematic correlation length ξ is very small and below the resolution limit. For the other temperatures a clear curvature of the phonon dispersion can be observed and the theoretical model is used to determine finite values for ξ (Fig. 4.26). Due to the larger K range, compared to previous measurements, the point where the dispersion becomes linear again can be seen in the experimental data. The values for the nematic correlation length ξ determined from the fits of the phonon dispersion of the inelastic scattering data can be compared to the previous data from INS (Fig. 4.26). The IXS data (red triangles) has a different y-scale than the INS data (black dots). The absolute values are smaller for IXS ($\xi_{max} \approx 60$ Å)than for INS ($\xi_{max} \approx 100$ Å) and might give a more advanced value for the upper limit of the nematic correlation length. The overall behavior is very similar for both experiments. Both data sets have their maximum at T_c.

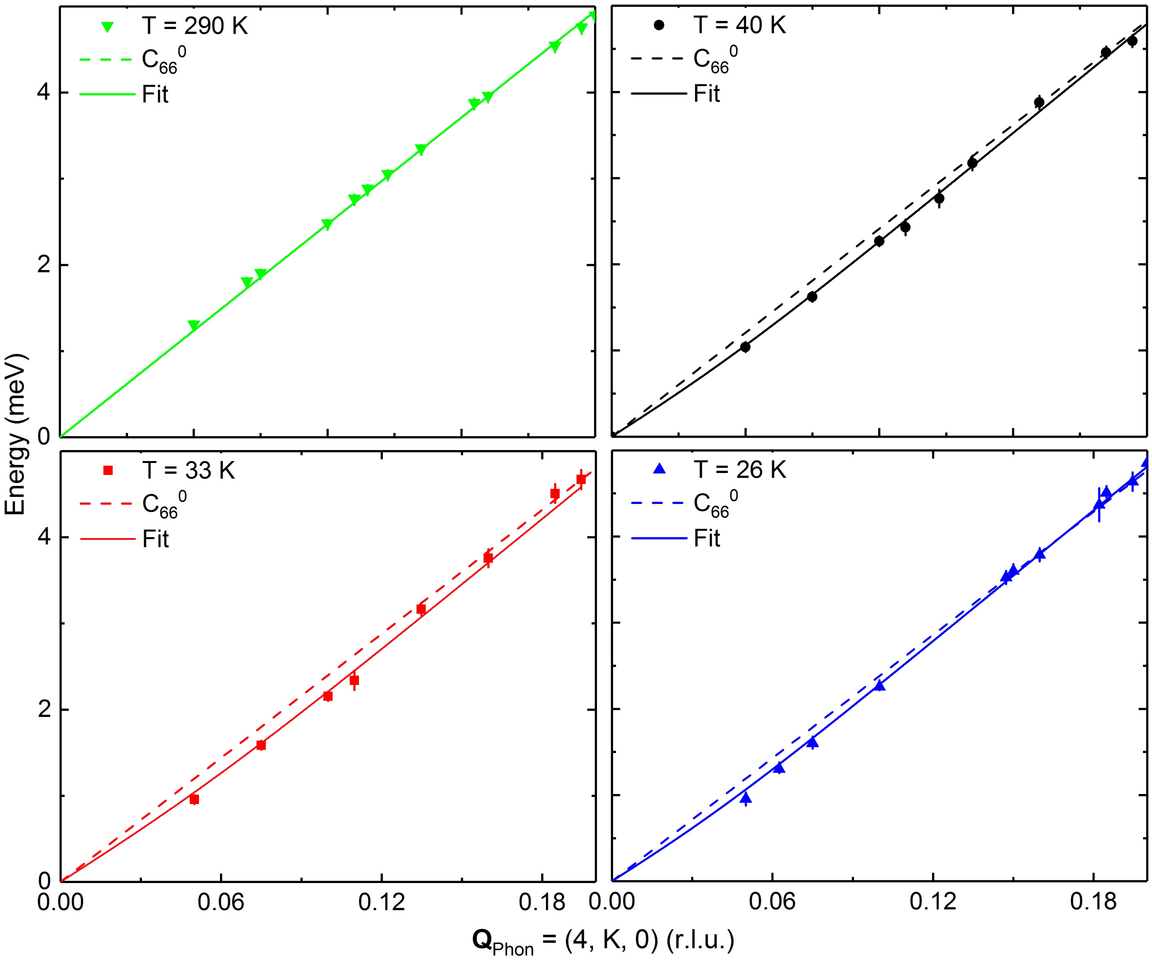

Figure 4.25: Analysis of the observed phonon dispersion (symbols) using Equation 4.5 (solid lines) at four different temperatures: one well above ($T = 290\,\mathrm{K}$) and three close to ($T = 40\,\mathrm{K}$, $T = 33\,\mathrm{K}$, $T = 26\,\mathrm{K}$) $T_c = 25\,\mathrm{K}$. Dotted lines represent C_{66}^{0} determined from the x-ray data at $T = 290\,\mathrm{K}$.

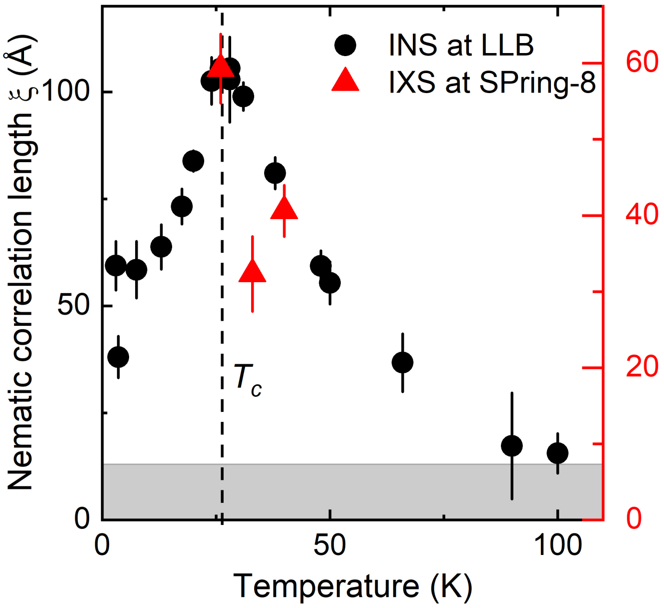

Figure 4.26: Phonon dispersions from inelastic x-ray scattering at $\mathbf{Q}_{\mathrm{Phon}} = (4, K, 0)$. The fits (solid lines) were done according to the theoretical model explained in Chapter 4.2. The dashed lines represent the bare elastic modulus C^0_{66} without nematicity.

4.3.5 Hole-doped samples

In $BaFe_2As_2$ it is not only possible to study electron doped samples, for example with Co [119] on the Fe site. Other substitutions studied in this thesis are hole doping with K [93], Na on the Ba site and additionally Na on the Sr site in $SrFe_2As_2$ (see Fig. 4.5). The original intention of this work was to investigate the temperature dependence of the phonon energy of those other members of the 122 family for both underdoped samples with a full structural phase transition and optimally doped samples exhibiting only a superconducting phase transition along with precursor effects of the suppressed nematic/structural phase transition. In the following the experimental data of the inelastic x-ray measurements of several samples of $Ba_{1-x}K_xFe_2As_2$, $Ba_{1-x}Na_xFe_2As_2$ and $Sr_{0.67}Na_{0.33}Fe_2As_2$ will be displayed, starting with $Sr_{0.67}Na_{0.33}Fe_2As_2$.

4.3.5.1 $Sr_{0.67}Na_{0.33}Fe_2As_2$

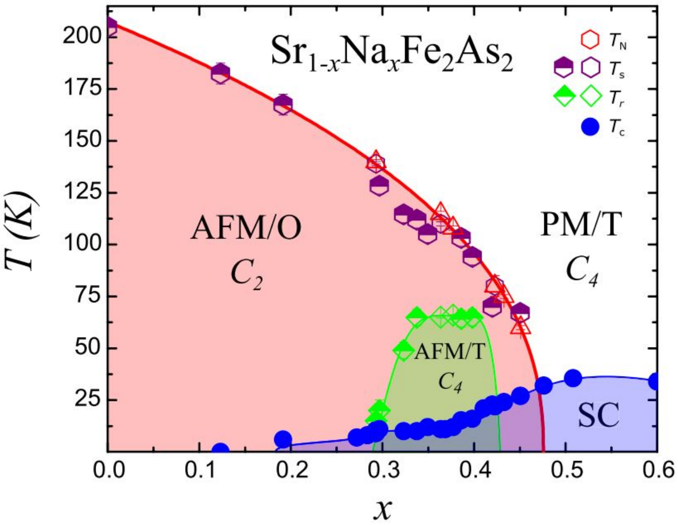

Figure 4.27: Phase diagram of $Sr_{1-x}Na_xFe_2As_2$. Displayed are the paramagnetic/tetragonal (PM/T, white), antiferromagnetic/orthorhombic (AFM/O, red), antiferromagnetic/tetragonal (AFM/T, green) and superconducting phase (SC, blue). [120]

In advance, all samples used for inelastic x-ray measurements at the APS where characterized via thermal expansion by C. Meingast and L. Wang from our institute[1]. The underdoped $Sr_{0.67}Na_{0.33}Fe_2As_2$ sample we were using shows two structural phase transitions on cooling (see Fig. 4.27), from tetragonal to orthorhombic ($T_{s1} \approx 122\,\mathrm{K}$) and back to tetragonal ($T_{s2} \approx 50\,\mathrm{K}$). The second tetragonal phase (green area in Fig. 4.27) is the C_4 phase which is also antiferromagnetic [120, 121].

On entering the orthorhombic state the crystal lattice is twinned and exhibits four different domains [upper part of Fig. 4.28(a)]. The domain formation splits the Bragg points into three or four points, depending on the direction in momentum space. The observed tetragonal (4 0 0) Bragg peak [marked by black circle in lower part of Fig. 4.28(a)] is splitting into three different peaks. Figure 4.28(b) shows three different scans done at constant energy in $Sr_{0.67}Na_{0.33}Fe_2As_2$. The scan at $T = 130\,\mathrm{K} > T_s$ shows one single Bragg peak (red squares). On cooling below the structural transition into the orthorhombic phase the splitting of the Bragg peaks could be observed (black circles). After cooling down to the second tetragonal phase and heating up to the orthorhombic phase again we were able to measure in a single domain without any Bragg peak split-

---

[1] I want to thank Christoph Meingast and Liran Wang for the really helpful thermal expansion data.

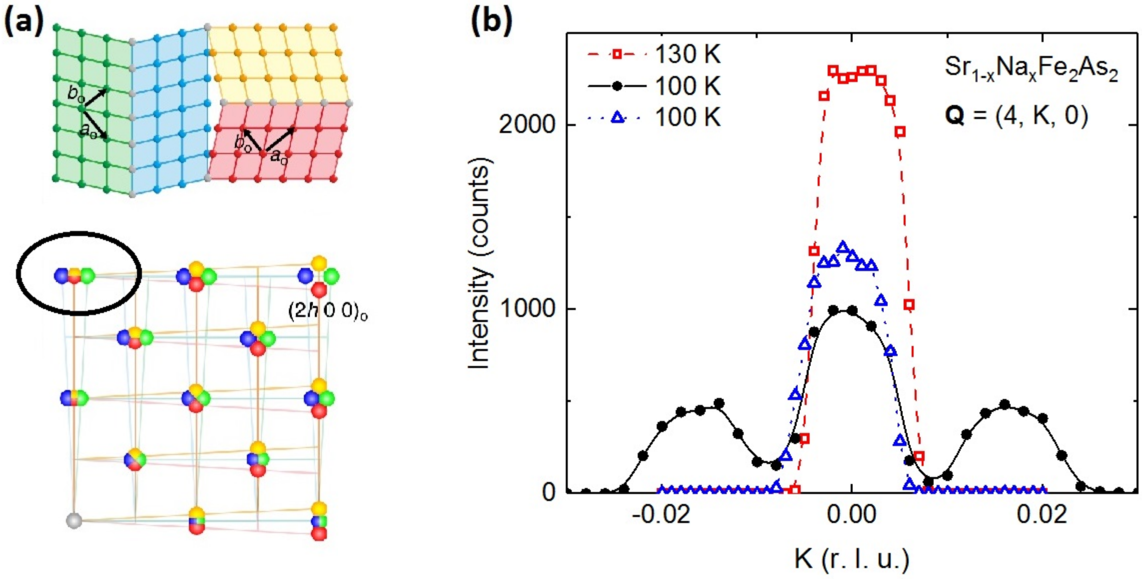

Figure 4.28: (a) Illustration of the connection of domain splitting and splitting of the Bragg peaks along different directions in momentum space [109]. The figure is based on the orthorhombic unit cell and uses the orthorhombic notation for the Bragg peaks, i.e. $(2h\,0\,0)_o$. The black circle marks the tetragonal (4 0 0) Bragg peak we are measuring and its possible splitting in three different peaks in the orthorhombic phase. (b) Constant energy scan at the $\mathbf{Q} = (4, 0, 0)$ Bragg peak along the K direction. The data taken at $T = 130\,\mathrm{K}$ in the tetragonal phase (red open squares) show one single Bragg peak. In the orthorhombic phase at $T = 100\,\mathrm{K}$ (black circles) a splitting of the Bragg peak in three single peaks can be observed. The blue triangles show the single domain data at $T = 100\,\mathrm{K}$ that was used for analysis of the phonon energy. The lines are a guide to the eye.

ting due to the small size of the incoming x-ray beam (blue triangles). As mentioned in Chapter 4.3.3 a large mosaicity and a broadening of the Bragg peak can affect the resolution of the phonon measurement. In the case of an actual splitting of the Bragg peak in the orthorhombic phase the interference between Bragg and the phonon might be too big to analyze the data. Above T_{s1} and below T_{s2} the structure is tetragonal and, hence, the phonon measurements where straight forward.

The phonon data was measured and fitted as described in the first part of Chapter 4.3.4. The fit results for the energy scans at $\mathbf{Q} = (4, 0.075, 0)$ in dependence of the sample temperature are displayed in figure 4.29 [Phonon energy in (a) and phonon linewidth in (b)]. The phonon softens on cooling towards $T_{s1} \approx 122\,\mathrm{K}$ followed by a weaker hardening towards $T_{s2} \approx 50\,\mathrm{K}$. At this temperature the phonon energy drops

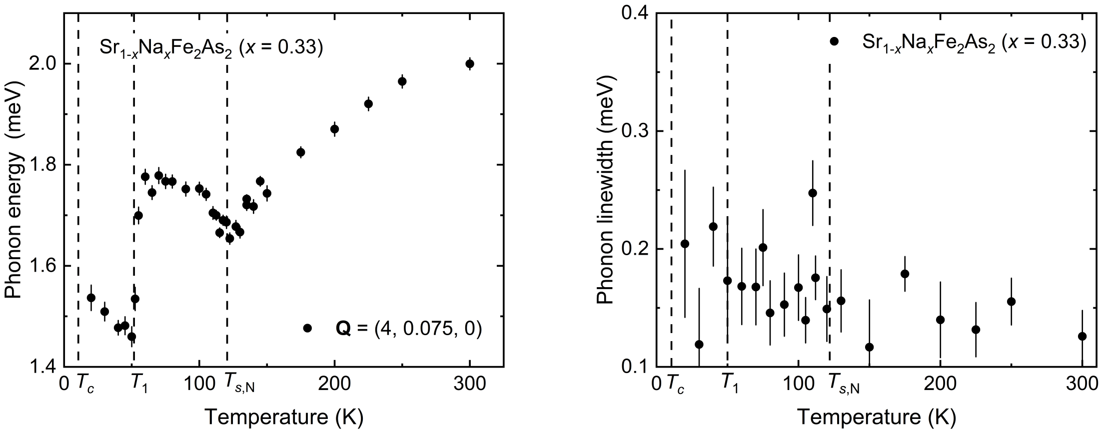

(a) C_{66}

(b) Phonon linewidth

Figure 4.29: (a) Phonon energy of $\mathrm{Sr}_{0.67}\mathrm{Na}_{0.33}\mathrm{Fe}_2\mathrm{As}_2$ as a function of the sample temperature at $\mathbf{Q}$ = (4, 0.075, 0). A softening on cooling towards $T_{s1} \approx 122\,\mathrm{K}$ can be observed, followed by a weaker hardening towards $T_{s2} \approx 50\,\mathrm{K}$. At this temperature the phonon energy drops abruptly. on further cooling a slight hardening is observed. (b) The phonon linewidth slightly increases on cooling but it shows no explicit changes near the transition temperatures.

abruptly before a slight hardening on cooling down to $T = 20\,\mathrm{K}$ takes place. We could not measure below the superconducting $T_c = 10.5\,\mathrm{K}$. For small temperatures the intensity of the anti-Stokes line is vanishing in accordance to the detailed balance principle (see Chapter 2.1). Without the anti-stokes line the position (e.g. the phonon energy) of the DHO function can not be determined unambiguously. The average of the deduced phonon linewidths seems to increase slightly on cooling but it shows no significant changes near the transition temperatures. For low temperatures the fitting of the data gets more sophisticated due to the vanishing anti-Stokes line, hence the error bars get bigger.

The phonon energy data from inelastic x-ray can be used to determine C_{66}. Since we were measuring at one single wave vector $\mathbf{Q}$ = (4, 0.075, 0) only a linear dispersion can be assumed in contrast to the model described in Chapter 4.3.2. Following Equation 4.2 from Chapter 4.3.2 for a strictis given bycan be calculated with

$$C_{66} = \left(\frac{E(\mathbf{q})^2}{q^2} \right)^2 \cdot \rho. \tag{4.11}$$

The results for this conversion are shown in Figure 4.30. In the following the results from the IXS measurements will all be shown as C_{66} to directly compare them to different measurements of Young's modulus $Y_{[110]}$.

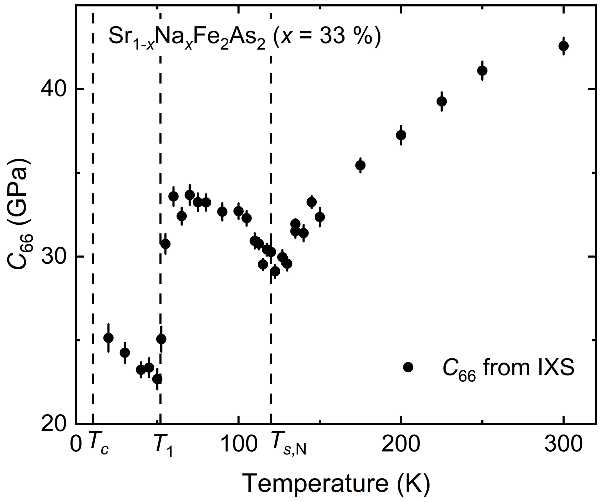

Figure 4.30: C_{66} data of $Sr_{0.67}Na_{0.33}Fe_2As_2$ as a function of the sample temperature at $\mathbf{Q} = (4,\ 0.075,\ 0)$.

4.3.5.2 $Ba_{1-x}Na_xFe_2As_2$

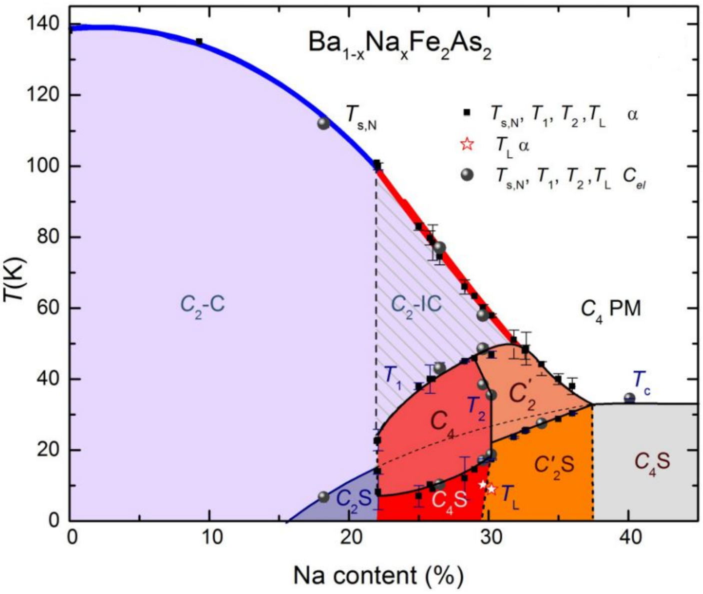

Figure 4.31: Phase diagram of $Ba_{1-x}Na_xFe_2As_2$. [122]

For Ba_{1-x}Na$_x$Fe$_2$As$_2$ we investigated two different samples, one underdoped ($x = 0.265$) and one optimally doped ($x = 0.4$). The underdoped sample becomes orthorhombic between $T_{s,\mathrm{N}} \approx 71\,\mathrm{K}$ and $T_1 \approx 45\,\mathrm{K}$ (see Fig. 4.31). In this temperature region we had the same problems with twinning and splitting of the Bragg peaks as in the Sr samples described in Chapter 4.3.5.1 but could stabilize a single domain measurement by several tries of cooling to get in and heating to get out of the orthorhombic phase and by slightly moving the beam to another spot of the sample surface. Effects connected to the superconducting transition ($T_c \approx 8\,\mathrm{K}$) could not be observed in the underdoped sample due to the vanishing anti-Stokes line as described for Sr122. In the optimally doped sample there is no structural transition but we were able to get below the superconducting transition temperature ($T_c \approx 33\,\mathrm{K}$). The phonon data for both samples was measured and fitted as described in chapter 4.3.4.

Figure 4.32 shows the results of the measurements for the underdoped sample of $\mathrm{Ba_{0.735}Na_{0.265}Fe_2As_2}$ at the wave vector $\mathbf{Q} = (4,\ 0.075,\ 0)$. A strong softening of C_{66} on cooling can be observed towards $T_{s,\mathrm{N}} \approx 71\,\mathrm{K}$ followed by a weak hardening towards $T_1 \approx 45\,\mathrm{K}$. At this temperature the phonon energy drops significantly in the range of just a few Kelvin. Below the phonon energy is constant within the error bars. The phonon linewidth essentially stays the same on cooling and it shows no explicit changes near the transition temperatures. Qualitatively , results shown in both diagrams are in good agreement with the underdoped $\mathrm{Sr_{0.67}Na_{0.33}Fe_2As_2}$ sample, except that the hardening in the orthorhombic phase of the Sr sample is a lot stronger than in the Ba sample. The blue line is deduced from measurements of Young's modulus $Y_{[110]}$ by Wang *et al.* [123]. Their results have been scaled to fit the observed maximum softening of 25 %. The reported softening was 17 %. The data was scaled in a way that high and low temperature values are in accordance to the C_{66} data.

Figure 4.32(c) shows the shear modulus C_{66} as a function of the sample temperature at $\mathbf{Q} = (4,\ 0.075,\ 0)$ in $\mathrm{Ba_{0.6}Na_{0.4}Fe_2As_2}$. A strong softening on cooling towards the superconducting transition temperature $T_c \approx 33\,\mathrm{K}$ can be observed. Below 75 K the observed phonon energies, and hence the deduced C_{66} values, stay constant within the experimental error bar. Below T_c a strong hardening occurs . In figure 4.32(d) the phonon linewidth is displayed. We cannot identify any trend within the scatter of the data.

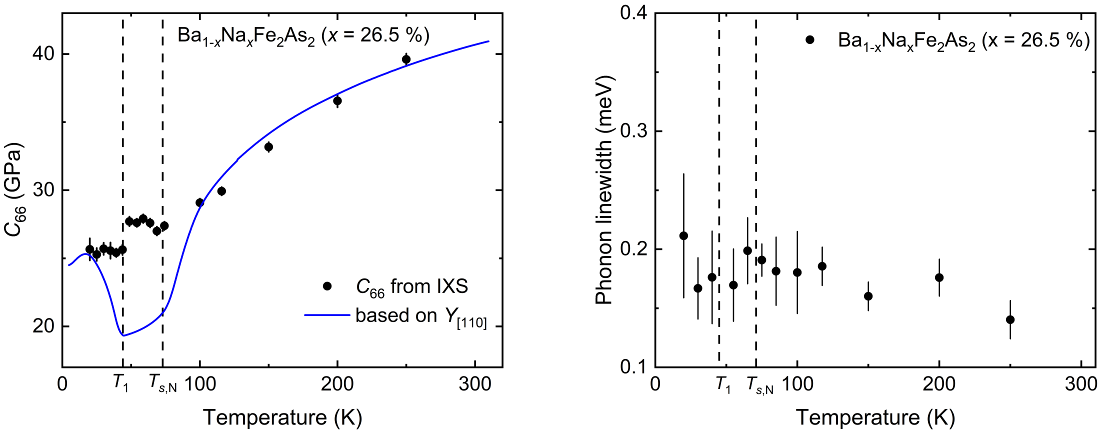

(a) C_{66} (b) Phonon linewidth

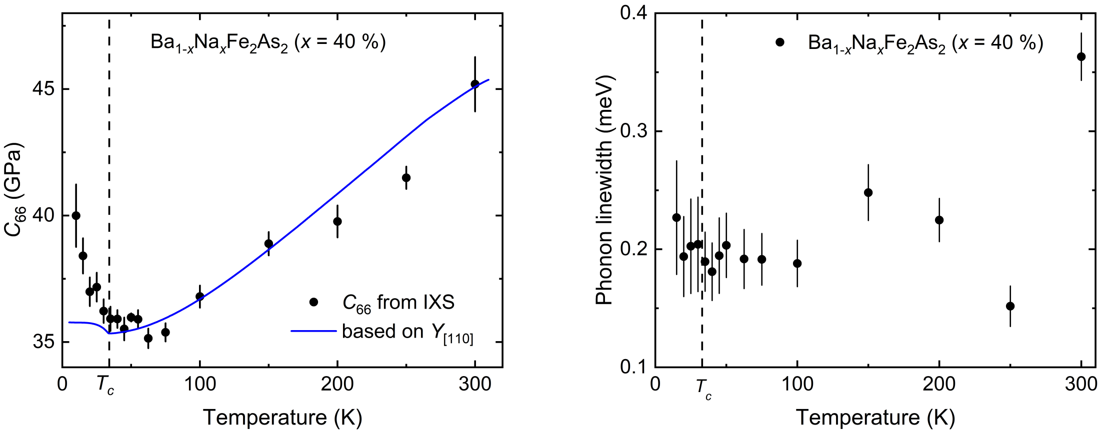

(c) C_{66} (d) Phonon linewidth

Figure 4.32: (a) Results for $C_{66}(T)$ deduced from our phonon measurements in $Ba_{0.735}Na_{0.265}Fe_2As_2$ as a function of the sample temperature at $\mathbf{Q} = (4,\ 0.075,\ 0)$. A strong softening on cooling towards $T_{s,\mathrm{N}} \approx 71\,\mathrm{K}$ can be observed, followed by a weaker hardening towards $T_1 \approx 45\,\mathrm{K}$. At this temperature the phonon energy drops significantly within a few Kelvin. Below the phonon energy is constant within the error bars. The blue line is based on data by Wang *et al.* [123]. (b) The phonon linewidth shows no explicit changes near the transition temperatures. (c) Results for $C_{66}(T)$ deduced from our phonon measurements in $Sr_{0.67}Na_{0.33}Fe_2As_2$ as a function of the sample temperature at $\mathbf{Q} = (4,\ 0.075,\ 0)$. A softening on cooling towards $T_{s1} \approx 122\,\mathrm{K}$ can be observed, followed by a weaker hardening towards $T_{s2} \approx 50\,\mathrm{K}$. At this temperature the phonon energy drops significantly. Below another hardening takes place. The blue line is based on data by Wang *et al.* [123]. (d) The phonon linewidth slightly increases on cooling but it shows no explicit changes near the transition temperatures.

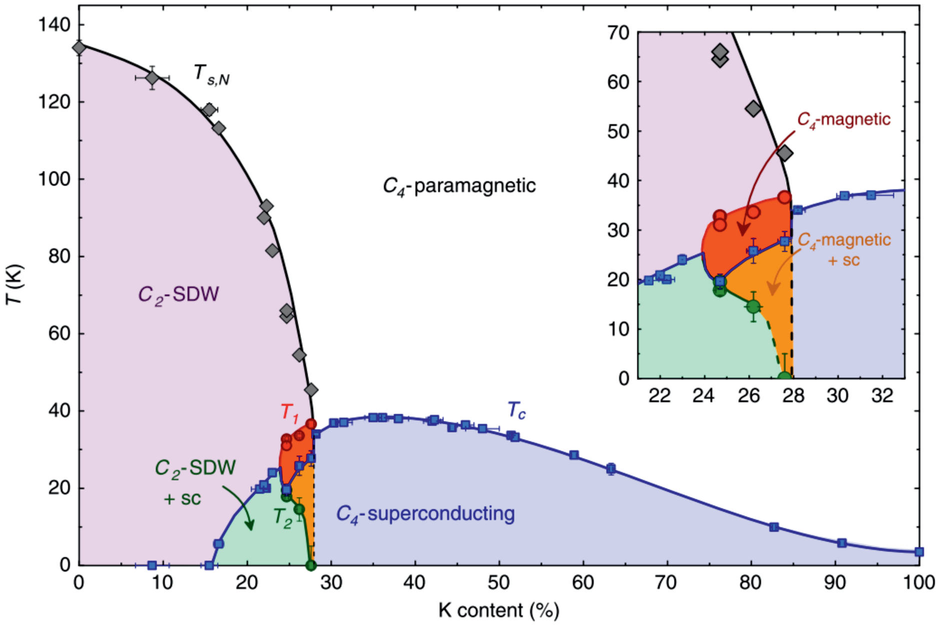

Figure 4.33: Phase diagram of $Ba_{1-x}K_xFe_2As_2$. [114]

4.3.5.3 $Ba_{1-x}K_xFe_2As_2$

For $Ba_{1-x}K_xFe_2As_2$ we investigated two different samples, one underdoped ($x = 22\%$) and one optimally doped ($x = 32.6\%$). The underdoped sample exhibits a structural phase transition from the tetragonal into the orthorhombic phase ($T_{s,\mathrm{N}} \approx 95\,\mathrm{K}$). The underdoped sample has a superconducting transition temperature $T_c \approx 24.5\,\mathrm{K}$ and the optimally doped $T_c \approx 37\,\mathrm{K}$ (see Fig. 4.33). The phonon data for both samples was measured and fitted as described in Chapter 4.3.4.

$Ba_{0.78}K_{0.22}Fe_2As_2$ exhibits a softening on cooling towards $T_{s,\mathrm{N}}$ slightly below $\approx 100\,\mathrm{K}$ [see Fig. 4.34(a)]. Below the transition a hardening of nearly the same magnitude can be observed. Within the error bars no effect at the superconducting transition temperature can be seen. The phonon linewidth below $T \leq 100\,\mathrm{K}$ is slightly bigger than at room temperature [Fig. 4.34(b)]. This behavior is reversed compared to that in $Ba_{0.6}Na_{0.4}Fe_2As_2$ but there this behavior is contradicted in between in between $100\,\mathrm{K} < T < 300\,\mathrm{K}$ [Fig 4.32(d)]. Hence, it is unclear if the increasing phonon linewidth in $Ba_{0.78}K_{0.22}Fe_2As_2$ is existing. It seems that it decreases on further cooling towards T_c.

The optimally doped sample $Ba_{0.674}K_{0.326}Fe_2As_2$ exhibits a softening on cooling towards $T_c \approx 37\,\mathrm{K}$, followed by a clear hardening on further cooling below the transition temperature [see Fig. 4.34(c)]. The phonon linewidth increases on cooling towards T_c

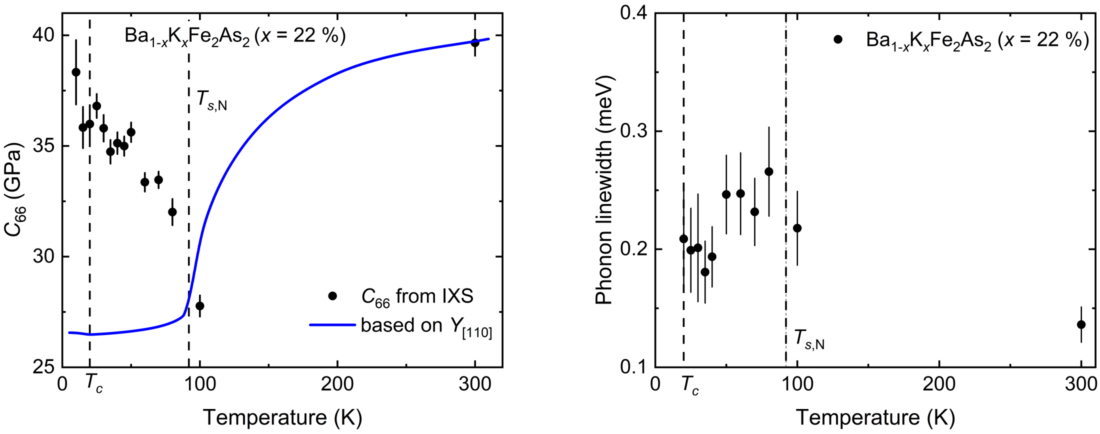

(a) C_{66} (b) Phonon linewidth

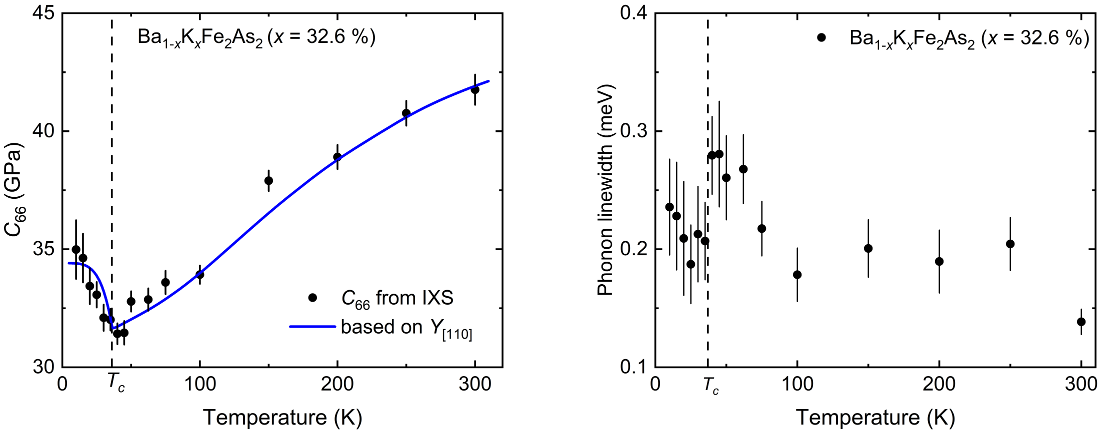

(c) C_{66} (d) Phonon linewidth

Figure 4.34: (a) C_{66} data of $Ba_{0.78}K_{0.22}Fe_2As_2$ as a function of the sample temperature at $\mathbf{Q} = (4,\ 0.075,\ 0)$. A softening on cooling towards $T \approx 100\,\mathrm{K}$ can be observed, followed by a nearly as strong hardening on further cooling. The blue line is based on Young's modulus measurements of Böhmer *et al.* [99]. (b) The phonon linewidth increases on cooling towards $T_{s,\mathrm{N}}$ and goes down after a small plateau on further cooling. (c) C_{66} data of $Ba_{0.674}K_{0.326}Fe_2As_2$ as a function of the sample temperature at $\mathbf{Q} = (4,\ 0.075,\ 0)$. A softening on cooling towards $T_c \approx 37\,\mathrm{K}$ can be observed, followed by a slight hardening on further cooling below the transition temperature. The blue line is based on Young's modulus measurements of Böhmer *et al.* [99]. Their results have been scaled to fit the observed maximum softening of 22 %. The reported softening was 20 %. (d) The phonon linewidth increases on cooling towards T_c and decreases down after on further cooling with its maximum at the superconducting transition temperature.

and decreases on further cooling with its maximum at the superconducting transition temperature [Fig. 4.34(d)].

4.4 Discussion and outlook

4.4.1 Optimally cobalt doped $\mathbf{Ba(Fe_{0.94}Co_{0.06})_2As_2}$

As already shown in Chapter 4.2 [92] there have been numerous studies on phonon effects in undoped iron-based systems [97]. However, they mostly focused on the phonon dispersion and the structural phase transitions. It was reported that non-magnetic DFT calculations do not predict the experimental results very well. The results agreed better with the magnetic calculations than with zero Fe momentum calculations [124]. The splitting of phonon peaks that was expected due to the twinning in the orthorhombic crystal lattice hosting magnetic order could initially not be observed. Murai *et al.* [125] could experimentally find the splitting predicted by magnetic DFT calculations using high-resolution inelastic x-ray scattering in $SrFe_2As_2$, a compound very similar to $BaFe_2As_2$. The effect was smaller than expected, which explains why it was not found earlier by Reznik *et al.* [124].

The superconducting pairing mechanism in the iron-based superconductors still remains elusive [82]. After an ongoing discussion it is widely believed that magnetic fluctuations are essential in mediating superconductivity and not as in conventional superconductors the electron-phonon coupling. Calculations with DFT [126] assume that in the cuprates and the pnictides the electron-phonon coupling is too weak to explain such high superconducting transition temperatures. However, it was experimentally shown that DFT [127] significantly underestimates the electron-phonon coupling in the cuprates [128, 129, 130]. While electron-phonon coupling might not be able to explain the high T_c's in the cuprates, phonon softening and damping effects can be very well observed and are another indicator of the strong competition between different degrees of freedom in these materials.

Based on this assumption Lamago *et al.* [131] searched for T_c-induced effects in $Ba(Fe_{1-x}Co_x)_2As_2$ (x = 0.06, 0.10). Since electron-phonon coupling effects have an effect on the phonon lifetime they also affect the phonon linewidth. In particular, phonons with an energy smaller than the superconducting gap 2Δ are not able to excite electrons in the superconducting phase and, hence, lose all damping which they might have shown in the normal state. Therefore, the study focused on phonon energies comparable to the superconducting gap (8.9 meV for the optimally doped sample and 6.8 meV for the overdoped sample). They did not see an effect due to superconductivity in the phonon energy nor the linewidth.

Our experiments on 1T showed that the previous study was performed in the wrong energy range. The INS measurements carried out at much smaller energies clearly showed superconductivity-induced energy shift of the phonons. A clear softening on cooling below T_c was observed. Furthermore the results suggested changes in the phonon linewidth associated with the superconducting phase. It has to be stated that those INS measurements are quite challenging in terms of momentum and energy resolution.

The measurements in $Ba(Fe_{0.94}Co_{0.06})_2As_2$ on the triple axes spin echo spectrometer TRISP (see Chapter 4.3.3) should validate the assumptions on the phonon lifetime. The analysis of the linewidth data showed that a pronounced phonon broadening occurs on cooling towards T_c. On further cooling below T_c a clear sharpening was observed. This is the first time that a change in the phonon lifetime and therefore a damping was experimentally observed in pnictides.

Studies on phonon effects in iron-based superconductors are scarce. However, the effects of phonon damping have been examined in detail in conventional superconductors, here related to electron-phonon coupling. Due to the excellent data in those systems our INS results will be compared to the widely studied elemental superconductor niobium. Figure 4.35 shows the phonon energy and phonon linewidth of Nb measured by Shapiro *et al.* [132]. The phonon energy shows a strong softening on cooling from room temperature towards the superconducting transition temperature. On further cooling below T_c an abrupt softening can be observed. The phonon linewidth drops significantly (towards zero) on cooling to below T_c. Here the phonons only interact with quasiparticles that are thermally excited above the superconducting gap of 2Δ. In the superconducting phase the phonons do not have enough energy to break up the Cooper pairs. Hence, the phonon lifetime is enhanced and the phonon linewidth decreases. Both a softening and a narrowing below T_c were also observed in our INS measurements at 1T (see Fig. 4.14) and NRSE measurements at TRISP (see Fig. 4.20). The temperature dependence of the phonon energy and the linewidth in $Ba(Fe_{0.94}Co_{0.06})_2As_2$ and Nb look very similar. This could lead to the assumption that electron-phonon coupling might play a larger role in iron-based superconductors than previously assumed. Especially the effects of the phonon lifetime with the smallest value at T_c might be a hint that the phonons are coupled to electrons at the Fermi surface which play also an important role for nematic fluctuations. Apparently, the phonon renormalization at T_c is not only restricted in energy but also in momentum space as explained in detail by the model dispersion equation (Eq. 4.6 on page 97). Theoreticians are working on a model for the dynamic coupling to solve the detailed coupling mechanism between lattice and electronic/magnetic degrees of freedom. With such a theory it might be possible to also determine the lifetime of the nematic fluctuations if they are coupling to the phonons.

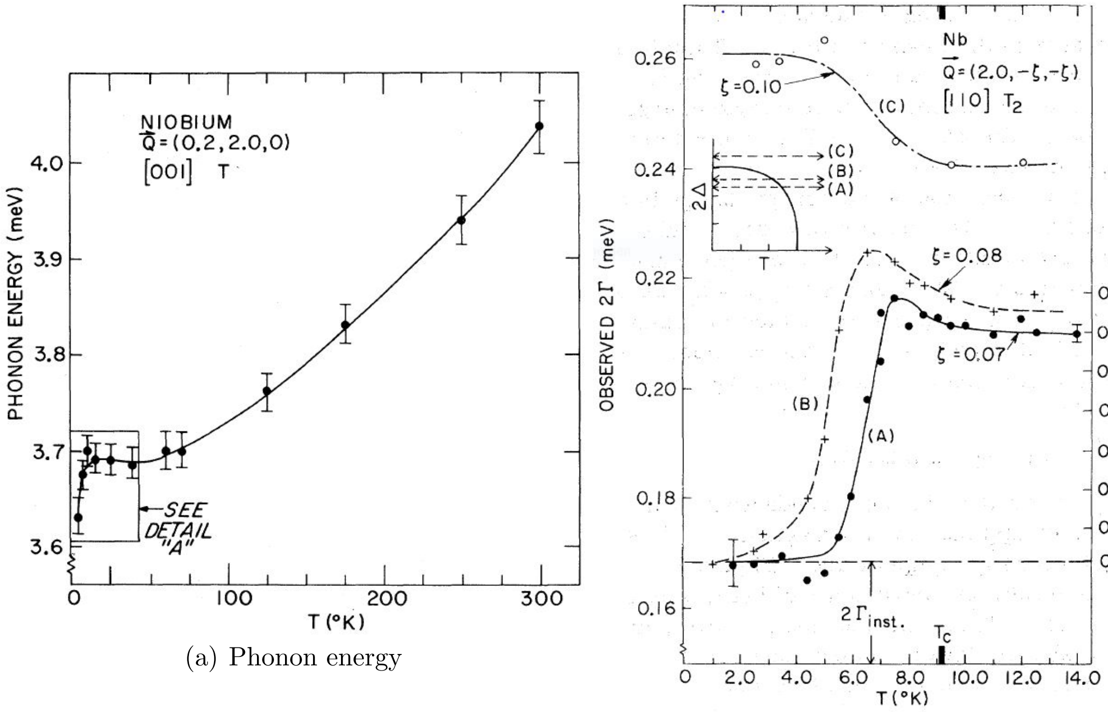

(a) Phonon energy

(b) Phonon linewidth

Figure 4.35: (a) Temperature dependence of a phonon in Nb showing the anomalous softening for $T_c < T < 300\,\mathrm{K}$ and an additional softening for $T < T_c$. (b) Temperature dependence of the linewidth of several phonons in Nb for low temperatures around T_c. [132]

In the framework of this thesis we showed that inelastic neutron scattering is suitable for investigating nematic fluctuations even without the need of external stress or strain in twinned samples which has been a problem in three-point bending and ultrasound measurements. Another major difference is that INS measurements take place at finite $\mathbf{q}$ whereas the other methods measure at $\mathbf{q} = 0$. Our experiments at $\mathbf{q} \neq 0$ gave us the opportunity to measure for the first time the correlation length of the nematic fluctuations ξ.

Wang *et al.* [133] showed that another experimental method can be used to study nematicity. Using neutron diffraction and neutron Larmor diffraction (on TRISP) they measured the temperature dependence of the orthorhombic distortion δ and the distribution of the interplanar atomic spacings $\Delta d/d$ in superconducting NaFe$_{1-x}$Ni$_x$As. They were measuring a Bragg peak in the longitudinal direction that is splitting into four different Bragg peaks on the tetragonal to orthorhombic phase transition [see Fig. 4.28(a)]. Upon the structural phase transition it is possible to resolve two different in-plane d-spacings, corresponding to different lattice parameters. Differently if the

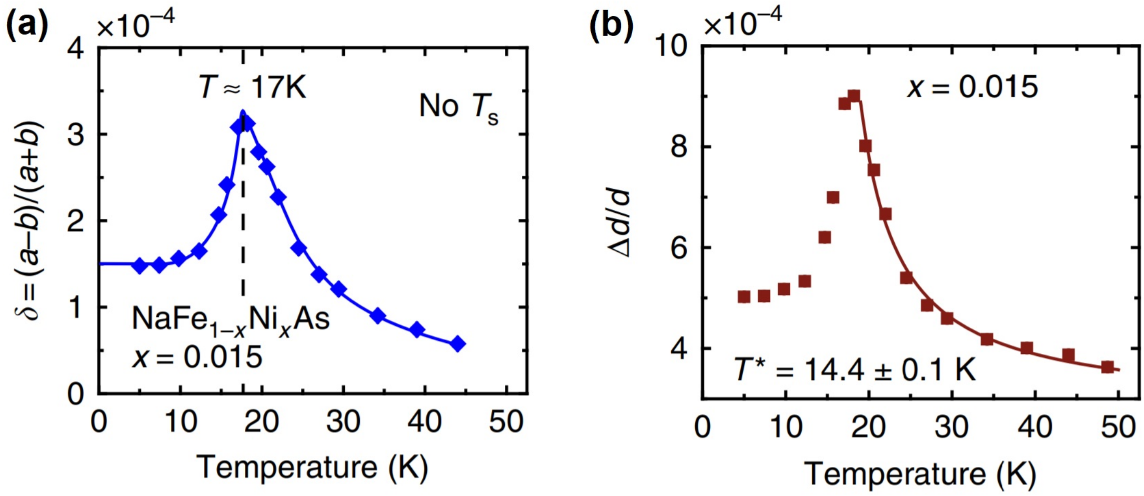

Figure 4.36: (a) Larmor diffraction study of the temperature dependence of the orthorhombic distortion δ for $\mathrm{NaFe_{0.985}Ni_{0.015}As}$. The solid line is a guide to the eye. δ is obtained by assuming that it is 0 at $T = 50\,\mathrm{K}$. (b) Temperature dependence of $\Delta d/d$ and Curie-Weiss fit to the data for $\mathrm{NaFe_{0.985}Ni_{0.015}As}$. [133]

sample only shows local orthorhombic distortions, i.e. in optimally doped samples, the Bragg peak is not completely splitting, only broadening. Then also a broadening of the d-spacing distribution can be observed while the average structure is still tetragonal. The study found local orthorhombic distortions that exist well above the structural transition from tetragonal to orthorhombic in underdoped samples and even in overdoped samples that exhibit neither magnetic nor structural phase transitions (Fig. 4.36). These local orthorhombic fluctuations can be described by Curie-Weiss fits [Fig. 4.36(b)] and are suppressed below the superconducting transition temperature. Therefore Wang *et al.* suggest that they result from the large nematic susceptibility near optimal superconductivity. These results for $\Delta d/d$ show a similar temperature dependence than the mosaicity measured in $\mathrm{Ba(Fe_{0.94}Co_{0.06})_2As_2}$ in the framework of our phonon lifetime study on TRISP. Obviously both quantities describe effects of the same structural distortion. The main difference is that the mosaicity is probing the transverse direction of the Bragg peak splitting (or broadening) and the d-spacing the longitudinal direction. The direction are corresponding to a splitting into three (mosaicity) or four different peaks ($\Delta d/d$) in Figure 4.28. The intensity of the Bragg peak that is probed by the mosaicity, e.g. (2 0 0), also shows a similar temperature dependence as the mosaicity and the distribution of the interplanar atomic spacings. The intensity of the Bragg peak increases for a higher mosaicity of the sample due to vanishing extinction in imperfect crystals [134]. This effect is well known and is used for monochromators where the mosaicity is enhanced on purpose to get stronger scattering intensities. The measurement of the intensity of the Bragg peak can be done with both neutrons and x-rays, even on a x-ray lab source and is a lot more straight forward than measurements of the mosaicity or $\Delta d/d$.

Figure 4.37 shows the comparison of the mosaicity from TRISP (red dots), Young's modulus $Y_{[110]}$ (black line) by Böhmer *et al.* [99], Bragg peak intensities from INS on 1T (blue triangles) in $Ba(Fe_{0.94}Co_{0.06})_2As_2$ and the distribution of the interplanar atomic spacings $\Delta d/d$ (green squares) for $NaFe_{0.985}Ni_{0.015}As$ by Wang *et al.* [133] (inset of Fig. 4.37). The shape of all curves is very similar even though they were measured with completely different techniques on different samples even in different systems. The figure also shows that the relation between the mosaicity and the Bragg intensities is not linear. However, the accordance of the data is quite remarkable and strongly supports the idea of using simple diffraction measurements to probe nematicity.

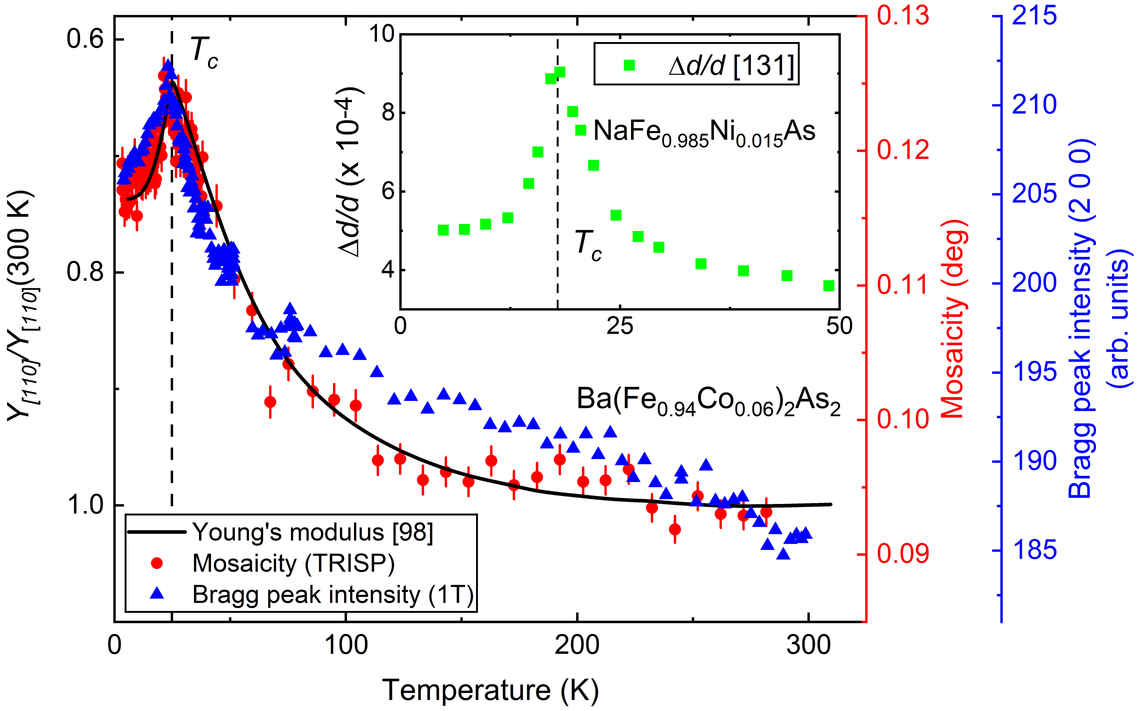

Figure 4.37: Comparison of different techniques to examine nematicity. The mosaicity from TRISP (red dots), Young's modulus $Y_{[110]}$ (black line) by Böhmer *et al.* [99] and Bragg peak intensities from INS on 1T (blue triangles) in Ba(Fe$_{0.94}$Co$_{0.06}$)$_2$As$_2$ are in really good agreement to each other. The inset shows the distribution of the interplanar atomic spacings $\Delta d/d$ (green squares) for NaFe$_{0.985}$Ni$_{0.015}$As by Wang *et al.* [133] which also has a very similar behavior.

4.4.2 Hole-doped samples

Besides the optimally cobalt doped samples first measurements on hole-doped samples were performed in this thesis. $\mathrm{Sr}_{1-x}\mathrm{Na}_x\mathrm{Fe}_2\mathrm{AS}_2$ ($x = 0.33$), $\mathrm{Ba}_{1-x}\mathrm{Na}_x\mathrm{Fe}_2\mathrm{As}_2$ ($x = 0.265$ and $x = 0.4$) and $\mathrm{Ba}_{1-x}\mathrm{K}_x\mathrm{Fe}_2\mathrm{As}_2$ ($x = 0.22$ and $x = 0.32.6$) samples have been investigated with inelastic x-ray scattering. The temperature dependence of the phonon energy was measured at one single wave vector $\mathbf{Q} = (4, 0.075, 0)$. Together with $\mathbf{q} = 0$ we have two points of the phonon dispersion and therefore only a linear fit represents a valid analysis and yields C_{66} related to the slope of the approximated linear dispersion. This is in contrast to the results from INS and IXS dispersion measurements in optimally doped Co-Ba122 and the theoretical model which propose a non-linear dispersion for $\mathbf{q} \neq 0$. However, the data can be used as an upper limit for the discussion of the nematic correlation length in hole-doped samples. They were compared to Young's modulus measurements by the Meingast group [99, 123] as it was done before for $Ba(Fe_{0.94}Co_{0.06})_2As_2$. The data were scaled to two values of the INS data, the high temperature value and the data point with the lowest phonon energy (C_{66}). Unfortunately for $Sr_{0.67}Na_{0.33}Fe_2AS_2$ there is no comparable data available, yet.

The underdoped $Ba_{0.735}Na_{0.265}Fe_2As_2$ and $Ba_{0.78}K_{0.22}Fe_2As_2$ samples both exhibit a structural phase transition. As already mentioned the previous ultrasound and three-point bending data are not reliable in the orthorhombic phase and cannot be compared to the data derived from inelastic x-ray scattering. However, both sample (and also the underdoped $Sr_{0.67}Na_{0.33}Fe_2AS_2$ sample) show a hardening in the orthorhombic phase.

The optimally doped $Ba_{0.6}Na_{0.4}Fe_2As_2$ and $Ba_{0.674}K_{0.326}Fe_2As_2$ samples exhibit only superconducting phase transitions and the results are in good agreement to the blue lines based on $Y_{[110]}$ on cooling towards T_c, showing a strong decrease of C_{66}. For the optimally K-doped sample both measurements fit also very well for the increasing C_{66} below T_c. In the optimally Na-doped sample further cooling below T_c, C_{66} seems to increase stronger in the IXS measurements than in the $Y_{[110]}$ measurements. The good agreement of our IXS derived results with those from three-point bending experiments indicate that in this/these sample/samples the wave vector $\mathbf{q} = (0, 0.075, 0)$ still can be considered to be in the small $\mathbf{q} \to 0$ limit. This is in contrast to the situation in optimally doped Co-Ba122, where there is a clear discrepancy between the temperature dependence of $Y_{[110]}$ and the phonon softening at the same wave vector (see Fig. 4.11). Figure 4.38 illustrates that our measurements just give an upper limit for the correlation length ξ which is closely connected to the curvature of the dispersion. The wave vector on which our studies were carried out just is too small to be sensitive to the curvature of the non-linear dispersion. The curvature might appear for higher $\mathbf{Q}$ (e.g. smaller ξ) and the chosen wave vector happens to be on a almost linear part of the dispersion. In both the optimally K- and Na-doped samples we estimate that the upper limit for $\xi \leq 18\,\text{Å}$. For all ξ larger than this limit, the deviations of the IXS and three-point bending measurements would be larger than the error bars.

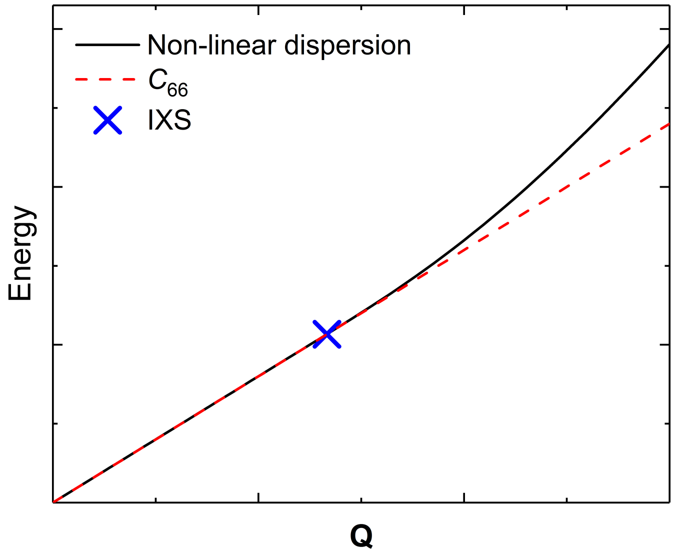

Figure 4.38: Inelastic x-ray measurements were carried out at one point of the phonon dispersion (indicated by the blue cross). The non-linear dispersion (black solid line) might exhibit a curvature at higher **Q**. Therefore it has the same value as C_{66} at the measured point.

However, this means that the results in these samples show that hole-doped samples exhibit a at least three times smaller correlation length than the electron-doped samples. This naturally gives rise to the question of what the difference between the hole- and electron-doped samples is. One major difference is that on hole doping the structural an magnetic phase transitions do not split. Whereas on electron doping the two transitions drift further apart on higher doping. Another difference is that the electron-doped samples seem to exhibit a nematic quantum critical point [96, 135]. In contrast hole-doped samples do not show hints for quantum criticality [99]. Moreover there might be a fundamental difference between the two different kinds of doping. In particular, it has been discussed controversially whether or not a substitution of Fe by Co does indeed lead to the widely assumed electron doping of $BaFe_2As_2$. There are studies that favor the picture of charge carriers arriving at the bands near E_F [136, 137] and others find arguments that assume a substitution and question the doping effect [138, 139]. Merz *et al.* [116] studied the spatial and electronic structure in various members of the iron-pnictide 122 family with x-ray diffraction and x-ray absorption. They tried to distinguish between charge-carrier doping effects and disorder effects. They reported that holes introduced by Ba/K substitution go only to Fe $3d$ states whereas carriers that are introduced by Fe substitution go exclusively to As $4s/4p$ states. Furthermore their data suggest that for Fe substitution, charge-carrier doping ('doping *per se*') is less important for the electronic and magnetic behavior in those compounds than the structural effects of substitution.

All of the aspects mentioned above might contribute to the different behavior of the two different kinds of doping, resulting in a shorter nematic correlation length ξ for the hole-doped systems compared to the electron-doped systems.

To get a better understanding of the differences between hole-doped and electron-doped systems and to further investigate the nematic correlation length ξ future systematic measurements are needed. Those should include studying ξ for a doping series and for different doping materials. It is instructive to do further measurements at SPring-8 since our results showed that it is most suitable for dispersion measurements.

Chapter 5

Summary

In the framework of this thesis inelastic neutron and x-ray scattering (INS and IXS, respectively) were used to study lattice dynamics in $LaCoO_3$ and various iron-pnictide superconductors of the AFe_2As_2 (A = Ba, Sr) family, with partial substitution of Fe by Co, or Ba and Sr by K and Na. Mainly inelastic scattering was used to study the phonon renormalization in those systems.

5.1 $LaCoO_3$

This thesis presented the first broad phonon study carried out on $LaCoO_3$. Furthermore it was the first experimental phonon investigation on this material that was strongly supported by detailed lattice dynamical calculations. We covered the temperature range from $2\,\mathrm{K} \leq T \leq 690\,\mathrm{K}$ and various wave vectors with our experimental work on the triple axis spectrometer 1T at the LLB. Those measurements were complemented by INS measurements of high energy phonons on PUMA and a study of atomic mean-square displacements (MSDs) with thermal neutron diffraction on HEiDi, both at MLZ.
The MSD and high energy phonon measurements suggest that the effects of the insulator-metal crossover which is typically seen at $T_{\mathrm{MI}} \approx 500\,\mathrm{K}$, e.g., in the magnetic susceptibility, influence the lattice dynamics at even lower temperatures, e.g. $T \approx 360 - 400\,\mathrm{K}$. This is in agreement with the onset of anomalous behavior in the lattice expansion. The MSDs of all three types of atoms shows an anomaly at $T \approx 360\,\mathrm{K}$. Since the anomaly was so far only observed for one temperature and was not reported in a similar study by Radaelli *et al.* [51] further measurements in this temperature range have to be done in the future. However, there are hints that the lattice is sensitive to the change of spin states in this temperature region. Not only have Señarís-Rodríguez *et al.* [72] identified $T \approx 350\,\mathrm{K}$ as an important temperature in the spin state evolution but also we have further evidence from phonon investigations at PUMA that the lattice

is affected by the insulator-metal crossover far below T_{MI}. The observed high energy phonon with a displacement pattern which strongly suggests to be associated with the breathing distortion seems to be sensitive to both crossovers. A softening on heating to above the spin-state crossover T_{SS} and a strong and abrupt hardening on further heating above $T \approx 360 - 400\,\mathrm{K}$ can be observed. On further heating the phonon energy stays constant above T_{MI} which suggests that the influence of the second crossover to the crystal lattice is the strongest way below the actual crossover.

The study of the acoustic phonons at 1T underlined the quality of the lattice dynamical calculations by Dr. K.P. Bohnen (KIT) that were used in this thesis to analyze the experimental data. The experimental energy scans could be easily compared to the calculated phonon intensities since the number of phonons and their energies in each scan were predicted really well. Furthermore the temperature dependence of the phonon energy was calculated accurately by the quasi-harmonic approximation for the normal phonon behavior. The phonons $\mathbf{Q} = (1.5, 1.5, 1.5)$ and $\mathbf{Q} = (1.5, 1.5, 2.5)$, both associated with the proposed ordering vector $\mathbf{q} = (0.5, 0.5, 0.5)$, exhibited an anomalous softening and broadening especially on heating to above the first crossover $T \approx 100\,\mathrm{K}$. The anomalous softening was extracted quantitatively by the subtraction of the the normal behavior calculated within the quasi-harmonic approximation. The result strongly suggested that the anomalous behavior arises from the population of HS states with increasing temperature and the associated magnetism. On heating towards the second crossover the phonon energy fits again to the calculated energies. Together with the absence of magnetism reported in previous studies this could be a hint to the melting of the HS/LS short-range dynamic order. To sum up our results we found a signature of the dynamic short-range order with a specific ordering vector (‘checkerboard’ structure).

For more information on the **q**-dependence of the HS/LS short-range dynamic order further measurements are needed. Especially for the high-energy mode dispersion measurements would be instructive. For an enhanced resolution of the **q**-dependence of the low energy phonons inelastic x-ray measurements seem to be most suitable.

5.2 Iron-based superconductors

Most of the INS work on iron-based superconductors was carried out on optimally cobalt doped $\mathrm{Ba(Fe_{0.94}Co_{0.06})_2As_2}$ samples. Furthermore first IXS measurements on hole-doped systems were done.

One of the major subjects is the relation between lattice dynamics, e.g. the soft phonon mode, nematicity and the magnetic/electronic degrees of freedom driving the nematic behavior. The results from the INS and IXS experiments in $\mathrm{Ba(Fe_{0.94}Co_{0.06})_2As_2}$ in the framework of this thesis served as the starting point for a theoretical model. The model was developed with R. Fernandes (University of Minnesota) and J. Schmalian (Karlsruhe Institute of Technology) describing the anomalous behavior of the phonon dispersion by introducing the nematic correlation length ξ. The observed sharp maximum of the nematic correlation length ξ and the strongest curvature of the experimental dispersion at T_c could both be explained due to the competition between nematic/magnetic fluctuations and superconductivity. Furthermore the concept of a nematic correlation length helped to resolve the apparent discrepancy between the phonon renormalization and the behavior of elastic constant $C_{66}(0)$ in the superconducting state.

Both the INS measurements at 1T and the phonon lifetime measurements at TRISP showed that a pronounced phonon broadening occurs on cooling towards T_c. On further cooling below T_c a clear sharpening was observed. This demonstrates that a change in the phonon lifetime and therefore a damping mechanism similar to conventional superconductors is experimentally observable in pnictides. The effects of the phonon lifetime with the smallest value at T_c might be a hint that the phonons are coupled to electrons at the Fermi surface which play also an important role for nematic fluctuations. Our analysis shows that not only the phonon energy is of importance but also its momentum $\mathbf{q}$. If and how the phonons couple to the ubiquitous nematic fluctuations in this important material class remains a task for the future.

There are several methods to investigate nematic fluctuations, i.e. three-point bending and ultrasound measurements. In the framework of this thesis we showed that INS is also suitable of measuring nematic fluctuations even without the need of external stress or strain in twinned samples. Moreover we proposed based on the comparison of different experimental results that simpler methods can also be used to probe nematicity. The mosaicity and even the Bragg peak intensity can be used for such investigations.

The temperature dependence of the phonon energies of hole-doped samples determined with IXS measurements showed good agreement with that of the shear modulus. This is in clear contrast to the observation for electron-doped $Ba(Fe_{0.94}Co_{0.06})_2As_2$. With this result we were able to determine an upper limit for the correlation length in hole-doped systems. We also found that ξ is significantly smaller in the hole-doped samples than it is in $Ba(Fe_{0.94}Co_{0.06})_2As_2$. Various differences between the two types of samples were identified as potential explanations for the different behavior regarding ξ.

For a better understanding of the differences between hole-doped and electron-doped Fe-based pnictide superconductors further systematic investigations of the nematic correlation length ξ are needed. They should include studying ξ for a doping series and for different doping materials. It would be instructive to do further measurements at SPring-8 since our results showed that this instrument is highly suitable for dispersion measurements whose importance for the nematic correlation length was underlined within this thesis.

List of Abbreviations

APS	Advanced Photon Source
CMR	colossal magnetoresistance
DFT	density functional theory
HERIX	high energy resolution inelastic x-ray
HS	high spin
INS	inelastic neutron scattering
IS	intermediate spin
IXS	inelastic x-ray scattering
KIT	Karlsruhe Institute of Technology
LDA	local density approximation
LLB	Laboratoire Léon Brillouin
LS	low spin
MLZ	Heinz Maier-Leibnitz Zentrum
MSD	mean square displacement
NRSE	neutron resonance spin echo
TAS	triple axes spectrometer
TRISP	three axes spin echo spectrometer

List of Figures

List of Tables

Bibliography

[1] *Nobel lectures : Physics ; 1991/95*, Hrsg.: Gosta [Hrsg.] Ekspong (World Scientific Publishing Co., Singapore, 1997).

[2] George E. Bacon, *Fifty years of neutron diffraction : the advent of neutron scattering* (Hilger, Bristol, 1986).

[3] G. L. Squires, *Introduction to the Theory of Thermal Neutron Scattering*, 3 ed. (Cambridge University Press, Cambridge, 2012).

[4] Bruno Dorner, *Coherent inelastic neutron scattering in lattice dynamics*, *Springer tracts in modern physics ; 93* (Springer, Berlin, 1982).

[5] Gen Shirane, Stephen M. Shapiro, John M. Tranquada, *Neutron scattering with a triple-axis spectrometer : basic techniques*, 1. publ. ed. (Cambridge University Press, Cambridge [u.a.], 2002).

[6] B. N. Brockhouse, *Inelastic Scattering Of Neutrons in Solids and Liquids*, International Atomic Energy Agency 113 (1961).

[7] C. Giacovazzo, *Fundamentals of Crystallography*, 2nd edn ed. (Oxford University Press, Oxford, 2002).

[8] *Modern diffraction methods*, Hrsg.: Eric J. [Hrsg.] Mittemeijer, Udo Siegfried [Hrsg.] Welzel (Wiley-VCH, Weinheim, 2013).

[9] M. Meven, V. Hutanu, G. Heger, *Scientific Review: HEiDi: Single Crystal Diffractometer at the Hot Source of the FRM II*, Neutron News **18**, 19 (2007).

[10] Heinz Maier-Leibnitz Zentrum et al., *HEiDi: Single crystal diffractometer at hot source*, Journal of large-scale research facilities **1**, (2015).

[11] Ayman H. Said, Harald Sinn, Ralu Divan, *New developments in fabrication of high-energy-resolution analyzers for inelastic X-ray spectroscopy*, Journal of Synchrotron Radiation **18**, 492 (2011).

[12] E. Burkel, J. Peisl, B. Dorner, *Observation of Inelastic X-Ray Scattering from Phonons*, EPL (Europhysics Letters) **3**, 957 (1987).

[13] B. Dorner, E. Burkel, J. Peisl, *An X-ray backscattering instrument with very high energy resolution*, Nuclear Instruments and Methods in Physics Research Section A: Accelerators, Spectrometers, Detectors and Associated Equipment **246**, 450 (1986).

[14] B. Dorner, E. Burkel, Th Illini, J. Peisl, *First measurement of a phonon dispersion curve by inelastic X-ray scattering*, Zeitschrift für Physik B Condensed Matter **69**, 179 (1987).

[15] Alfred Q.R. Baron, *Introduction to High-Resolution Inelastic X-Ray Scattering*, arXiv 1504.01098 (2015).

[16] Michael Krisch, Francesco Sette, in *Light Scattering in Solid IX*, Hrsg.: Manuel Cardona, Roberto Merlin (Springer Berlin Heidelberg, Berlin, Heidelberg, 2007), 317–370.

[17] Burkel Eberhard, *Phonon spectroscopy by inelastic x-ray scattering*, Reports on Progress in Physics **63**, 171 (2000).

[18] T. Keller, K. Habicht, H. Klann, M. Ohl, H. Schneider, B. Keimer, *The NRSE-TAS spectrometer at the FRM-2*, Applied Physics A **74**, s332 (2002).

[19] T. Keller, P. Aynajian, S. Bayrakci, K. Buchner, K. Habicht, H. Klann, M. Ohl, B. Keimer, *Scientific Review: The Triple Axis Spin-Echo Spectrometer TRISP at the FRM II*, Neutron News **18**, 16 (2007).

[20] Max-Planck-Institut für Festkörperforschung et al., *TRISP: Three axes spin echo spectrometer*, Journal of large-scale research facilities **1**, (2015).

[21] Ferenc Mezei, Catherine Pappas, Thomas Gutberlet, *Neutron spin echo spectroscopy : basics, trends and applications*, *Lecture notes in physics ; 601* (Springer, Berlin, 2003).

[22] T. Keller, R. Golub, R. Gähler, in *Scattering : scattering and inverse scattering in pure and applied science*, Hrsg.: Roy Pike (Academic Pr., San Diego, 2002), 1264–1286.

[23] R. Golub, R. Gähler, *A neutron resonance spin echo spectrometer for quasi-elastic and inelastic scattering*, Physics Letters A **123**, 43 (1987).

[24] F. Mezei, *Neutron inelastic scattering* (International Atomic Energy Agency (IAEA), Vienna, 1978), 125–134.

[25] K. Habicht, R. Golub, F. Mezei, B. Keimer, T. Keller, *Temperature-dependent phonon lifetimes in lead investigated with neutron-resonance spin-echo spectroscopy*, Physical Review B **69**, 104301 (2004).

[26] Klaus Habicht, Thomas Keller, Robert Golub, *The resolution function in neutron spin-echo spectroscopy with three-axis spectrometers*, Journal of Applied Crystallography **36**, 1307 (2003).

[27] P. Aynajian, T. Keller, L. Boeri, S. M. Shapiro, K. Habicht, B. Keimer, *Energy gaps and Kohn anomalies in elemental superconductors*, Science **319**, 1509 (2008).

[28] R. Heid, K. P. Bohnen, *Linear response in a density-functional mixed-basis approach*, Physical Review B **60**, R3709 (1999).

[29] Stefano Baroni, Stefano de Gironcoli, Andrea Dal Corso, Paolo Giannozzi, *Phonons and related crystal properties from density-functional perturbation theory*, Reviews of Modern Physics **73**, 515 (2001).

[30] J. P. Perdew, S. Kurth, in *A Primer in Density Functional Theory*, Hrsg.: C. Fiolhais, F. Nogueira, M. A. L. Marques (Springer, Berlin, Heidelberg, 2003), 1–55.

[31] P. Hohenberg, W. Kohn, *Inhomogeneous Electron Gas*, Physical Review **136**, B864 (1964).

[32] W. Kohn, L. J. Sham, *Self-Consistent Equations Including Exchange and Correlation Effects*, Physical Review **140**, A1133 (1965).

[33] A. D. Becke, *Density-functional exchange-energy approximation with correct asymptotic behavior*, Physical Review A **38**, 3098 (1988).

[34] John P. Perdew, Kieron Burke, Matthias Ernzerhof, *Generalized Gradient Approximation Made Simple*, Physical Review Letters **77**, 3865 (1996).

[35] Stefano Baroni, Paolo Giannozzi, Andrea Testa, *Elastic Constants of Crystals from Linear-Response Theory*, Physical Review Letters **59**, 2662 (1987).

[36] Stefano Baroni, Paolo Giannozzi, Andrea Testa, *Green's-function approach to linear response in solids*, Physical Review Letters **58**, 1861 (1987).

[37] G. H. Jonker, J. H. Van Santen, *Magnetic compounds wtth perovskite structure III. ferromagnetic compounds of cobalt*, Physica **19**, 120 (1953).

[38] M. W. Haverkort, Z. Hu, J. C. Cezar, T. Burnus, H. Hartmann, M. Reuther, C. Zobel, T. Lorenz, A. Tanaka, N. B. Brookes, H. H. Hsieh, H. J. Lin, C. T. Chen, L. H. Tjeng, *Spin State Transition in* $LaCoO_3$ *Studied Using Soft X-ray Absorption Spectroscopy and Magnetic Circular Dichroism*, Physical Review Letters **97**, 176405 (2006).

[39] Y. Tokura, Y. Okimoto, S. Yamaguchi, H. Taniguchi, T. Kimura, H. Takagi, *Thermally induced insulator-metal transition in* $LaCoO_3$*: A view based on the Mott transition*, Physical Review B **58**, R1699 (1998).

[40] J. G. Bednorz, K. A. Müller, *Possible highTc superconductivity in the Ba-La-Cu-O system*, Zeitschrift für Physik B Condensed Matter **64**, 189 (1986).

[41] B. Ivanova Natal'ya, G. Ovchinnikov Sergei, M. Korshunov Maksim, M. Eremin Il'ya, V. Kazak Natal'ya, *Specific features of spin, charge, and orbital ordering in cobaltites*, Physics-Uspekhi **52**, 789 (2009).

[42] J. M. Tranquada, B. J. Sternlieb, J. D. Axe, Y. Nakamura, S. Uchida, *Evidence for stripe correlations of spins and holes in copper oxide superconductors*, Nature **375**, 561 (1995).

[43] Y. Drees, D. Lamago, A. Piovano, A. C. Komarek, *Hour-glass magnetic spectrum in a stripeless insulating transition metal oxide*, Nature Communications **4**, 2449 (2013).

[44] Y. Drees, Z. W. Li, A. Ricci, M. Rotter, W. Schmidt, D. Lamago, O. Sobolev, U. Rütt, O. Gutowski, M. Sprung, A. Piovano, J. P. Castellan, A. C. Komarek, *Hour-glass magnetic excitations induced by nanoscopic phase separation in cobalt oxides*, Nature Communications **5**, 5731 (2014).

[45] V. Hinkov, P. Bourges, S. Pailhès, Y. Sidis, A. Ivanov, C. D. Frost, T. G. Perring, C. T. Lin, D. P. Chen, B. Keimer, *Spin dynamics in the pseudogap state of a high-temperature superconductor*, Nature Physics **3**, 780 (2007).

[46] M. Maschek, D. Lamago, J. P. Castellan, A. Bosak, D. Reznik, F. Weber, *Polaronic metal phases in* $La_{0.7}Sr_{0.3}MnO_3$ *uncovered by inelastic neutron and x-ray scattering*, Physical Review B **93**, 045112 (2016).

[47] M. Maschek, J.-P. Castellan, D. Lamago, D. Reznik, F. Weber, *Polaronic correlations and phonon renormalization in* $La_{0.7}Sr_{0.3}MnO_3$ *($x = 0.2, 0.3$)*, Phys. Rev. B **97**, 245139 (2018).

[48] N. Menyuk, K. Dwight, P. M. Raccah, *Low temperature crystallographic and magnetic study of* $LaCoO_3$, Journal of Physics and Chemistry of Solids **28**, 549 (1967).

[49] Gérard Demazeau, Michel Pouchard, Paul Hagenmuller, *Sur de nouveaux composés oxygénés du cobalt +III dérivés de la perovskite*, Journal of Solid State Chemistry **9**, 202 (1974).

[50] Hans-Rudolf Wenk, Andrej G. Bulach, *Minerals : their constitution and origin* (Cambridge Univ. Press, Cambridge [u.a.], 2004).

[51] P. G. Radaelli, S. W. Cheong, *Structural phenomena associated with the spin-state transition in* $\mathrm{LaCoO_3}$, Physical Review B **66**, 094408 (2002).

[52] K. Knížek, Z. Jirák, J. Hejtmánek, M. Veverka, M. Maryško, G. Maris, T. T. M. Palstra, *Structural anomalies associated with the electronic and spin transitions in* $LaCoO_3$, The European Physical Journal B - Condensed Matter and Complex Systems **47**, 213 (2005).

[53] K. Berggold, M. Kriener, P. Becker, M. Benomar, M. Reuther, C. Zobel, T. Lorenz, *Anomalous expansion and phonon damping due to the Co spin-state transition in* $RCoO_3$ *(R = La, Pr, Nd, and Eu)*, Physical Review B **78**, 134402 (2008).

[54] Kichizo Asai, Atsuro Yoneda, Osamu Yokokura, J. M. Tranquada, G. Shirane, Key Kohn, *Two Spin-State Transitions in* $LaCoO_3$, Journal of the Physical Society of Japan **67**, 290 (1998).

[55] C. Zobel, M. Kriener, D. Bruns, J. Baier, M. Grüninger, T. Lorenz, P. Reutler, A. Revcolevschi, *Evidence for a low-spin to intermediate-spin state transition in* $LaCoO_3$, Physical Review B **66**, 020402 (2002).

[56] Kichizo Asai, Osamu Yokokura, Nobuhiko Nishimori, Henry Chou, J. M. Tranquada, G. Shirane, Sadao Higuchi, Yuichiro Okajima, Kay Kohn, *Neutron-scattering study of the spin-state transition and magnetic correlations in* $La_{1-x}Sr_xCoO_3$ *(x =0 and 0.08)*, Physical Review B **50**, 3025 (1994).

[57] John B. Goodenough, *An interpretation of the magnetic properties of the perovskite-type mixed crystals* $La_{1-x}Sr_xCoO_{3-\lambda}$, Journal of Physics and Chemistry of Solids **6**, 287 (1958).

[58] M. A. Korotin, S. Yu Ezhov, I. V. Solovyev, V. I. Anisimov, D. I. Khomskii, G. A. Sawatzky, *Intermediate-spin state and properties of* $LaCoO_3$, Physical Review B **54**, 5309 (1996).

[59] A. Podlesnyak, S. Streule, J. Mesot, M. Medarde, E. Pomjakushina, K. Conder, A. Tanaka, M. W. Haverkort, D. I. Khomskii, *Spin-State Transition in* $LaCoO_3$*: Direct Neutron Spectroscopic Evidence of Excited Magnetic States*, Physical Review Letters **97**, 247208 (2006).

[60] S. Noguchi, S. Kawamata, K. Okuda, H. Nojiri, M. Motokawa, *Evidence for the excited triplet of* Co^{3+} *in* $LaCoO_3$, Physical Review B **66**, 094404 (2002).

[61] Z. Ropka, R. J. Radwanski, ^5D *term origin of the excited triplet in* $LaCoO_3$, Physical Review B **67**, 172401 (2003).

[62] R. Eder, *Spin-state transition in* $LaCoO_3$ *by variational cluster approximation*, Physical Review B **81**, 035101 (2010).

[63] Jan Kuneš, Vlastimil Křápek, *Disproportionation and Metallization at Low-Spin to High-Spin Transition in Multiorbital Mott Systems*, Physical Review Letters **106**, 256401 (2011).

[64] V. Křápek, P. Novák, J. Kuneš, D. Novoselov, Dm M. Korotin, V. I. Anisimov, *Spin state transition and covalent bonding in* $LaCoO_3$, Physical Review B **86**, 195104 (2012).

[65] Tôru Kyômen, Yoshinori Asaka, Mitsuru Itoh, *Negative cooperative effect on the spin-state excitation in* $\mathrm{LaCoO_3}$, Physical Review B **67**, 144424 (2003).

[66] Tôru Kyômen, Yoshinori Asaka, Mitsuru Itoh, *Thermodynamical analysis of spin-state transitions in* $LaCoO_3$*: Negative energy of mixing to assist thermal excitation to the high-spin excited state*, Physical Review B **71**, 024418 (2005).

[67] M. Karolak, M. Izquierdo, S. L Molodtsov, A. I. Lichtenstein, *Correlation-Driven Charge and Spin Fluctuations in* $LaCoO_3$, Physical Review Letters **115**, 046401 (2015).

[68] Jan Kuneš, Pavel Augustinský, *Excitonic instability at the spin-state transition in the two-band Hubbard model*, Physical Review B **89**, 115134 (2014).

[69] A. Doi, J. Fujioka, T. Fukuda, S. Tsutsui, D. Okuyama, Y. Taguchi, T. Arima, A. Q. R. Baron, Y. Tokura, *Multi-spin-state dynamics during insulator-metal crossover in* $LaCoO_3$, Physical Review B **90**, 081109 (2014).

[70] P. M. Raccah, J. B. Goodenough, *First-Order Localized-Electron Collective-Electron Transition in* $LaCoO_3$, Physical Review **155**, 932 (1967).

[71] Robert A. Bari, J. Sivardière, *Low-Spin-High-Spin Transitions in Transition-Metal-Ion Compounds*, Physical Review B **5**, 4466 (1972).

[72] M. A. Señarís-Rodríguez, J. B. Goodenough, $LaCoO_3$ *Revisited*, Journal of Solid State Chemistry **116**, 224 (1995).

[73] Thant Sin Naing, Toshiaki Kobayashi, Yoshihiko Kobayashi, Masaru Suzuki, Kichizo Asai, *Ultrasonic Measurement of $LaCoO_3$ –Evidence for the Orbital-Order Fluctuation–*, Journal of the Physical Society of Japan **75**, 084601 (2006).

[74] Y. Kobayashi, Thant Sin Naing, M. Suzuki, M. Akimitsu, K. Asai, K. Yamada, J. Akimitsu, P. Manuel, J. M. Tranquada, G. Shirane, *Inelastic neutron scattering study of phonons and magnetic excitations in $LaCoO_3$*, Physical Review B **72**, 174405 (2005).

[75] J. Q. Yan, J. S. Zhou, J. B. Goodenough, *Bond-length fluctuations and the spin-state transition in $LCoO_3$ (L = La, Pr, and Nd)*, Physical Review B **69**, 134409 (2004).

[76] D.A. Tennant, McMorrow D.F., Rescal for Matlab: a computational package for calculating neutron TAS resolution functions, 1995.

[77] Vaclav Petricek, Michal Dusek, Lukas Palatinus, JANA2006, 2001.

[78] A. Ishikawa, J. Nohara, S. Sugai, *Raman study of the orbital-phonon coupling in $LaCoO_3$*, Phys Rev Lett **93**, 136401 (2004).

[79] M. Merz, P. Nagel, C. Pinta, A. Samartsev, H. v. Löhneysen, M. Wissinger, S. Uebe, A. Assmann, D. Fuchs, S. Schuppler, *X-ray absorption and magnetic circular dichroism of $LaCoO_3$, $La_{0.7}Ce_{0.3}CoO_3$, and $La_{0.7}Sr_{0.3}CoO_3$ films: Evidence for cobalt-valence-dependent magnetism*, Phys. Rev. B **82**, 174416 (2010).

[80] D. Fuchs, C. Pinta, T. Schwarz, P. Schweiss, P. Nagel, S. Schuppler, R. Schneider, M. Merz, G. Roth, H. v. Löhneysen, *Ferromagnetic order in epitaxially strained $LaCoO_3$ thin films*, Phys. Rev. B **75**, 144402 (2007).

[81] A. Harada, T. Taniyama, Y. Takeuchi, T. Sato, T. Kyômen, M. Itoh, *Ferromagnetism at the surface of a $LaCoO_3$ single crystal observed using scanning SQUID microscopy*, Phys. Rev. B **75**, 184426 (2007).

[82] Yoichi Kamihara, Takumi Watanabe, Masahiro Hirano, Hideo Hosono, *Iron-Based Layered Superconductor $La[O_{1-x}F_x]FeAs$ $(x = 0.05-0.12)$ with $T_C = 26\,K$*, Journal of the American Chemical Society **130**, 3296 (2008).

[83] Zhi-An Ren, Wei Lu, Jie Yang, Wei Yi, Xiao-Li Shen, Cai Zheng, Guang-Can Che, Xiao-Li Dong, Li-Ling Sun, Fang Zhou, Zhong-Xian Zhao, *Superconductivity at 55 K in Iron-Based F-Doped Layered Quaternary Compound $Sm[O_{1-x}F_x]$ $FeAs$*, Chinese Physics Letters **25**, 2215 (2008).

[84] Pallecchi Ilaria, Eisterer Michael, Malagoli Andrea, Putti Marina, *Application potential of Fe-based superconductors*, Superconductor Science and Technology **28**, 114005 (2015).

[85] Tanabe Keiichi, Hosono Hideo, *Frontiers of Research on Iron-Based Superconductors toward Their Application*, Japanese Journal of Applied Physics **51**, 010005 (2012).

[86] Shimoyama Jun-ichi, *Potentials of iron-based superconductors for practical future materials*, Superconductor Science and Technology **27**, 044002 (2014).

[87] David C. Johnston, *The puzzle of high temperature superconductivity in layered iron pnictides and chalcogenides*, Advances in Physics **59**, 803 (2010).

[88] G. R. Stewart, *Superconductivity in iron compounds*, Reviews of Modern Physics **83**, 1589 (2011).

[89] R. M. Fernandes, A. V. Chubukov, J. Schmalian, *What drives nematic order in iron-based superconductors?*, Nature Physics **10**, 97 (2014).

[90] R. M. Fernandes, L. H. VanBebber, S. Bhattacharya, P. Chandra, V. Keppens, D. Mandrus, M. A. McGuire, B. C. Sales, A. S. Sefat, J. Schmalian, *Effects of Nematic Fluctuations on the Elastic Properties of Iron Arsenide Superconductors*, Physical Review Letters **105**, 157003 (2010).

[91] Eduardo Fradkin, Steven A. Kivelson, Michael J. Lawler, James P. Eisenstein, Andrew P. Mackenzie, *Nematic Fermi Fluids in Condensed Matter Physics*, Annual Review of Condensed Matter Physics **1**, 153 (2010).

[92] D. Parshall, L. Pintschovius, J. L. Niedziela, J. P. Castellan, D. Lamago, R. Mittal, Th Wolf, D. Reznik, *Close correlation between magnetic properties and the soft phonon mode of the structural transition in* $BaFe_2As_2$ *and* $SrFe_2As_2$, Physical Review B **91**, 134426 (2015).

[93] Marianne Rotter, Marcus Tegel, Dirk Johrendt, *Superconductivity at 38 K in the Iron Arsenide* $(Ba_{1-x}K_x)Fe_2As_2$, Physical Review Letters **101**, 107006 (2008).

[94] T. Yildirim, *Strong Coupling of the Fe-Spin State and the As-As Hybridization in Iron-Pnictide Superconductors from First-Principle Calculations*, Phys. Rev. Lett. **102**, 037003 (2009).

[95] K.W. Kim, A. Pashkin, H. Schäfer, M. Beyer, M. Porer, T. Wolf, C. Bernhard, J. Demsar, R. Huber, A. Leitenstorfer, *Ultrafast transient generation of spin-density-wave order in the normal state of* $BaFe_2As_2$ *driven by coherent lattice vibrations*, Nature Materials **11**, 497 (2012), 43.11.01; LK 01.

[96] Jiun-Haw Chu, Hsueh-Hui Kuo, James G. Analytis, Ian R. Fisher, *Divergent Nematic Susceptibility in an Iron Arsenide Superconductor*, Science **337**, 710 (2012).

[97] Ming Yi, Donghui Lu, Jiun-Haw Chu, James G. Analytis, Adam P. Sorini, Alexander F. Kemper, Brian Moritz, Sung-Kwan Mo, Rob G. Moore, Makoto Hashimoto, Wei-Sheng Lee, Zahid Hussain, Thomas P. Devereaux, Ian R. Fisher, Zhi-Xun Shen, *Symmetry-breaking orbital anisotropy observed for detwinned $Ba(Fe_{1-x}Co_x)_2As_2$ above the spin density wave transition*, Proceedings of the National Academy of Sciences **108**, 6878 (2011).

[98] Xingye Lu, J. T. Park, Rui Zhang, Huiqian Luo, Andriy H. Nevidomskyy, Qimiao Si, Pengcheng Dai, *Nematic spin correlations in the tetragonal state of uniaxial-strained $BaFe_{2-x}Ni_xAs_2$*, Science **345**, 657 (2014).

[99] A. E. Böhmer, P. Burger, F. Hardy, T. Wolf, P. Schweiss, R. Fromknecht, M. Reinecker, W. Schranz, C. Meingast, *Nematic Susceptibility of Hole-Doped and Electron-Doped $BaFe_2As_2$ Iron-Based Superconductors from Shear Modulus Measurements*, Physical Review Letters **112**, 047001 (2014).

[100] Y. Gallais, R. M. Fernandes, I. Paul, L. Chauvière, Y. X. Yang, M. A. Méasson, M. Cazayous, A. Sacuto, D. Colson, A. Forget, *Observation of Incipient Charge Nematicity in $Ba(Fe_{1-x}Co_x)_2As_2$*, Physical Review Letters **111**, 267001 (2013).

[101] Gianluca Giovannetti, Carmine Ortix, Martijn Marsman, Massimo Capone, Jeroen van den Brink, José Lorenzana, *Proximity of iron pnictide superconductors to a quantum tricritical point*, Nature Communications **2**, 398 (2011).

[102] Hiroshi Kontani, Tetsuro Saito, Seiichiro Onari, *Origin of orthorhombic transition, magnetic transition, and shear-modulus softening in iron pnictide superconductors: Analysis based on the orbital fluctuations theory*, Physical Review B **84**, 024528 (2011).

[103] Masahito Yoshizawa, Daichi Kimura, Taiji Chiba, Shalamujiang Simayi, Yoshiki Nakanishi, Kunihiro Kihou, Chul-Ho Lee, Akira Iyo, Hiroshi Eisaki, Masamichi Nakajima, Shin-ichi Uchida, *Structural Quantum Criticality and Superconductivity in Iron-Based Superconductor $Ba(Fe_{1-x}Co_x)_2As_2$*, Journal of the Physical Society of Japan **81**, 024604 (2012).

[104] Rafael M. Fernandes, Jörg Schmalian, *Manifestations of nematic degrees of freedom in the magnetic, elastic, and superconducting properties of the iron pnictides*, Superconductor Science and Technology **25**, 084005 (2012).

[105] Pengcheng Dai, Jiangping Hu, Elbio Dagotto, *Magnetism and its microscopic origin in iron-based high-temperature superconductors*, Nature Physics **8**, 709 (2012).

[106] C. de la Cruz, Q. Huang, J. W. Lynn, J. Li, 2nd Ratcliff, W., J. L. Zarestky, H. A. Mook, G. F. Chen, J. L. Luo, N. L. Wang, P. Dai, *Magnetic order close to superconductivity in the iron-based layered $LaO_{1-x}F_xFeAs$ systems*, Nature **453**, 899 (2008).

[107] Dirk Johrendt, *Structure-property relationships of iron arsenide superconductors*, Journal of Materials Chemistry **21**, 13726 (2011).

[108] Anna Elisabeth Böhmer, *Competing Phases in Iron-Based Superconductors Studied by High-Resolution Thermal-Expansion and Shear-Modulus Measurements*, Dissertation, 2014.

[109] S. Tonegawa, S. Kasahara, T. Fukuda, K. Sugimoto, N. Yasuda, Y. Tsuruhara, D. Watanabe, Y. Mizukami, Y. Haga, T. D. Matsuda, E. Yamamoto, Y. Onuki, H. Ikeda, Y. Matsuda, T. Shibauchi, *Direct observation of lattice symmetry breaking at the hidden-order transition in URu_2Si_2*, Nat Commun **5**, (2014).

[110] K. Grube, L. Pintschovius, F. Weber, J. P. Castellan, S. Zaum, S. Kuntz, P. Schweiss, O. Stockert, S. Bachus, Y. Shimura, V. Fritsch, H. v Löhneysen, *Magnetic and Structural Quantum Phase Transitions in* $\mathrm{CeCu}_{6-x}\mathrm{Au}_x$ *are Independent*, Physical Review Letters **121**, 087203 (2018).

[111] J. L. H. Lindenhovius, E. M. Hornsveld, A. den Ouden, W. A. J. Wessel, H. H. J. ten Kate, *Powder-in-tube (PIT) Nb_3Sn conductors for high-field magnets*, IEEE Transactions on Applied Superconductivity **10**, 975 (2000).

[112] L. R. Testardi, *Structural instability and superconductivity in A-15 compounds*, Reviews of Modern Physics **47**, 637 (1975).

[113] W. Rehwald, *Lattice softening and stiffening of single crystal niobium stannide at low temperatures*, Physics Letters A **27**, 287 (1968).

[114] A. E. Böhmer, F. Hardy, L. Wang, T. Wolf, P. Schweiss, C. Meingast, *Superconductivity-induced re-entrance of the orthorhombic distortion in $Ba_{1-x}K_xFe_2As_2$*, Nature Communications **6**, 7911 (2015).

[115] F. Weber, D. Parshall, L. Pintschovius, J. P. Castellan, M. Kauth, M. Merz, Th. Wolf, M. Schütt, J. Schmalian, R. M. Fernandes, D. Reznik, *Soft phonons reveal the nematic correlation length in* $\mathrm{Ba(Fe_{0.94}Co_{0.06})_2As_2}$, Physical Review B **98**, 014516 (2018).

[116] Michael Merz, Peter Schweiss, Peter Nagel, Meng-Jie Huang, Robert Eder, Thomas Wolf, Hilbert von Löhneysen, Stefan Schuppler, *Of Substitution and Doping: Spatial and Electronic Structure in Fe Pnictides*, Journal of the Physical Society of Japan **85**, 044707 (2016).

[117] U. Karahasanovic, J. Schmalian, *Elastic coupling and spin-driven nematicity in iron-based superconductors*, Physical Review B **93**, 064520 (2016).

[118] Rekveldt, M. T., Keller, T., Golub, R., *Larmor precession, a technique for high-sensitivity neutron diffraction*, Europhys. Lett. **54**, 342 (2001).

[119] Athena S. Sefat, Rongying Jin, Michael A. McGuire, Brian C. Sales, David J. Singh, David Mandrus, *Superconductivity at 22 K in Co-Doped* $BaFe_2As_2$ *Crystals*, Physical Review Letters **101**, 117004 (2008).

[120] K. M. Taddei, J. M. Allred, D. E. Bugaris, S. Lapidus, M. J. Krogstad, R. Stadel, H. Claus, D. Y. Chung, M. G. Kanatzidis, S. Rosenkranz, R. Osborn, O. Chmaissem, *Detailed magnetic and structural analysis mapping a robust magnetic* C_4 *dome in* $Sr_{1-x}Na_xFe_2As_2$, Phys. Rev. B **93**, 134510 (2016).

[121] J. M. Allred, K. M. Taddei, D. E. Bugaris, M. J. Krogstad, S. H. Lapidus, D. Y. Chung, H. Claus, M. G. Kanatzidis, D. E. Brown, J. Kang, R. M. Fernandes, I. Eremin, S. Rosenkranz, O. Chmaissem, R. Osborn, *Double-Q spin-density wave in iron arsenide superconductors*, Nature Physics **12**, (2016).

[122] L. Wang, F. Hardy, A. E. Böhmer, T. Wolf, P. Schweiss, C. Meingast, *Complex phase diagram of* $Ba_{1-x}Na_xFe_2As_2$*: A multitude of phases striving for the electronic entropy*, Physical Review B **93**, 014514 (2016).

[123] Liran Wang, Mingquan He, Frédéric Hardy, Peter Adelmann, Thomas Wolf, Michael Merz, Peter Schweiss, Christoph Meingast, *Large nematic susceptibility in the double-Q* C_4 *magnetic phase of* $Ba_{1-x}Na_xFe_2As_2$, Physical Review B **97**, 224518 (2018).

[124] D. Reznik, K. Lokshin, D. C. Mitchell, D. Parshall, W. Dmowski, D. Lamago, R. Heid, K.-P. Bohnen, A. S. Sefat, M. A. McGuire, B. C. Sales, D. G. Mandrus, A. Subedi, D. J. Singh, A. Alatas, M. H. Upton, A. H. Said, A. Cunsolo, Yu. Shvyd'ko, T. Egami, *Phonons in doped and undoped* $BaFe_2As_2$ *investigated by inelastic x-ray scattering*, Phys. Rev. B **80**, 214534 (2009).

[125] N. Murai, T. Fukuda, T. Kobayashi, M. Nakajima, H. Uchiyama, D. Ishikawa, S. Tsutsui, H. Nakamura, M. Machida, S. Miyasaka, S. Tajima, A. Q. R. Baron, *Effect of magnetism on lattice dynamics in* $SrFe_2As_2$ *using high-resolution inelastic x-ray scattering*, Phys. Rev. B **93**, 020301 (2016).

[126] L. Boeri, O. V. Dolgov, A. A. Golubov, *Is* $LaFeAsO_{1-x}F_x$ *an Electron-Phonon Superconductor?*, Phys. Rev. Lett. **101**, 026403 (2008).

[127] K.-P. Bohnen, R. Heid, M. Krauss, *Phonon dispersion and electron-phonon interaction for* $YBa_2Cu_3O_7$ *from first-principles calculations*, Europhys. Lett. **64**, 104 (2003).

[128] D. Reznik, B. Keimer, F. Dogan, I. A. Aksay, *q Dependence of Self-Energy Effects of the Plane Oxygen Vibration in* $YBa_2Cu_3O_7$, Phys. Rev. Lett. **75**, 2396 (1995).

[129] N. Pyka, W. Reichardt, L. Pintschovius, G. Engel, J. Rossat-Mignod, J. Y. Henry, *Superconductivity-induced phonon softening in* $YBa_2Cu_3O_7$ *observed by inelastic neutron scattering*, Phys. Rev. Lett. **70**, 1457 (1993).

[130] M. Krantz, H. J. Rosen, R. M. Macfarlane, V. Y. Lee, *Effect of oxygen stoichiometry on softening of Raman active lattice modes in* $YBa_2Cu_3O_x$, Phys. Rev. B **38**, 4992 (1988).

[131] D. Lamago, L. Pintschovius, D. Reznik, R. Heid, Th. Wolf, R. Mittal, S.L. Chaplot, *Search for an effect of superconductivity on the phonons in* $Ba(Fe_{1-x}Co_x)_2As_2$, Physica C: Superconductivity **471**, 1595 (2011).

[132] S. M. Shapiro, G. Shirane, J. D. Axe, *Measurements of the electron-phonon interaction in Nb by inelastic neutron scattering*, Phys. Rev. B **12**, 4899 (1975).

[133] Weiyi Wang, Yu Song, Chongde Cao, Kuo-Feng Tseng, Thomas Keller, Yu Li, Leland W. Harriger, Wei Tian, Songxue Chi, Ren-Feng Yu, Andriy H. Nevidomskyy, Pengcheng Dai, *Local orthorhombic lattice distortions in the paramagnetic tetragonal phase of superconducting* $NaFe_{1-x}Ni_xAs$, Nature Communications **9**, 3128 (2018).

[134] M. Schlenker, J.-P. Guigay, in *International Tables for Crystallography Volume B: Reciprocal space*, Hrsg.: U. Shmueli (Springer Netherlands, Dordrecht, 2001), 557–569.

[135] Christoph Meingast, Frédéric Hardy, Rolf Heid, Peter Adelmann, Anna Böhmer, Philipp Burger, Doris Ernst, Rainer Fromknecht, Peter Schweiss, Thomas Wolf, *Thermal Expansion and Grüneisen Parameters of* $Ba(Fe_{1-x}Co_x)_2As_2$*: A Thermodynamic Quest for Quantum Criticality*, Phys. Rev. Lett. **108**, 177004 (2012).

[136] Chang Liu, A. D. Palczewski, R. S. Dhaka, Takeshi Kondo, R. M. Fernandes, E. D. Mun, H. Hodovanets, A. N. Thaler, J. Schmalian, S. L. Bud'ko, P. C.

Canfield, A. Kaminski, *Importance of the Fermi-surface topology to the superconducting state of the electron-doped pnictide Ba(Fe$_{1-x}$Co$_x$)$_2$As$_2$*, Phys. Rev. B **84**, 020509 (2011).

[137] Walid Malaeb, Teppei Yoshida, Atsushi Fujimori, Masato Kubota, Kanta Ono, Kunihiro Kihou, Parasharam M. Shirage, Hijiri Kito, Akira Iyo, Hiroshi Eisaki, Yasuyuki Nakajima, Tsuyoshi Tamegai, Ryotaro Arita, *Three-Dimensional Electronic Structure of Superconducting Iron Pnictides Observed by Angle-Resolved Photoemission Spectroscopy*, Journal of the Physical Society of Japan **78**, 123706 (2009).

[138] M. Merz, F. Eilers, Th. Wolf, P. Nagel, H. v. Löhneysen, S. Schuppler, *Electronic structure of single-crystalline Sr(Fe$_{1-x}$Co$_x$)$_2$As$_2$ probed by x-ray absorption spectroscopy: Evidence for effectively isovalent substitution of Fe^{2+} by Co^{2+}*, Phys. Rev. B **86**, 104503 (2012).

[139] E. M. Bittar, C. Adriano, T. M. Garitezi, P. F. S. Rosa, L. Mendon ça Ferreira, F. Garcia, G. de M. Azevedo, P. G. Pagliuso, E. Granado, *Co-Substitution Effects on the Fe Valence in the* $\mathrm{BaFe_2As_2}$ *Superconducting Compound: A Study of Hard X-Ray Absorption Spectroscopy*, Phys. Rev. Lett. **107**, 267402 (2011).